PHARMACOKINETIC-PHARMACODYNAMIC MODEL ON A CHIP FOR TESTING TOXICITY OF CHEMOTHERAPEUTIC AGENTS

A Dissertation
Presented to the Faculty of the Graduate School
of Cornell University
in Partial Fulfillment of the Requirements for the Degree of
Doctor of Philosophy

by
Jong Hwan Sung
August 2009

PHARMACOKINETIC-PHARMACODYNAMIC MODEL ON A CHIP FOR TESTING TOXICITY OF CHEMOTHERAPEUTIC AGENTS

Jong Hwan Sung, Ph. D.

Cornell University 2009

Human response to drugs and environmental chemicals is often dramatically different from predictions made by conventional cell-based assays. Current in vitro methods for testing drug toxicity use a single cell type in a static culture environment, treated with a bolus dose. Such experiments do not capture the complex, dynamic response of the body to drug absorption, distribution, metabolism and excretion (ADME). Integrated pharmacokinetic-pharmacodynamic (PK-PD) models allow prediction of pharmacological outcome from a give dosage, but have limitations in building realistic models. A micro cell culture analog (μCCA) is a microfluidic device based on a physiologically-based pharmacokinetic (PBPK) model, with multiple chambers each representing an organ or tissue on a silicon chip, with these chambers connected to emulate the blood circulation.

This thesis work describes the combined approach of a PK-PD modeling and a μCCA platform, for testing the toxicity of chemotherapeutic agents. A PK-PD model was developed to predict tumor growth in a rat, treated with the chemotherapeutic agent, Tegafur. Various dosing scenarios and the effect of metabolizing enzyme levels were tested. As an experimental approach, the μCCA was improved in design, to accommodate 3-D hydrogel cell cultures and to enable a long-term operation. Using the μCCA, metabolism-dependent toxicity of Tegafur was observed. A PK-PD model for a μCCA was developed, and differential responses of three cell lines (representing the liver, tumor, and marrow) to the drugs in static and dynamic conditions were analyzed. A major challenge in developing microfluidic systems is prevention of

bubble formation. A microscale bubble trap was developed, and it was demonstrated that the presence of a bubble trap significantly alleviated the bubble interference. To address the issue of detection and analysis in a microfluidic device, an *in situ*, fluorescence optical detection system was developed and integrated with a μCCA, and a real-time detection of cell viability and metabolic activity was demonstrated.

This thesis work demonstrates the use of a microfluidic device, μCCA for a pharmacokinetic-based drug toxicity study and its combination with a mathematical modeling for a quantitative analysis of cell death kinetics. We envision that the combined approach will be useful in improving the productivity of drug development process by supplementing animal and human studies.

BIOGRAPHICAL SKETCH

Jong Hwan Sung was born in Seoul, Republic of Korea, in February 1978. He attended Seoul National University and graduated in 2000 with a Bachelor of Science in Chemical Engineering. After graduation, he went on to pursue a master's degree in the same university, under the guidance of Prof. Tai Hyun Park in Cell and Microbial Engineering Laboratory. There he worked on developing an 'artificial nose' system, by expressing a recombinant protein (odorant receptor originated from *C.elegans*) in *Escherichia coli* and measuring the binding of odorant molecules to the receptors. He graduated with a Master of Science in Chemical Engineering in August 2003. He came to United States in 2003, to begin his studies in the School of Chemical and Biomolecular Engineering at Cornell University. Currently he has accepted a post doctorial position in Prof. Dan Luo's lab in Biological and Environmental Engineernig at Cornell University.

ACKNOWLEDGEMENTS

The works described here were made possible by a number of people. First of all, I consider myself as a fortunate student, who was lucky enough to be mentored by Prof. Shuler, who gave me valuable lessons during the years. Before I joined his lab, at the faculty presentation session, he began his introduction by saying that he was looking for students to work *with* him, and not *for* him. Now I understand the meaning of his remark more clearly, as I believe I have grown to be a better person and a researcher through working with him, and not just for him. I also thank my minor committee members, Prof. Schwark and Prof. Putnam, for providing helpful and insightful discussion for completing this thesis. Paula Miller, our lab manager, and Glenn Swan at the machine shop, supported my work with their years of experience. Our group members, Kwanchanok Viravaidya, Dan Tatosian, and Grechen McAuliffe initially taught me about my CCA project, and Anjali Dhiman has been a wonderful mentor and co-worker. My other group members, Jordan Atlas, Tricia Echtenkamp, Rishard Chen, Iman Elgheriany, Hui Xu, Mandy Esch, and BJ made my years more pleasant. Finally, I thank my family, my parents and my sister, Ji Youn. Above all, my wife, Hwa Kyung, supported me through all of my times and made it possible.

This work was supported in part by Nanobiotechnology center (NBTC, project CM-2 (Nanotechnological Assessment of Drug Toxicity)), NSF (National Science Foundation), CNF (Cornell Nanoscale Science and Technology Facility), and also through a grant from Army Corp of Engineers (CERL) W9132T-07. J. JHS gratefully acknowledges support from Samsung Lee Kun Hee Scholarship Foundation.

TABLE OF CONTENTS

BIOGRAPHICAL SKETCH iii
ACKNOWLEDGEMENTS iv
TABLE OF CONTENTS v
LIST OF TABLES ix
LIST OF FIGURES x
LIST OF ABBREVIATIONS xii
1. INTRODUCTION 1
1.1 Motivation 1
1.2 Integrated Pharmacokinetic-Pharmacodynamic (PK-PD) Modeling 4
1.3 Previous Works in Micro Cell Culture Analog (μCCA) 6
1.4 Specific Goals and Outlines 9
2. COMBINED PHARMACOKINETIC-PHARMACODYNAMIC (PK-PD) MODEL FOR TUMOR GROWTH IN THE RAT AFTER UFT ADMINISTRATION 14
2.1 Introduction 14
2.2 Methods 15
2.2.1 Experimental Background for Model Development 15
2.2.2 Physiologically-based Pharmacokinetic (PBPK) Model Structure 17
2.2.3 PBPK Model Parameters 21
2.2.4 Curve Fitting Procedure 24
2.2.5 Pharmacodynamic (PD) Model 28
2.3 Results 33
2.3.1 Construction of PK-PD model 33
2.3.2 Optimization of Dosing Regimens 38
2.4 Discussion 47
2.4.1 The construction of PBPK model and PD model 47
2.5 Conclusion 53
3. SILICON MICRO CELL CULTURE ANALOG (μCCA) WITH 3-D HYDROGEL CULTURES FOR ASSESSING METABOLISM-DEPENDENT CYTOTOXICITY OF ANTI-CANCER DRGS 59
3.1 Introduction 59
3.2 Materials and Methods 61
3.2.1 Chemicals and Cell Line 61

3.2.2 Design and Fabrication of a μCCA 61
3.2.3 Incorporation of Hydrogel into a μCCA and Assembly of a μCCA Device64
3.2.4 Operation of a μCCA and Cell Viability Analysis 67
3.2.5 96-well Microtiter Plate Cytotoxicity Assay 67
3.2.6 Image Processing 68
3.2.8 Simulation of Transport inside a μCCA 68
3.3 Results 71
3.3.1 Verification of Design and Operation of a μCCA 71
3.3.2 Cell Culture in Hydrogel in a μCCA 71
3.3.3 Toxicity of Tegafur and 5-FU 74
3.3.4 Gradient Formation inside Alginate 80
3.4 Discussion 82
3.4.1 Long-term Operation of a μCCA 82
3.4.2 3-D Hydrogel Cell Culture in a μCCA 82
3.4.3 Toxicity of Chemotherapeutic Agents in a 96-well Plate and a μCCA 85
3.5 Conclusion 87
4. MICROSCALE BUBBLE TRAP 91
4.1 Introduction 91
4.2 Materials and Methods 94
4.2.1 Materials 94
4.2.2 Design of a Bubble Trap 95
4.2.3 Fabrication of a Bubble Trap 97
4.2.4 Bubble Trap Efficiency 98
4.2.5 Finite-Element Simulation of Flow 98
4.2.6 Cell Culture Test Using Micro Cell Culture Analog (μCCA) 99
4.3 Results and Discussion 99
4.3.1 Design and Fabrication of a Bubble Trap 99
4.3.2 Trapping and Removal of Bubbles 100
4.3.3 Microfluidic Cell Culture Test 103
4.4. Conclusion 109
5. *IN SITU* FLUORESCENCE OPTICAL DETECTION SYSTEM FOR INTEGRATION WITH μCCA FOR REAL-TIME ANALYSIS 112
5.1 Introduction 112
5.2 Materials and Methods 115

5.2.1 Cell Culture and Chemicals 115
5.2.2 ISFODS for Cell Viability Measurement 115
5.2.3 Ethanol Toxicity Experiment 120
5.2.4 Cell Growth Monitoring 120
5.2.5 Image Processing 121
5.2.6 ISFODS for Metabolic Activity Measurement 121
5.2.7 Linearity Calibration of Fluorescence Intensity 125
5.2.8 96-well Plate Experiment for Cell Metabolic Activity Measurement 125
5.2.9 Mathematical Simulation 126
5.3 Results 131
5.3.1 Ethanol Toxicity Experiment 131
5.3.2 CalceinAM Injection and Cell Staining Experiment 135
5.3.3 Cell Growth Monitoring 135
5.3.4 Linearity Calibration of Resorufin Fluorescent Intensity 138
5.3.5 Measurement of P450 1A1/1A2 Enzyme Activity of HepG2/C3A Cells in a 96-well Plate and a μCCA 140
5.4 Discussion 145
5.4.1 Ethanol Toxicity and CalceinAM Staining 145
5.4.2 Cell Growth Monitoring with ISFODS 147
5.4.3 Enzyme Activity Monitoring in μCCA 148
5.5 Conclusion 149
6. A MICROFLUIDIC DEVICE FOR A PHARMACOKINETIC-PHARMACODYNAMIC (PK-PD) MODEL ON A CHIP 152
6.1 Introduction 152
6.2 Materials and Methods 154
6.2.1 Cell Culture and Chemicals 154
6.2.3 Device Assembly and Operation 157
6.2.4 Pharmacokinetic-Pharmacodynamic (PK-PD) Modeling 160
6.3 Results 163
6.3.1 Device Assembly and Gravity-induced Flow 163
6.3.2 Construction of PK-PD model 167
6.3.3 Effect of Uracil as a Modulator 170
6.4 Discussion 175
6.4.1 Advantages of Layered Design 175

6.4.2 Insights from a PK-PD Model of a μCCA 177
6.4.3 Effect of Encapsulating Matrix on Cell Function..... 180
6.5 Conclusion..... 181
7. FINAL CONCLUDING REMARKS AND FUTURE DIRECTIONS..... 186

LIST OF TABLES

Table 2.1 Physiological values 22
Table 2.2 Partition coefficients 23
Table 2.3 Kinetic parameters 26
Table 2.4 Parameters for the pharmacodynamic models 32
Table 3.1 Parameters used in the simulation of diffusion of calcein AM in alginate 70
Table 3.2 Boundary and sub-domain conditions used in the simulation of diffusion of calcein AM in alginate. N-S: Navier-Stokes, C-D: Convection-diffusion model 70
Table 3.3 Comparison of calculated residence times and velocities in each chamber with measured values. 72
Table 4.1 Residence times of flow in each chamber in a microfluidic device attached after a separate bubble trap module. 105
Table 4.2 Residence times of flow in each chamber in a microfluidic device with integrated bubble trap. 105
Table 5.1 Parameters used in the simulation of a well-mixed model and a convection-diffusion (C-D) model. 129
Table 5.2 Boundary and sub-domain conditions used in the simulation of a convection-diffusion model. N-S: Navier-Stokes, C-D: Convection and Diffusion. 130
Table 6.1 Parameters for the PK model of a μCCA 162
Table 6.2 Parameters for a PD model in static condition 173
Table 6.3 Parameters for a PD model in a μCCA 173

LIST OF FIGURES

Figure 2.1 Mechanism of Tegafur and 5-fluorouracil (5-FU) metabolism. 18
Figure 2.2 Structure of a PBPK model 19
Figure 2.3 Pharmacodynamic models to simulate the growth of tumor cells 31
Figure 2.4 PK profiles after Tegafur or uracil administration 35
Figure 2.5 PK profiles after UFT administration 36
Figure 2.6 Comparison of PD model simulation with experimental result 39
Figure 2.7 PK-PD model simulation for tumor growth in a rat 40
Figure 2.8 Simulation of cell growth with various combination ratios 41
Figure 2.9 Simulation of cell growth for various DPD activities 43
Figure 2.10 Effect of U:FT ratio on efficacy and toxicity of UFT 45
Figure 2.11 Simulation of pharmacokinetic-modulating chemotherapy (PMC) 46
Figure 3.1 A mathematical PBPK model and a corresponding μCCA 62
Figure 3.2 Incorporation of hydrogel into a μCCA 65
Figure 3.3 Assembly and operation of a μCCA 66
Figure 3.4 Steps of image processing of live cells stained with CalceinAM. 69
Figure 3.5 Pictures of live/dead staining of cells cultured in a μCCA. 73
Figure 3.6 Morphology of tumor and liver cells cultured in Matrigel and in monolayer in a μCCA. 75
Figure 3.7 Cytotoxicity of Tegafur on tumor cells 78
Figure 3.8 Cytotoxicity of Tegafur on liver and marrow cells 79
Figure 3.9 Formation of gradient in alginate hydrogel inside a μCCA 81
Figure 4.1 The schematic diagrams of design of a bubble trap 96
Figure 4.2 Pictures of a bubble trap 96
Figure 4.3 Testing bubble trap efficiency 102
Figure 4.4 Finite-element simulation of the flow inside a bubble trap. 104
Figure 4.5 Cell culture compatibility of a bubble trap 108
Figure 5.1 Overview of ISFODS for cell viability measurement 118
Figure 5.2 A μCCA used with ISFODS for cell viability measurement. 119
Figure 5.3 *In situ* fluorescence optical detection system (ISFODS) for enzyme activity measurement. 124
Figure 5.4 Mathematical models describing the micro cell culture analog system and a detection chamber. 128

Figure 5.5 Time course of cell viability index in response to ethanol 132
Figure 5.6 Exposure of cells to ethanol 133
Figure 5.7 Necrosis time constant at various ethanol concentrations 134
Figure 5.8 Staining/cell death experiment 136
Figure 5.9 Cell growth of MESSA H2B-GFP and HepG2-C3A cells in a μCCA 137
Figure 5.10 Linearity calibration of ISFODS 139
Figure 5.11 P450 1A1/1A2 activity of HepG2/C3A cells as measured by the formation of resorufin 142
Figure 5.12 Simulated and measured resorufin formation at different substrate concentrations 144
Figure 5.13 Simulated and measured resorufin formation at varying cell concentration. 144
Figure 5.14 P450 1A1/1A2 activities of chemically induced HepG2/C3A cells 146
Figure 6.1 Schematics of device assembly 159
Figure 6.2 A μCCA and corresponding PBPK and PD models 161
Figure 6.3 Sealing of device 165
Figure 6.4 Gravity-induced flow 166
Figure 6.5 Live/dead staining of cells 168
Figure 6.6 Measured and simulated cell viability in static condition 171
Figure 6.7 Measured and simulated cell viability in a μCCA 172
Figure 6.8 Effect of uracil as a modulator 174
Figure 6.9 Comparison of PK profile for different modes of recirculation 178

LIST OF ABBREVIATIONS

μCCA: Microscale cell culture analog

PK: Pharmacokinetic

PD: Pharmacodynamic

PBPK: Physiologically based pharmacokinetic

FT: Tegafur

5-FU: 5-fluorouracil

U: Uracil

3-MC: 3-methylcholanthrene

EtOH: Ethanol

ISFODS: *In situ* fluorescence optical detection system

C-D: Convection-diffusion

CHAPTER 1

INTRODUCTION

1.1 Motivation

Drug development is a complex process, requiring knowledge from pharmacology, cell and molecular biology, chemistry and mathematics. Completion of a drug development process takes many years, and only one in ten drugs entering clinical trials reaches the market, making the drug discovery process a high-risk enterprise (Dingemanse and Appel-Dingemanse 2007). These aspects render drug development expensive, both in terms of cost and time. It is estimated that the cost of drug development is approximately $US 900 million per new drug (Kola and Landis 2004). In addition, pharmaceutical companies are suffering from decreasing productivity with a decreasing number of new drugs each year. Based on a report by Kola and Landis, the average success rate in all therapeutic areas is approximately 11%, and success rates in some therapeutic areas are even lower, such as 5% success rate for oncology drugs (Kola and Landis 2004). In this report, the analysis on the underlying causes of attrition reveals that a significant portion of drug candidates fail due to lack of efficacy or unforeseen toxicity.

Typically, the drug development process consists of three main stages; preclinical *in vitro* testing, animal testing, and human clinical trials. *In vitro* testing typically involves a cell-based multi-well plate system (96-well plate or 384-well plate), where cells are exposed to drug candidates and the response is analyzed. A cell-based assay system can provide human cell-specific responses to the drug candidate, but is an incomplete model as it does not provide the responses due to multi-organ interactions. In addition, cell lines cultured *in vitro* often do not provide the same

responses as the cells *in vivo*, which makes the human cultured cell model incomplete. While the whole body response to a drug can be obtained from clinical trials, testing drug candidates in humans is met with serious challenges in resources such as time and cost. Animal models have been used as an alternative approach to human clinical trials, such as rodents and nonhuman primates. However, animal models are also expensive and carry ethical issues. More importantly, the extrapolation of animal to human model does not always guarantee successful prediction of human response to a drug candidate. Therefore, it is of paramount importance to develop an improved *in vitro* model system that is predictive of human response. This is especially true with oncology drugs, where animal models are known to have a high unpredictability for human response (Booth et al. 2003).

A mathematical modeling approach such as pharmacokinetic-pharmacodynamic (Agoram et al. 2007) modeling has made significant contributions to the drug development process. Pharmacokinetics, which relates the administered dose of a drug to its concentration profiles in plasma and at a target site, evaluates drug absorption, distribution, metabolism and elimination characteristics, collectively known as ADME. On the other hand, pharmacodynamics examines the pharmacological effect of a drug at a given concentration at the target site. When combined together, PK-PD models aim to predict the time course of pharmacological effect after a given dosing regimen. The role of PK-PD models in drug discovery process has been emphasized in several review papers (Derendorf and Meibohm 1999; Perez-Urizar et al. 2000; Meibohm and Derendorf 2002; Karlsson et al. 2005; Dingemanse and Appel-Dingemanse 2007), but the impact of a PK-PD modeling approach has been limited due to several obstacles, including the problems of finding optimal parameters and inaccurate predictions due to unknown mechanism of action.

Recently, the advance in micro and nanofabrication technology has enabled development of a new research area called microfluidics (Whitesides 2006), and microfluidic systems with novel design have been shown to be ideal for attacking problems in cell biology, tissue engineering and drug discovery (Beebe et al. 2002; Li et al. 2003; El-Ali et al. 2006; Kang et al. 2008). The microscale nature of such systems makes it appropriate for addressing questions more relevant to the physiological situation *in vivo* (Breslauer et al. 2006). Furthermore, microfluidics is ideal for building a system with multiple compartments and connecting them to reproduce multi-organ interaction. Such a capability can be exploited to develop a 'body-on-a-chip' device, as will be described in this dissertation.

Although microfluidics is a useful and powerful technology in its own right, it has great potential for improving the drug development process when combined with a mathematical modeling approach, such as PK-PD models. A carefully designed microfluidic system can compensate for some of the drawbacks of PK-PD modeling system, and a quantitative mathematical analysis by PK-PD modeling can guide the design of a physiologically realistic microfluidic system and help researchers interpret the experimental result with greater insight. Currently, a mathematical approach combined with microfluidic systems has been primarily applied to the simulation of transport phenomenon only (Roy et al. 2001; Mehta and Linderman 2006; Zeng et al. 2006), and there are few examples of mathematical models for the pharmacological effect of a drug on cells in a microfluidic system. We believe that the combined approach of PK-PD modeling and microfluidic systems has a great potential for a synergistic outcome, and will describe efforts for the realization of a 'PK-PD model on a chip'.

1.2 Integrated Pharmacokinetic-Pharmacodynamic (PK-PD) Modeling

The term pharmacokinetics refers to the prediction of time-dependent concentrations of a substance in a living system (Gerlowski and Jain 1983). It examines drug absorption, distribution, metabolism and elimination, collectively known as ADME, which determines the disposition of the drug within an organism. A pharmacokinetic model attempts to predict the concentration profile of a drug in the blood or at the target site from a given dose, as well as the values of pharmacokinetic parameters such as clearance rate and half-life. Predicting pharmacokinetics prior to the clinical phase of drug development has been shown to be useful, especially in the selection of dosages in the clinical studies, which resulted in significant time-savings (Reigner et al. 1997). Several commercial PK modeling software packages are available on the market, including GastroPlus, SIMCYP, Cloe PK (Willmann et al. 2003; Agoram et al. 2007).

Pharmacodynamics refers to the time course of a drug's pharmacological effect at the target site for a given target concentration. In short, pharmacokinetics studies 'what the body does to the drug', whereas pharmacodynamics characterizes 'what the drug does to the body' (Holford and Sheiner 1982). The basis of pharmacodynamics is that the pharmacological effect of a drug is a function of its concentration at the target site. The pharmacological effect of a drug is modeled using a drug concentration as a variable, whose exact form will differ depending on the type and the pharmacological effect of the drug. Pharmacokinetics and pharmacodynamics characterize different realms of pharmacology, but when integrated, PK-PD models can provide a description of the time course of a drug's effects in response to a dosage regimen (Derendorf and Meibohm 1999; Dingemanse and Appel-Dingemanse 2007).

To develop an integrated PK-PD model, concentration profiles of a drug in different organs are computed using a pharmacokinetic model, and the pharmacodynamic model is used to predict the pharmacological effect based on the concentration profile of a drug in a target organ. For example, if one builds a PK-PD model for an oncology drug, the concentration profile of a drug in the tumor compartment will serve as an input for a PD model, which simulates the tumor growth in the presence of the drug. Therefore, one can predict the growth kinetics of the tumor for a given dose of the drug (Simeoni et al. 2004). Integrated PK-PD modeling can be versatile and can be applied to dosing and scheduling determination (Friberg et al. 2000), dosing individualization (Holford 1995), formulation development (Aarons et al. 2001) and toxicity assessment (Latz et al. 2006). Currently, use of PK-PD modeling is limited to early drug development phase and research applications only. Before PK-PD models can be utilized more broadly, obstacles both in the area of PK and PD modeling must be overcome. A limiting factor for building a realistic model is that while some parameters are relatively easy to find either in the literature or experimentally, some parameters are extremely difficult to estimate, especially for a human model. Although it is possible to optimize the model and find the parameters given sufficient data, data for human parameters are sparse. Usually during the drug development process, a PBPK model for animal is built first to validate the PK-PD modeling approach. An animal model is easier to build than a human model, because animal data are more readily available. If the animal model can predict animal response with reasonable accuracy, then a human model is considered. However, verification in an animal model does not necessarily warrant the development of a human model, since extrapolation of an animal model to a human model is not always straightforward.

1.3 Previous Works in Micro Cell Culture Analog (μCCA)

Initially, the prototype cell culture analog (CCA) device used for a proof-of-concept study was described by Sweeney (Sweeney 1995). In this prototype, two milk dilution bottles and a spinner flask were connected using Teflon FEP tubes, and recirculation was achieved using peristaltic pumps. The glass bottles represented the lung and liver compartments, and the 'other tissues' compartment was represented by a glass reaction beaker. The system was the first prototype for a multi-compartment system with multiple cell types with fluid recirculation. The major limitations of this prototype were the non-physiological residence times in each chamber and an unrealistic ratio of liver-to-lung cells (Shuler 1996). Also the difficulty with stable operation of the device and obtaining time course data were limitations of the prototype system. An improved macroscale system was designed to mimic the physiological organ characteristics of a rat more closely than the prototype CCA (Ghanem and Shuler 2000). The CCA system used cells attached to microcarrier beads, which formed packed beds with cell culture medium recirculating through the beds. The main advantage of packed beds rather than a monolayer cell culture was that a higher cell density was achievable, providing a more realistic liquid-to-cell ratio, and medium residence times were closer to *in vivo* values. With this second generation, packed beds CCA device, several aspects of the device operation was examined, including mixing profiles, naphthalene distribution profile and the effect of reactor environment on cell viability. These systems were validated using naphthalene as a model drug, and the experimental results were shown to match with the prediction by a mathematical physiologically-based pharmacokinetic (PBPK) model.

Although the concept of a cell culture analog (CCA) as a physical realization of a PBPK model has been validated, still there were several obstacles to overcome.

The liquid-to-cell ratio was about 1000:1 in the first prototype and 5:1 in the second generation system compared to the physiological ratio of 1:2. Conventional 2-D monolayer culture methods using standard culture flasks or wells also have liquid volumes greater than the volume of the cell layer. As the cells are exposed to environment that is completely different from their native environment, it is not surprising that many cells exhibit a different behavior when separated from their native tissue and cultured by conventional methods (Cushing and Anseth 2007). Secondly, early versions of CCA devices did not have physiologically realistic residence times in organ chambers. For example, the residence time for the liver chamber in the packed bed CCA device was 1.9 min, whereas the actual residence time for the liver in a rat is about 21.3 seconds (Ghanem and Shuler 2000). A PBPK model is based on physiological parameters such as blood flow rates and organ sizes, and a faithful realization of the PBPK model is achieved only if the residence times in each chamber are close to the actual values, because inaccurate residence times in organ chambers could distort a pharmacokinetic-pharmacodynamic response, not correctly reflecting physiological responses in the body.

These limitations of macroscale CCA devices together with advances in microfluidic technology spurred the development of a microscale CCA (μCCA), which is a miniaturized version of the earlier CCA devices (Sin et al. 2004). It should be noted that the term 'micro (μ)' has been added to emphasize the microscale nature of the device. A cell culture analog device in microscale confers several advantages. 1) The natural length scales in tissue are order of 100 μm from capillary blood flow with cells on order of 10 – 20 μm in size; these dimensions can be easily mimicked in the microscale systems. This allows more realistic residence times and relative organ sizes, because the flow rate and the geometry of a microfluidic device can be precisely controlled using microfabrication techniques. 2) Being in microscale, fewer cells and

less test chemical are required, which enables the use of scarce tissue samples and novel compounds. Authentic tissue samples provide more realistic representations of *in vivo* environment. A system requiring small amounts of test chemicals would enable high throughput experiments with newly developed, novel molecules. 3) The small size of the device facilitates operation of multiple devices concurrently, which enables high throughput assays. Miniaturization also allows integration of the system with other components necessary for drug testing, such as sample analysis and optical detection. 4) Once a master device has been fabricated, subsequent devices can be made very cheaply, reducing the cost of fabrication for mass parallelization.

The μCCA device was tested using naphthalene as a model toxicant (Viravaidya et al. 2004). Since the majority of naphthalene toxicity affects the lung, a rat lung cell line (L2) was cultured in the lung compartment, and a rat or human hepatoma cell line (H4IIE or HepG2/C3A) was cultured in the liver compartment. In this study, naphthalene was added to the circulating media in a μCCA device, and the viability of L2 (lung) and HepG2/C3A (liver) cells were tested by MCB staining for GSH. The results showed that after naphthalene was added to the medium, the GSH levels in lung and liver cells continuously decreased for the duration of the experiment, demonstrating the toxic effect of naphthalene on the cells. To verify that the HepG2/C3A (liver) cells were responsible for the observed cytotoxicity of the naphthalene in the μCCA, control experiments were performed where the liver chamber was empty. When HepG2/C3A (liver) cells were not present in the μCCA device, the cytotoxic effect of naphthalene was not observed, as manifested by high level of GSH in L2 (lung) cells. Further experiments with several metabolites of naphthalene including naphthoquinone, naphthol, and naphthalene dihydrodiol revealed that naphthoquinone was responsible for the toxicity of naphthalene in the μCCA with a dose-dependent response (Viravaidya et al. 2004).

1.4 Specific Goals and Outlines

The ultimate goal of this thesis work is to develop an integrated system that combines a mathematical pharmacokinetic-pharmacodynamic (PK-PD) model and an experimental platform (μCCA), with a specific focus on a chemotherapeutic agent for colon cancer. As will be discussed throughout this thesis work, achieving this goal requires combination of different research disciplines, and this thesis work is divided into five chapters, which are organized as follows. In the second chapter, the development of a mathematical model will be described, which predicts the growth of tumor in the rat after administration of a drug for colon cancer. A physiologically-based pharmacokinetic (PBPK) model is developed first, and combined with a pharmacodynamic (PD) model which describes the growth of tumor in a rat in the presence of a drug. The developed model is validated by comparing with experimental data from existing literature, and different dosing regimens are tested using the model. In the third chapter, a micro cell culture analog (μCCA) is developed to test the cytotoxic effect of a drug. The μCCA described in this chapter is based on the previous work by Sin and Viravaidya (Sin et al. 2004; Viravaidya et al. 2004), with two major modifications. First, the three-chamber μCCA is designed for specifically assessing the toxicity of a drug for colon cancer. Secondly, instead of 2-D monolayer cell cultures, cells are encapsulated in hydrogel, Matrigel or alginate, inside the chambers. The μCCA is used to quantify the cytotoxic effect of the drug on colon cancer cell line, hepatoma cell line, and myeloblasts, representing tumor, liver, and bone marrow, respectively. One of the requirements for testing the cytotoxic effect of a cancer drug is that cells need to be cultured for a relatively long-term (several days), as opposed to a short-term culture used in the previous naphthalene study (several hours). Several issues need to be overcome to achieve the operation of a μCCA for

several days, such as prevention of bacterial contamination, complete sealing of the device, and prevention of air bubble formation. The fourth chapter describes a microscale bubble trap to prevent the formation of air bubbles inside a μCCA. It is designed to trap bubbles with a large enough size to cause blockage of channels in a μCCA, and dramatically enhanced the operation of a μCCA. Devices in a microscale offer several advantages, but also results in limitations in detection and analysis of the system. The fifth chapter describes an *in situ*, fluorescence optical detection system (ISFODS), which is designed to be integrated with a μCCA for real-time measurement of cell viability or cell metabolic activity. The last chapter depicts development of a new μCCA, with specific purpose of incorporating 3-D hydrogel cell cultures in the device. Several improvements have been made over the original μCCA described in the third chapter, including elimination of bubble formation, better consistency in the operation, and easier implementation of high-throughput experiment. It is demonstrated that the μCCA can used for assessing the toxicity of a chemotherapeutic agent, and a corresponding PK-PD model is developed to describe the action of the drug in the device.

REFERENCES

Aarons, L., et al. (2001). "Role of modelling and simulation in Phase I drug development." Eur J Pharm Sci 13(2): 115-22.

Agoram, B. M., et al. (2007). "The role of mechanism-based pharmacokinetic-pharmacodynamic (PK-PD) modelling in translational research of biologics." Drug Discov Today 12(23-24): 1018-24.

Beebe, D. J., et al. (2002). "Physics and applications of microfluidics in biology." Annu Rev Biomed Eng 4: 261-86.

Booth, B., et al. (2003). "Oncology's trials." Nat Rev Drug Discov 2(8): 609-10.

Breslauer, D. N., et al. (2006). "Microfluidics-based systems biology." Mol Biosyst 2(2): 97-112.

Cushing, M. C. and K. S. Anseth (2007). "Materials science. Hydrogel cell cultures." Science 316(5828): 1133-4.

Derendorf, H. and B. Meibohm (1999). "Modeling of pharmacokinetic/pharmacodynamic (PK/PD) relationships: concepts and perspectives." Pharm Res 16(2): 176-85.

Dingemanse, J. and S. Appel-Dingemanse (2007). "Integrated pharmacokinetics and pharmacodynamics in drug development." Clin Pharmacokinet 46(9): 713-37.

El-Ali, J., et al. (2006). "Cells on chips." Nature 442(7101): 403-11.

Friberg, L. E., et al. (2000). "Models of schedule dependent haematological toxicity of 2'-deoxy-2'-methylidenecytidine (DMDC)." Eur J Clin Pharmacol 56(8): 567-74.

Gerlowski, L. E. and R. K. Jain (1983). "Physiologically based pharmacokinetic modeling: principles and applications." J Pharm Sci 72(10): 1103-27.

Ghanem, A. and M. L. Shuler (2000). "Characterization of a perfusion reactor utilizing mammalian cells on microcarrier beads." Biotechnol Prog 16(3): 471-9.

Ghanem, A. and M. L. Shuler (2000). "Combining cell culture analogue reactor designs and PBPK models to probe mechanisms of naphthalene toxicity." Biotechnol Prog 16(3): 334-45.

Holford, N. H. (1995). "The target concentration approach to clinical drug development." Clin Pharmacokinet 29(5): 287-91.

Holford, N. H. and L. B. Sheiner (1982). "Kinetics of pharmacologic response." Pharmacol Ther 16(2): 143-66.

Kang, L., et al. (2008). "Microfluidics for drug discovery and development: from target selection to product lifecycle management." Drug Discov Today 13(1-2): 1-13.

Karlsson, M. O., et al. (2005). "Pharmacokinetic/pharmacodynamic modelling in oncological drug development." Basic Clin Pharmacol Toxicol 96(3): 206-11.

Kola, I. and J. Landis (2004). "Can the pharmaceutical industry reduce attrition rates?" Nat Rev Drug Discov 3(8): 711-5.

Latz, J. E., et al. (2006). "A semimechanistic-physiologic population pharmacokinetic/pharmacodynamic model for neutropenia following pemetrexed therapy." Cancer Chemother Pharmacol 57(4): 412-26.

Li, N., et al. (2003). "Biology on a chip: microfabrication for studying the behavior of cultured cells." Crit Rev Biomed Eng 31(5-6): 423-88.

Mehta, K. and J. J. Linderman (2006). "Model-based analysis and design of a microchannel reactor for tissue engineering." Biotechnol Bioeng 94(3): 596-609.

Meibohm, B. and H. Derendorf (2002). "Pharmacokinetic/pharmacodynamic studies in drug product development." J Pharm Sci 91(1): 18-31.

Perez-Urizar, J., et al. (2000). "Pharmacokinetic-pharmacodynamic modeling: why?" Arch Med Res 31(6): 539-45.

Reigner, B. G., et al. (1997). "An evaluation of the integration of pharmacokinetic and pharmacodynamic principles in clinical drug development. Experience within Hoffmann La Roche." Clin Pharmacokinet 33(2): 142-52.

Roy, P., et al. (2001). "Analysis of oxygen transport to hepatocytes in a flat-plate microchannel bioreactor." Ann Biomed Eng 29(11): 947-55.

Shuler, M. L., Ghanem, A., Quick, D., Wong, M. C., Miller, P. (1996). "A self-regulating cell culture analog device to mimic animal and human toxicological responses." Biotecnology and bioengineering 52(1): 45-60.

Simeoni, M., et al. (2004). "Predictive pharmacokinetic-pharmacodynamic modeling of tumor growth kinetics in xenograft models after administration of anticancer agents." Cancer Res 64(3): 1094-101.

Sin, A., et al. (2004). "The design and fabrication of three-chamber microscale cell culture analog devices with integrated dissolved oxygen sensors." Biotechnol Prog 20(1): 338-45.

Sweeney, L. M., Shuler, M. L., Babish, J. G., Ghanem, A. (1995). "A cell culture analogue of rodent physiology: application to naphthalene toxicology." Toxicology in vitro 9(3): 307-316.

Viravaidya, K., et al. (2004). "Development of a microscale cell culture analog to probe naphthalene toxicity." Biotechnol Prog 20(1): 316-23.

Whitesides, G. M. (2006). "The origins and the future of microfluidics." Nature 442(7101): 368-73.

Willmann, S., et al. (2003). "PK-Sim: a physiologically based pharmacokinetic 'whole-body' model." Biosilico 1(4): 121-124.

Zeng, Y., et al. (2006). "Mass transport and shear stress in a microchannel bioreactor: numerical simulation and dynamic similarity." J Biomech Eng 128(2): 185-93.

CHAPTER 2

COMBINED PHARMACOKINETIC-PHARMACODYNAMIC (PK-PD) MODEL FOR TUMOR GROWTH IN THE RAT AFTER UFT ADMINISTRATION[1]

2.1 Introduction

Drug development is an expensive, time-consuming process. According to Adams et al., drug development cost ranges from $500 million to $2,000 million per new drug, depending on the therapy and the developing firm (Adams and Brantner). Even after the development and approval of drug to the market, the optimal dosing schedule and regimen remain uncertain. For example, the chemotherapeutic drug 5-fluorouracil (5-FU) was developed several decades ago and has been widely used, but the optimal method of using this drug is still in debate (Goyle and Maraveyas 2005; Kelder et al. 2006). Finding an optimal dosing strategy is a difficult, expensive task that involves a large number of patients and a long period of time, especially for oncology drugs. In addition, the inherent metabolic and physiologic variations in patients result in patients responding differently to the same dosing regimen (Deeken et al. 2007). Pharmacogenetics, which studies the effect of genetic variations on responses of patients to drugs and attempts to tailor the dosing strategy for each individual patient, attempts to address this issue (Relling and Dervieux 2001; Park et al. 2003). Considering this individual genetic variation further complicates the problem of dose optimization because it is virtually impossible to perform such a large number of tests on each individual.

[1] This chapter has been modified from an article Sung, J. H., et al. (2009). "A combined pharmacokinetic-pharmacodynamic (PK-PD) model for tumor growth in the rat with UFT administration." J Pharm Sci 98(5): 1885-904, with permission of Wiley Interscience.

A mathematical approach such as a pharmacokinetic-pharmacodynamic (PK-PD) model is a feasible alternative as it can link the administration regimen to patient response in terms of tumor growth (Simeoni et al. 2004). In this chapter, a PBPK model is developed to describe the concentration profiles of a chemotherapeutic drug administered in a rat, and a PD model is developed to describe the tumor growth kinetics in the presence of the drug. The PBPK model and the PD model are then combined together to predict the growth of tumor in a rat. The combined PK-PD model is used to find the optimal combination ratio of the drugs, and to test the effect of variation in the metabolizing enzyme level. Also a new dosing strategy to maximize the drug efficacy is tested. Such a model should be an effective guide towards rapid evaluation of treatment strategies and can be a useful tool for patient specific chemotherapy if levels of key enzymes in an individual are known.

2.2 Methods

2.2.1 Experimental Background for Model Development

Colorectal cancer ranks second as a cause of cancer related deaths (Pasetto et al. 2006). Since the discovery by C. Heidelberger in 1957 (Heidelberger et al. 1957), 5-fluorouracil (5-FU) has been the most widely accepted chemotherapeutic agent for colorectal cancer. 5-FU was developed based on the study conducted by Rutman et al. that rat hepatomas used the pyrimidine uracil more rapidly than other normal tissues (Rutman et al. 1954), implying that uracil metabolism can be a target for chemotherapeutic agents (Gill et al. 2003). 5-FU can be classified as an antimetabolite drug that is synthesized by substitution of fluorine for hydrogen in uracil. The mechanism of cytotoxicity of 5-FU has been ascribed to several factors including the misincorporation of fluoronucleotides into RNA and DNA, and to the inhibition of

nucleotide synthetic enzyme thymidylate synthase (TS). Although it is not clear which mechanism of action mainly contributes to the cytotoxic effect of 5-FU, the mechanism of action depends on 5-FU concentration, and other factors (Yoshikawa et al. 2001). It has been reported that the dysfunction of RNA can be achieved only when 5-FU concentration is high (10-100μM) (Spiegelman et al. 1980), while DNA synthesis can be inhibited at lower 5-FU concentration (0.5-1.0μM) (Parker and Cheng 1990).

The catabolism of 5-FU is achieved mainly through the enzyme called dihydropyrimidine dehydrogenase (DPD), which is located primarily in the liver. DPD catalyzes the conversion of 5-FU to fluoro-5,6-dihydrouracil, and is the rate limiting step in the catabolism of 5-FU (Lu et al. 1993). About 80% of the administered 5-FU is degraded by DPD (Heggie et al. 1987). Since DPD plays such an important role in the catabolism of 5-FU, the relationship between the activity of DPD enzyme and the response of patients to 5-FU related chemotherapy has been studied extensively, in the expectation of using the DPD enzyme activity as a predictive marker for 5-FU related chemotherapy. It has been found that DPD expression is inversely related to the efficacy of 5-FU, that is 5-FU was less effective with higher DPD expression level (Ichikawa et al. 2003; Kornmann et al. 2003). 5-FU related toxicity has also been found to be closely related to the DPD activity. Mutations and single nucleotide polymorphisms (SNPs) can cause deficiencies in DPD enzymatic activity, and patients with DPD deficiencies have a reduced capacity to metabolize 5-FU and are at risk of developing severe toxic reactions (Wei et al. 1996; van Kuilenburg 2004; Deeken et al. 2007). Based on these findings, individualization of 5-FU chemotherapy has been proposed (Park et al. 2003; Ploylearmsaeng et al. 2006). For example, the expression level of DPD enzyme can be tested and the dose can be reduced in case of patients with low levels of DPD activity.

The bioavailability of 5-FU has been shown to be unpredictable, especially after oral administration (Hahn et al. 1975). In addition, administered 5-FU is rapidly degraded into F-β-alanine by DPD, and the half-life time of the administered 5-FU *in vivo* has been reported to be only 10-20 minutes (Pinedo and Peters 1988). An oral prodrug of 5-FU such as Tegafur (tetrahydrofuranyl-5-fluorouracil, Ftorafur, FT) has been developed to achieve a better bioavailability and a more stable concentration profile of 5-FU after oral administration. Tegafur has no cytotoxic effects *in vitro*, but when it is administered *in vivo*, it is converted to 5-FU by the cytochrome p450 enzyme system mainly in the liver (de Bono and Twelves 2001). The metabolic pathway of Tegafur and 5-FU is shown in Figure 2.1. Several isozymes of CYP450 enzymes are known to be responsible for the conversion, including 1A2, 2A6 and 3A5 (Komatsu et al. 2000). In addition, Tegafur can be converted to 5-FU by thymidine phosphorylase (TP) in the liver, small intestine and tumor tissues, or can be converted into 5-FU spontaneously *in vivo* (Tanaka et al. 2000). To enhance the therapeutic index of the drug, UFT was developed, which is a combination of uracil and Tegafur in a molar ratio of 4 to 1. Uracil is a natural substrate of DPD enzyme, therefore it competes with 5-FU and acts as a modulator of 5-FU catabolism (Malet-Martino and Martino 2002). The molar ratio of 4 to 1 was chosen because this ratio gave the best tumor selectivity in rats in a preclinical test (Fujii et al. 1979).

2.2.2 Physiologically-based Pharmacokinetic (PBPK) Model Structure

The PBPK model in Figure 2.2 consists of seven compartments, which are assumed to be homogeneously well-mixed and equilibrated with exiting blood. The only exception is the liver compartment for uracil, where the vascular and the tissue space were separated to describe the distinctively low uracil concentration in the liver.

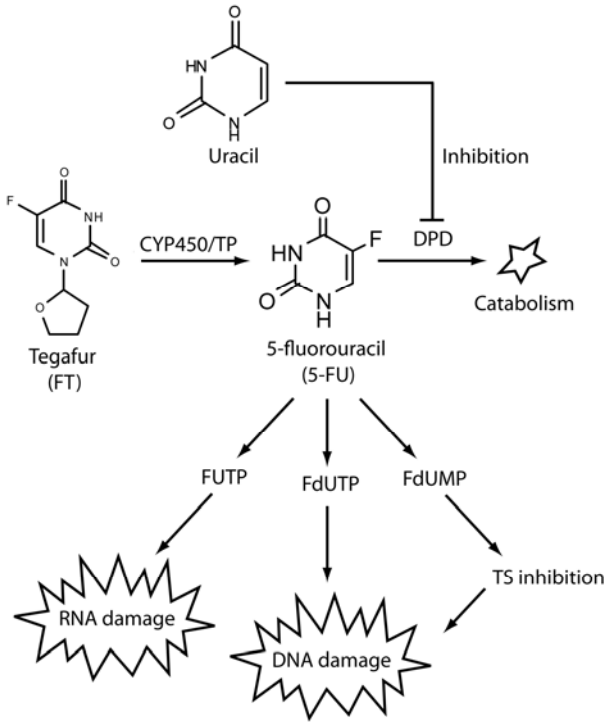

Figure 2.1 Mechanism of Tegafur and 5-fluorouracil (5-FU) metabolism.

Tegafur (FT) is metabolized to 5-FU mainly by P450 enzymes in the liver. 5-FU is further metabolized and exerts cytotoxic effect via RNA inhibition and DNA inhibition. 5-FU is mainly degraded by dihydropyrimidine dehydrogenase (DPD). Uracil, which is a natural substrate of DPD, inhibits the degradation. UFT is a combination of uracil with Tegafur in a molar ratio of 4 to 1.

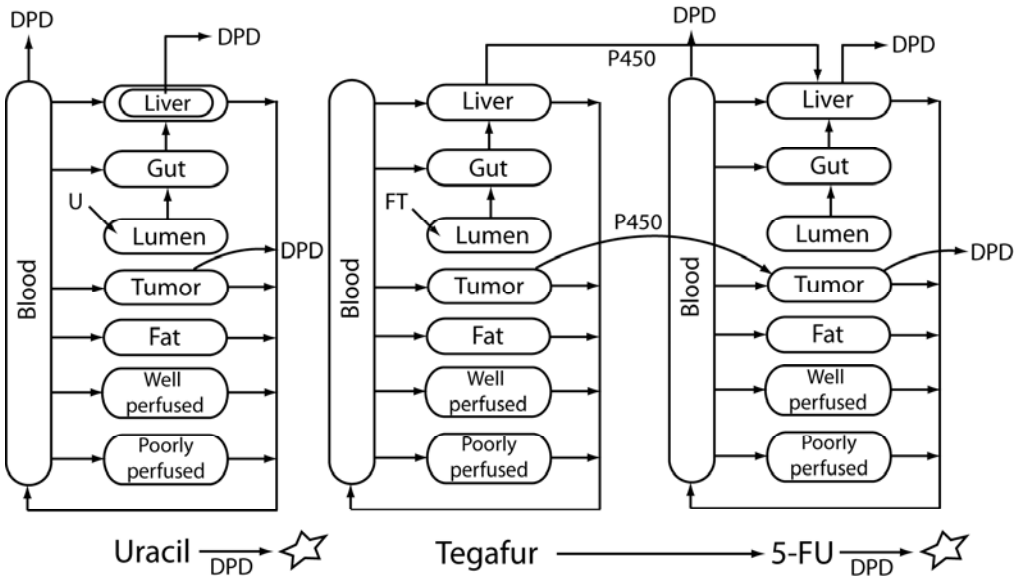

Figure 2.2 Structure of a PBPK model

Tegafur is converted to 5-FU mainly by P450 enzyme in the liver and the tumor compartment. Uracil and 5-FU are degraded by DPD enzyme and compete with each other. UFT is taken orally, therefore uracil and Tegafur starts in the lumen compartment in the model.

Tegafur and uracil are administered orally and the model starts with GI lumen compartment. It was assumed that Tegafur is converted to 5-FU in the liver and the tumor compartments (de Bono and Twelves 2001). Conversion in the gastrointestinal tract was assumed to be negligible since the main P450 enzyme responsible for the conversion is known to be active mainly in the liver (Yamazaki et al. 2001; Kajita et al. 2003). 5-FU and uracil were assumed to be metabolized by DPD in the liver, tumor, and the blood compartment (de Bono and Twelves 2001; Ichikawa et al. 2003; van Kuilenburg 2004).

Ordinary differential equations were used to describe the mass balance for each compound in compartments. The mass transfer between the blood and the organs was assumed to be limited by perfusion to the organs. It has been reported that 5-FU and uracil share a saturable transport system capable of rapid equilibration of these substrates across the cell membrane (Wohlhueter et al. 1980). Less is known about the transport of Tegafur across the cell membrane, but since Tegafur has a similar structure to 5-FU and uracil, we assumed that the transport of Tegafur was also rapid, and tested the hypothesis by evaluating the ability of the constructed model to fit to the concentration profiles of Tegafur.

The enzymatic conversion of Tegafur by cytochrome P450, the degradation of 5-FU by DPD and the metabolism of uracil were assumed to follow Michaelis-Menten kinetics. The degradation of 5-FU by DPD is inhibited by uracil by competitive inhibition, thus the equation that describes competitive inhibition was used to describe the inhibition kinetics (Adjei 1999). A software program, coded in C++, was written to solve the differential equations, implementing a 4th order Runge-Kutta algorithm. The same equations were also solved using ode45 function in Matlab (Mathworks, Natick, MA).

2.2.3 PBPK Model Parameters

Physiological parameters such as the volume of organs and blood flow rates were taken from the literature, with the weight of a rat assumed to be 220 grams (Davies and Morris 1993; Quick and Shuler 1999). All other major organs that were not modeled specifically in the PBPK model were lumped into either the well-perfused organ or the poorly-perfused organ compartments. The size of the tumor was assumed to be 1 gram, which was close to the average size of tumors in the study by Kawaguchi et al. (Kawaguchi et al. 1980), and 0.25 ml/min/g tissue of blood flow rate was calculated from Farris et al. (Farris et al. 1985), which is also close to the value found in Vaupel et al. (Vaupel et al. 1989). Physiological parameters used in the simulation are listed in Table 2.1.

The tissue-to-blood partition coefficients were calculated by the method of Poulin and Theil, which predicts partition coefficients based on n-octanol-water partition coefficients and the tissue composition (Poulin and Theil 2002). Rat tissue composition data used in the calculations were also taken from Poulin and Theil (Poulin and Theil 2002). A homogeneous distribution was assumed when partition coefficients were used to describe the distribution of the drugs. An effort was made to make as few changes as possible to the values of calculated partition coefficients. However, it was necessary in some cases to make some modifications to the values of partition coefficients to achieve an acceptable fit. The partition coefficient values used in the simulation are listed in Table 2.2.

Table 2.1 Physiological values

	Organ weight[a]	Blood flow rate (ml/min)[a]
Blood	13.2	76.45
Gut	7.92	17.1
Liver	8.8	19
Tumor	1.0[b]	0.25 [c]
Fat	15.4	38.9
Well perfused organs[e]	8.5	38.9
Poorly perfused organs[f]	165	11.4

All values were taken from Quick,(Quick and Shuler 1999) except the values for the tumor.

a. Tumor weight is assumed to be 1.0 gram, taken from the average tumor size from Kawaguchi (Kawaguchi et al. 1980).

b. 0.25 ml/min/g tissue was assumed, from Farris et al. (Farris et al. 1985).

c. In case of uracil in liver, 10% vascular space was assumed (Jain 1988).

d. Well perfused organs include kidney and lung

e. Poorly perfused organs include muscle, bone and skin.

Table 2.2 Partition coefficients[a]

	5-FU	Tegafur	uracil
Gut	0.794	0.808 (0.6)	0.793
Liver	0.759 (1.635)	0.768 (0.326)	N/A
Tumor [b]	0.5	0.895	0.793
Fat	0.169	0.336	0.153
Well perfused organs	0.826	0.834	0.825
Poorly perfused organs	0.795	0.800	0.795

a. In case where the parameter was adjusted, the adjusted values are shown in the parenthesis

b. Partition coefficients for tumor were adjusted to fit to data.

Biochemical parameters such as V_m and K_m for reactions based on Michaelis-Menten kinetics could be obtained from studies using rat liver homogenates or microsomes. However V_m parameters measured *in vitro* are often not representative of *in vivo* parameters. Our approach was to use the literature to make initial estimates of parameters and then to modify the kinetic parameters based on optimization routines to make a good fit to existing experimental animal data. The rate of absorption into gastrointestinal tract was estimated under the assumption that the drug was absorbed completely within 30 minutes (Borner et al. 2002). IC_{50} (concentration of uracil that shows 50% inhibition) values for the degradation of 5-FU is known to be about 18 μM (Tatsumi et al. 1987), but the K_i value for competitive inhibition of uracil was not available from the literature. Therefore, the inhibition constant was made adjustable to fit the experimental data, using 18μM as the starting value for the optimization. Since uracil and 5-FU compete for the same DPD enzyme, they inhibit the activity of DPD on each other. Appropriate inhibition terms were added to the equations describing the kinetics of both 5-FU and uracil.

2.2.4 Curve Fitting Procedure

Concentration profiles of three different compounds (5-FU, Tegafur and uracil) in four different organs (gut, liver, tumor and blood) for two different dosing conditions were fitted to the experimental data from literature (Kawaguchi et al. 1980). Curve fitting procedure was done by a standard weighted least square method (Jacobs and Institute of Mathematics and Its Applications. 1977) and a lsqnonlin routine of the optimization toolbox in the Matlab software (Mathworks, Natick, MA) was used. The weight of $1/y_i$ was given, where yi is the model solution at time point i. Since we tried to fit the concentration profiles of three different compounds in several different

organs, a systematic approach was required. In the first step, we took the data for the case where only uracil was administered. The parameters that were made adjustable were V_m and K_m values for uracil metabolism, and the absorption constant for the absorption of uracil in the gut. After the fitting, uracil clearance from the tumor compartment was ignored since the adjusted value of V_m was low and clearance from the tumor compartment was negligible. In the second step, we took the data for the case where only Tegafur was administered (without uracil), and parameters related to the metabolism of Tegafur were optimized. In this step the parameters that were made adjustable were V_m values of CYP450 enzymes in the liver and the tumor, the absorption constant for Tegafur in the gut, and the partition coefficients of Tegafur in the gut and the liver. The third step was to take 5-FU concentration profiles from the same condition (administration of Tegafur only), and use them to fit the parameters for the metabolism of 5-FU. The adjustable parameters were V_m values of DPD enzyme, and partition coefficients of 5-FU in the gut and the liver. Clearance of 5-FU from the blood was ignored since the adjusted value was low and contribution of 5-FU clearance from the blood was negligible. Having optimized the parameters involved in the metabolism of uracil, Tegafur and 5-FU, the only parameters left were those that are involved in the interaction between 5-FU and uracil via inhibition of DPD enzyme. In the fourth step, the uracil concentration profiles from administration of UFT (combination of uracil and Tegafur) were used to optimize the value of the inhibition constant for uracil degradation (ki_u). Subsequently 5-FU concentration profiles were taken and used to optimize the inhibition constant for 5-FU degradation (k_i). The optimization of the inhibition constants was done in an iterative manner, where after the fifth step we went back to the fourth step and re-did the optimization until the optimization results were consistent. The resulting optimized kinetic parameters are summarized in table 2.3.

Table 2.3 Kinetic parameters

Parameter	**Value**	**Description**
$V_{m,\ CYP,\ liver}$ (nmol/min/g tissue)	997 (52.1)	V_{max} for CYP450 enzyme in liver [a]
$K_{m,\ CYP,\ liver}$ (nmol/ml)	2700	Michaelis Menten constant [b]
$V_{m,\ CYP,\ tumor}$ (nmol/min/g tissue)	504	V_{max} for TP enzyme in tumor
$K_{m,\ CYP,\ tumor}$ (nmol/ml)	2700	Michaelis Menten constant
$V_{m,\ DPD,\ liver}$ (nmol/min/g tissue)	250.7 (192)	V_{max} for DPD enzyme in liver [c]
$K_{m,DPD,\ liver}$ (nmol/ml)	40	Michaelis Menten constant [d]
$V_{m,\ DPD,\ tumor}$ (nmol/min/g tissue)	16.2	V_{max} for DPD enzyme in tumor
$K_{m,DPD,\ tumor}$ (nmol/ml)	40	Michaelis Menten constant
$k_{abs,FT}$ (g/min)	1.29	Absorption coefficient for FT
$k_{abs,Uracil}$ (g/min)	0.0164	Absorption coefficient for uracil
K_i (nmol/ml)	20	Inhibition constant of 5-FU in liver
K_{i_U} (nmol/ml)	10	Inhibition constant for uracil in liver
K_{i_T}	5	Inhibition constant for 5-FU in tumor
CL_{FT} (ml/min)	1	Systemic clearance rate of FT
CL_{FU} (ml/min)	0.1	Systemic clearance rate of 5-FU
$V_{m,Uracil,L}$ (nmol/min/g tissue)	45	V_{max} for uracil clearance in liver
$K_{m,Uracil,L}$ (nmol/g tissue)	2	Michaelis Menten constant
$V_{m,Uracil,B}$ (nmol/min/g tissue)	10	V_{max} for uracil clearance in blood
$K_{m,Uracil\_B}$ (nmol/g tissue)	2	Michaelis Menten constant
k_{u_out}(nmol/min)	100	Transfer coefficient from tissue space to vascular space[e]

Table 2.3 (Continued)

k_{u_int}(nmol/min)	18.3	Transfer coefficient from vascular space to tissue space[e]

a. The value inside the parenthesis was calculated from literature and used as a starting value for the optimization, and the value outside is the optimized parameter. Vmax value of 0.95 nmol/min/mg protein was obtained from Yamazaki(Yamazaki et al. 2001) and converted to per g tissue basis by multiplying by microsomal protein content of 54.9 mg/g tissue, calculated from Quick (Quick and Shuler 1999). The microsomal protein needed to be converted to per g tissue basis before multiplying using the organ volume and weight data from Davies (Davies and Morris 1993).

b. Km value was taken from Yamazaki (Yamazaki et al. 2001) and was used without modification.

c. Calculated from Vmax value from Ikenaka (Ikenaka et al. 1979), which is 0.51 nmol/mg protein/min. The Vmax was converted to per g tissue basis by multiplying by total protein content in liver, which is 376.3 mg/g tissue, obtained from Quick (Quick and Shuler 1999). The total protein content needed to be converted to per g tissue basis before multiplying, using the organ volume and weight data from Davies (Davies and Morris 1993).

d. Km value taken from Ikenaka (Ikenaka et al. 1979).

e. Transfer coefficients between the tissue space and the vascular space of liver for uracil were obtained by fitting

f. For other parameters refer to the methods section.

2.2.5 Pharmacodynamic (PD) Model

To model the growth of tumor cells under the influence of 5-FU, three different pharmacodynamic models were used. The three PD models that were tested are, 1) a cell cycle phase-specific model, 2) transit compartment model, and 3) dual transit compartment model with two sets of transit compartments. The schematic representations of the three PD models are shown in Figure 2.3.

1) Cell cycle phase-specific model

$$\frac{dC_S}{dt} = k_g \cdot C_S \cdot (1 - C_S / C_{SS}) - k_{sr} \cdot C_S + k_{rs} \cdot C_R - K \cdot C_S \quad (2.1)$$

$$\frac{dC_R}{dt} = k_{sr} \cdot C_S - k_{rs} \cdot C_R - k_d \cdot C_R \quad (2.2)$$

$$K = \frac{K_{max} \cdot FU}{EC_{50} + FU} \quad (2.3)$$

5-FU is generally known to be cell cycle specific and cause S-phase arrest (Yoshikawa et al. 2001). This property can be characterized by using a two-compartment model, which separates the total cell population into sensitive (C_s) and resistant groups (C_r) (Mager et al. 2003). The first-order rate constant k_{sr} and k_{rs} refer to the rates of cell cycling between the two populations. k_g and k_d refer to the rates of cell growth and death, respectively. C_{ss} is the maximum cell number that can be reached due to space and nutrient limitation. K is the nonlinear function for the cell kill effect of the drug, described to follow Michaelis-Menten Kinetics. FU is the concentration of 5-FU, K_{max} is a maximal cell kill rate, and EC_{50} is a Michaelis constant.

2) Transit compartment model

$$\frac{dC}{dt} = k_g \cdot C \cdot (1 - C / C_{SS}) - K_n \cdot C \quad (2.4)$$

$$\frac{dK_1}{dt} = (K - K_1)/\tau \quad (2.5)$$

$$\frac{dK_2}{dt} = (K_1 - K_2)/\tau \quad (2.6)$$

$$\frac{dK_3}{dt} = (K_2 - K_3)/\tau \quad (2.7)$$

…..

$$\frac{dK_n}{dt} = (K_{n-1} - K_n)/\tau \quad (2.8)$$

$$K = \frac{K_{max} \cdot FU}{EC_{50} + FU} \quad (2.9)$$

C, K_{max}, EC_{50}, C_{SS}, 5-FU and K are as defined above. The rate function of 5-FU-induced cell killing (K_n) is related to K via a series of transit compartments (Lobo and Balthasar 2002). τ refers to the mean transit time in each compartment (Simeoni et al. 2004). This transit compartment model is useful for modeling the pharmacological effect of compounds that may be mediated by time-dependent transduction, and when there is a time lag in the final drug response (Sun and Jusko 1998). It can be particularly useful for modeling the cell kill effect of chemotherapeutic agents, since chemotherapeutic agents exert their effects through a complex mechanism of action, and in many cases there is a time delay in the observed effect after the administration of the agents (Lobo and Balthasar 2002). One advantage of the transit compartment model is that a mechanistic knowledge about each step is not required to construct the model. The model contains a minimal number of drug (E_{max} and EC_{50}) and system

parameters (τ) that may be applied to data and may provide a simple structure on which future knowledge of specific processes may be integrated (Mager et al. 2003).

3) Dual transit compartment model

$$\frac{dC}{dt} = k_g \cdot C \cdot (1 - C / C_{SS}) - K_n \cdot C - L_n \cdot C \quad (2.10)$$

$$\frac{dK_1}{dt} = (K - K_1) / \tau_1 \quad (2.11)$$

$$\frac{dL_1}{dt} = (L - L_1) / \tau_2 \quad (2.12)$$

$$\frac{dK_2}{dt} = (K_1 - K_2) / \tau_1 \quad (2.13)$$

$$\frac{dL_2}{dt} = (L_1 - L_2) / \tau_2 \quad (2.14)$$

…..

$$\frac{dK_n}{dt} = (K_{n-1} - K_n) / \tau_1 \quad (2.15)$$

$$\frac{dL_n}{dt} = (L_{n-1} - L_n) / \tau_2 \quad (2.16)$$

$$K = \frac{K_{max1} \cdot FU}{EC_{501} + FU} \quad (2.17)$$

$$L = \frac{K_{max2} \cdot FU}{EC_{502} + FU} \quad (2.18)$$

This is a modification of the transit compartment model. This model assumes that there are two independent mechanisms of action of the drug, and each mechanism of action is modeled by two separate sets of transit compartment models (K and L). The parameters used in the three PD models were determined by fitting the simulated growth curve to the growth curve of colon cancer cell line (HCT-116) under the influence of various concentrations of 5-FU. The experimental data was taken from the study by Yoshikawa (Yoshikawa et al. 2001). The lsqnonlin routine in the optimization toolbox of Matlab software was used to find the optimal parameter sets,

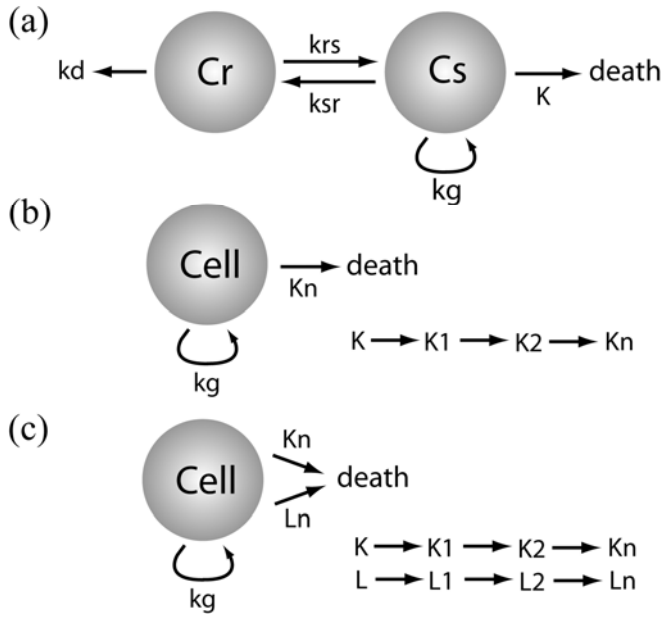

Figure 2.3 Pharmacodynamic models to simulate the growth of tumor cells

(a) Cell cycle phase specific model. Cell population is divided into resistant and sensitive groups. Cell death occurs through K, which is a function of drug concentration (b) Transit compartment model where cell death is mediated by a series of transit compartments defined by a function of drug concentration (c) Dual transit compartment where two cell death pathways exist.

Table 2.4 Parameters for the pharmacodynamic models

Cell cycle specific model	
C_{ss} (unitless)	90
K_g (1/hr)	0.1
K_{sr} (1/hr)	0.1
k_{rs} (1/hr)	0.1
K_{max} (1/hr)	0.119
EC_{50} (μM)	0.153
Transit compartment model	
K_g (1/hr)	0.0597
C_{ss} (unitless)	125
K_{max} (1/hr)	0.0985
EC_{50} (μM)	0.329
τ (hr)	2.97
Dual transit compartment model	
K_g (1/hr)	0.07
C_{ss} (unitless)	120
K_{max1} (1/hr)	0.0602
EC_{501} (μM)	0.0074
τ_1 (hr)	20.1
K_{max2} (1/hr)	0.142
EC_{502} (μM)	2.81
τ_2 (hr)	2.59

which solves a nonlinear least-square problem by minimizing user-defined function. We found the optimal parameter set by minimizing the difference between the model solution and the experimental data. The optimized parameters for the three models are listed in table 2.4.

The PBPK model and PD model were then combined, by using the concentration profiles of 5-FU in the tumor compartment from the PBPK model as the input values for 5-FU concentration in the PD model. The combined model can model dynamically the tumor response to the drug, since the drug concentration changes as a time dependent variable, and the growth of tumor will change depending on the drug concentration it is exposed to. It was assumed that the transport of the drugs is not limiting, based on the study that 5-fluorouracil uses a facilitated transport mechanism and achieves a rapid equilibration across the cell membrane (Wohlhueter et al. 1980). The resulting growth kinetics of tumor was compared with the experimental result by Rustum, in which the tumor cells were inoculated into rats and the rats were treated with either Tegafur or UFT for a period of time (Rustum 1997). For optimization of parameters, the lsqnonlin routine in the Matlab software was used (Table 2.5).

2.3 Results

2.3.1 Construction of PK-PD model

The result of parameter fitting for the PBPK model is shown in Figure 2.4 and 2.5. The experimental results shown in the figures for comparison were taken from Kawaguchi et al. (Kawaguchi et al. 1980). In general, the PBPK model made a reasonably good fit to the experimental data in all organs. The model was able to make accurate predictions for Tegafur concentration profiles in all organs. It should be noted that the result shown in Figure 2.5(b) was not used for curve fitting. We used this

Table 2.5 Parameters for PD model for tumor growth in a rat

K_g (1/hr)	0.012
C_{ss} (mg)	14000
K_{max1} (1/hr)	0.0075
EC_{501} (nmol/ml)	3.8
t_1 (hr)	20
K_{max2} (1/hr)	0.65
EC_{502} (nmol/ml)	70
t_2 (hr)	2.59

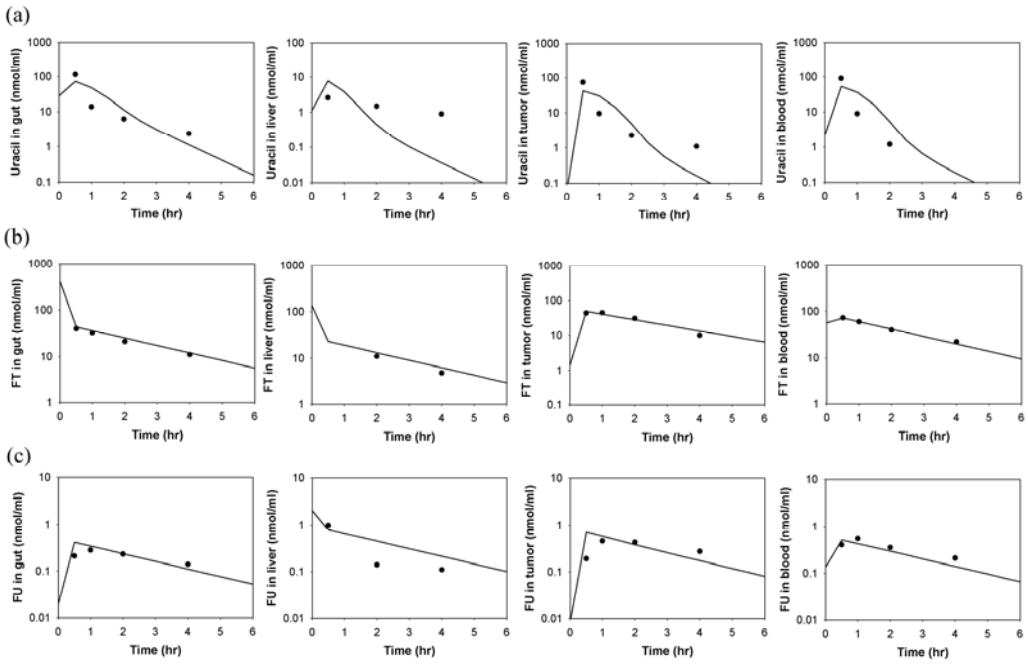

Figure 2.4 PK profiles after Tegafur or uracil administration

(a) Simulated and experimental concentration profiles of uracil after administration of uracil (33.6 mg/kg) (b) Tegafur after administration of Tegafur (15 mg/kg) (c) 5-FU after administration of Tegafur (15 mg/kg). Lines are the simulated profiles and dots are experimental data taken from literature (Kawaguchi, Nagayama et al. 1980).

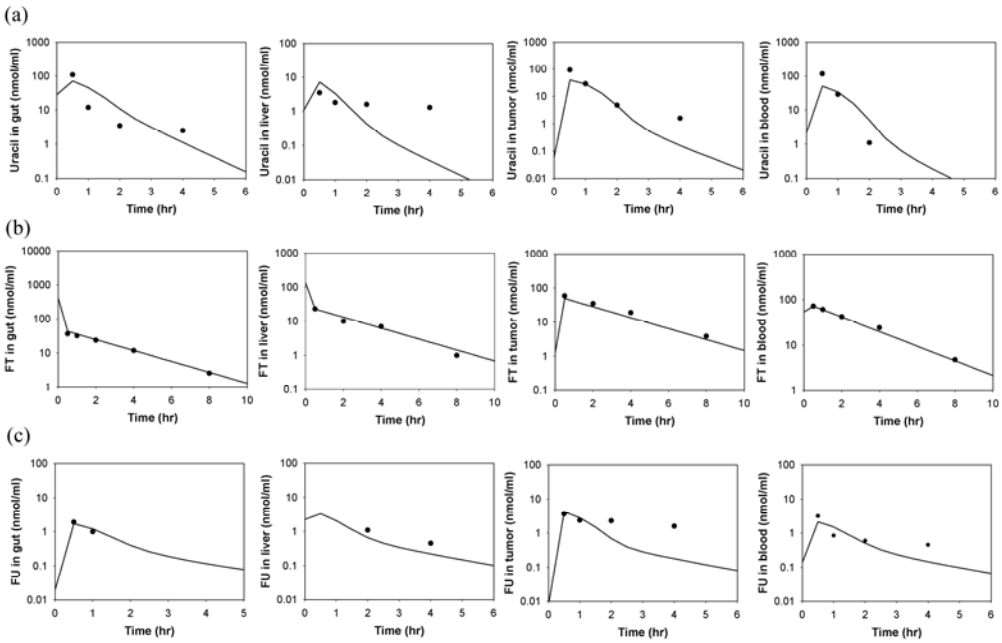

Figure 2.5 PK profiles after UFT administration

(a) Uracil (b) Tegafur and (c) 5-FU after UFT administration (uracil 33.6 mg/kg and Tegafur 15 mg/kg). Lines are simulated profiles and dots are experimental data taken from literature (Kawaguchi, Nagayama et al. 1980)

independent set of data to test the ability of the model to predict the Tegafur concentration profiles, and the result in Figure 2.5(b) shows that the constructed model is able to make predictions for Tegafur consistent with data. The predictions for uracil and 5-FU were fairly accurate, except the uracil concentration in the liver and 5-FU concentration in the tumor were predicted to have faster elimination than the observed pharmacokinetics, indicating possible binding events of the drug which were not included in our model. The observed uracil concentration in the liver was distinctively lower than the uracil concentration in the other organs, and if perfusion-limitation assumption was used, the partition coefficient of uracil in the liver would have to be reduced significantly to match the experimental data. Thus instead of using the partition coefficient approach, we assumed that there was limitation in the transport of the drug and separated the liver compartment into vascular space and tissue space. After fitting the transport coefficients across the vascular space and the tissue space, the uracil concentration profile in the liver matched the experimental data better.

Three different pharmacodynamic (PD) models of tumor cells were tested. Figure 2.6 shows the simulation of the three models, with the measured response of tumor cells (HCT-116) treated with five different doses of 5-FU (Yoshikawa et al. 2001). The phase-specific model in Figure 2.6(a) shows that it predicts the growth of untreated cancer cells fairly accurately. It also predicts the growth inhibition effect at early periods, but it is not able to predict the cell death at later times (after 80 hour). The transit compartment model in Figure 2.6(b) predicts the longer term cell death better. However, the prediction by the transit compartment model tends to become less accurate for lower drug concentrations and longer incubation times. Figure 2.6(c) shows the simulation result of dual transit compartment model, and the result shows that this model is able to predict the growth kinetics of tumor cells more accurately for all concentration and time ranges than the other models.

The PBPK model and the dual transit PD model were combined to predict the dynamics of tumor growth, which was compared with experimental results from literature (Rustum 1997). Since the previously developed PD model simulates the growth of tumor cells *in vitro*, the growth pattern in the *in vivo* situation can be expected to be different. Therefore we tested the model while maintaining the structure, but allowing the parameters to be re-adjusted. The pharmacokinetic profiles of the drugs were obtained using the PBPK model using the same doses used in the paper, and the simulated concentration profiles were used in the pharmacodynamic model to predict the tumor growth. The result in Figure 2.7 shows that the combined PK-PD model was able to make good predictions for three different dosing conditions, which are control (no treatment), Tegafur 150mg/kg/day and UFT 60mg/kg/day for 26 days. In case of Tegafur treatment, the model does not predict the re-growth of tumor after 12 days which may be the result of tumor developing resistance to the treatment.

2.3.2 Optimization of Dosing Regimens

We used the PK-PD model to examine various UFT dosing strategies. First the effect of the ratio of uracil and Tegafur was tested. To compare the efficacy and the toxicity of the drugs, the cell growth in the tumor was related to the efficacy of the drug and the cell growth in the blood was related to the toxic effect of systemic drug exposure to the body. The same model was used to simulate the growth of cells in the tumor and the blood compartment. Figure 2.8 show that the increase in the ratio of uracil and Tegafur results in higher 5-FU concentration and a slower cell growth in both the tumor and the blood compartment. A ratio that is too low will result in almost no toxic effect, but also no appreciable tumor reduction, whereas a high ratio will result in almost complete removal of tumor but a great amount of systemic toxicity.

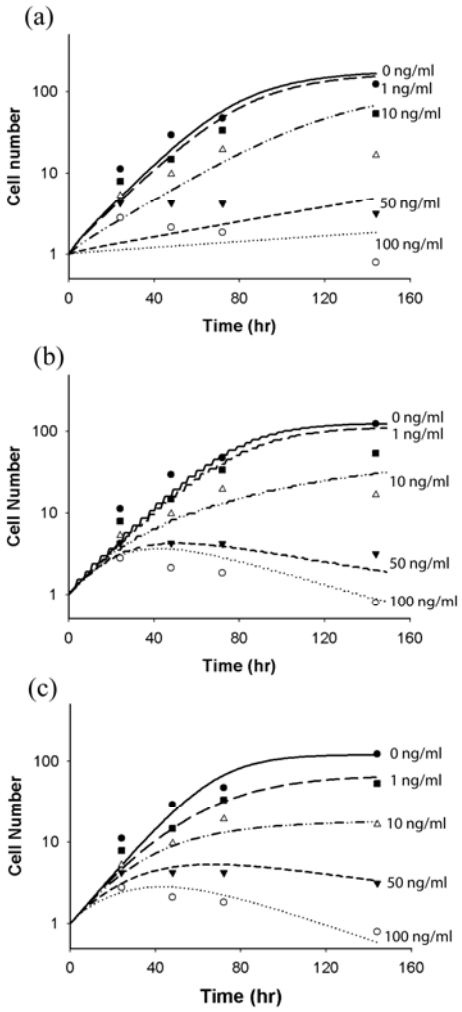

Figure 2.6 Comparison of PD model simulation with experimental result

(a) Phase-specific model (b) transit compartment model (c) dual-transit compartment model. Dots are experimental data from literature (Yoshikawa, Kusunoki et al. 2001) and lines are simulation results.

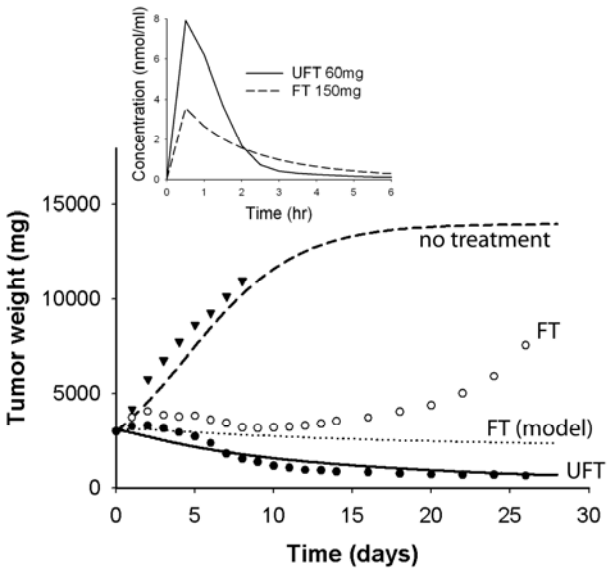

Figure 2.7 PK-PD model simulation for tumor growth in a rat

The rat was treated with UFT 60 mg/kg or FT 150 mg/kg. Dots are experimental results from literature (Rustum 1997) and lines are simulation results. Shown in inset is the pharmacokinetic profiles of 5-FU in tumor for the two dosing conditions.

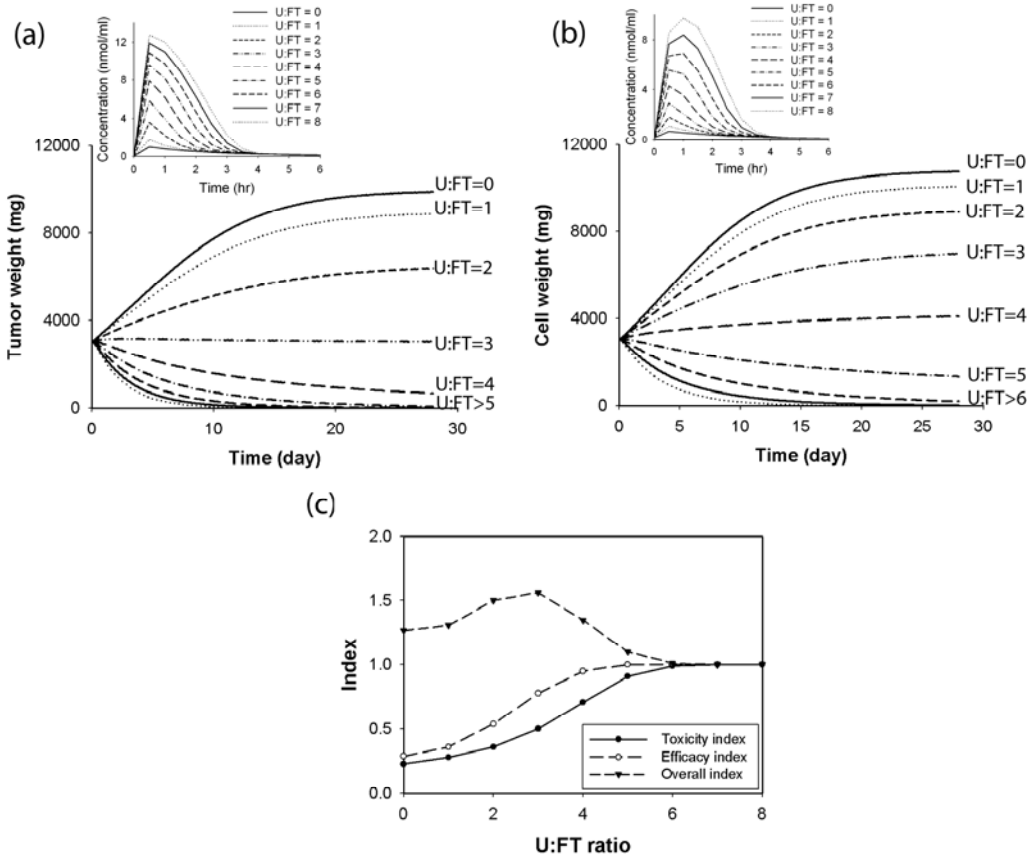

Figure 2.8 Simulation of cell growth with various combination ratios

Simulated cell growth in (a) tumor and (b) blood compartment for various U:FT ratios. 5-FU concentration profiles in each compartment are shown in smaller boxes. (c) Toxicity and efficacy index of UFT for various U:FT combination ratios.

In the tumor compartment, 5-FU concentration increases the most between ratios of two to four, whereas in the blood compartment a steeper increase occurs after the ratio of four. It is shown more clearly in Figure 2.8(c), with the predicted efficacy and the predicted toxicity of the drug. The efficacy index of the drug was calculated as the relative tumor reduction (zero being no reduction and one being complete elimination of tumor, compared to the tumor growth in the case of no treatment), and the toxicity index was calculated as ratio of cell death in the blood compartment (zero being no toxicity and one being complete cell death in the blood compartment compared to the cell growth in the case of no treatment). The overall index was calculated by dividing the efficacy index by toxicity index, thus a higher overall index means a higher tumor reduction with lower blood toxicity. The plot of overall index shows that the optimal combination ratio is achieved between combination rations of two and four, where the efficacy is the highest relative to the toxic effect. This optimal ratio of uracil to Tegafur that was predicted from our mathematical model agrees with the reported optimal combination ratio in experiment reported by Fujii (Fujii et al. 1979).

The effect of dihydropyrimidine dehydrogenase (DPD) activity was tested by varying the value of V_m for dihydropyrimidine dehydrogenase (DPD) enzyme, shown in Figure 2.9. Since DPD enzyme catalyzes degradation of 5-FU, it is predicted that a higher DPD activity will result in a low 5-FU concentration. With a high DPD activity, there was almost no tumor remission, but relatively rapid cell proliferation in the blood compartment. On the other hand, with a low DPD enzyme activity, there was a complete tumor remission, but also a complete cell death in the blood. Based on the simulation a high DPD activity will result in a weak tumor response while toxic side effects will also be negligible. A low DPD activity will result in complete remission of tumor, although a severe side effect is likely to make the dosing unacceptable.

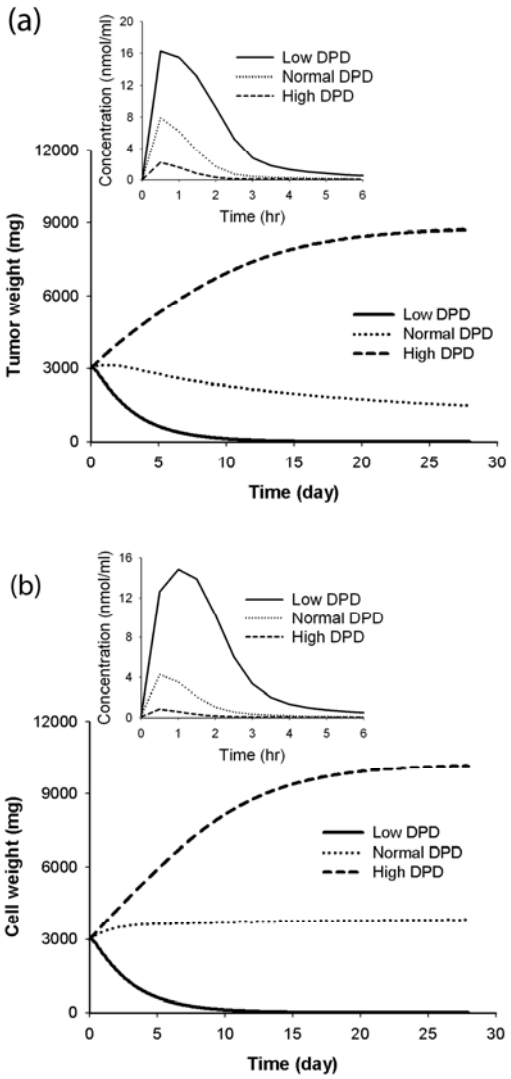

Figure 2.9 Simulation of cell growth for various DPD activities

Cell growth in (a) tumor and (b) blood compartment for various DPD activities, with 5-FU concentration profiles shown in inset. Low DPD activity results in increased 5-FU concentration, resulting in rapid cell death in both tumor and blood. High DPD activity results in reduced 5-FU concentration with rapid cell proliferation.

Due to the dramatic effect of changes in the DPD activity on the pharmacokinetic profiles of 5-FU, the dosage of UFT which would be effective at normal DPD activity becomes impractical with abnormal DPD levels. The main criterion for adjusting the dosage was the 5-FU level in the blood, since 5-FU in the blood will determine the systemic drug exposure. In the study by Rustum, the maximum tolerated dose (MTD) for a rat was 60mg/kg/day of UFT, three times daily. From our PBPK model with normal DPD activity, this dosing schedule resulted in the AUC of 470 nmol·min/ml in the blood. In case of abnormal DPD activity, the dosage was adjusted so that it would result in the same 5-FU AUC value. In case of low DPD activity, the original dose had to be reduced by 56%, whereas in case of high DPD activity, it was increased by 86%. In case of low DPD activity, changing the drug combination ratio did not have noticeable effect on the pharmacodynamic profile, whereas in case of high DPD activity, about 50% increase in the overall index of the drug resulted from changing the ratio of uracil to Tegafur (Figure 2.10). Therefore in case of a rat with a low DPD activity, even after reducing the dose, not much benefit is expected from combining uracil with Tegafur.

In Figure 2.11, we tested the pharmacokinetic/pharmacodynamic profile of two different dosing strategies, pharmacokinetic modulating chemotherapy (PMC) and 5-FU continuous infusion. PMC is a combination of 5-FU continuous infusion with periodic oral administration of UFT, which has been shown to enhance the response significantly compared to 5-FU infusion (Kusunoki et al. 2000). The total drug dose was kept same at 40mg/kg/day. The model simulation showed that continuous infusion of 5-FU results in a low concentration of 5-FU in the tumor, whereas UFT administration causes a spike in the 5-FU concentration. Consequently, the tumor growth is significantly reduced with PMC, whereas 5-FU infusion alone has a much weaker anti-tumor activity than PMC.

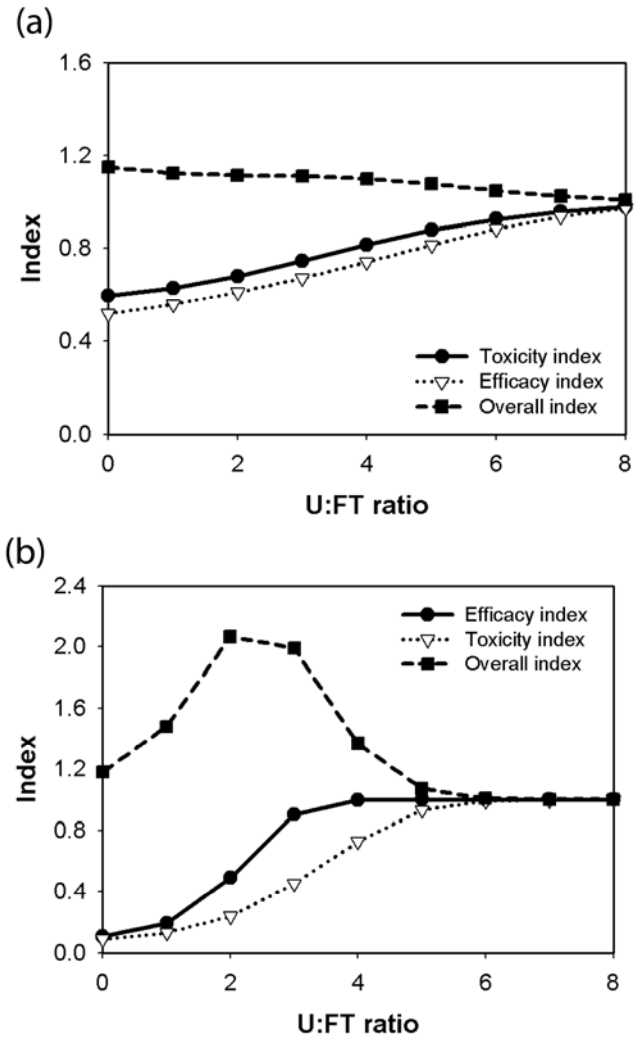

Figure 2.10 Effect of U:FT ratio on efficacy and toxicity of UFT

(a) low DPD activity, (b) high DPD activity. In case of low DPD activity changing U:FT combination ratio does not result in enhancement of efficacy or toxicity profiles of the drug, whereas in case of high DPD activity, U:FT combination ratio of 2 to 4 gives the highest efficacy relative to the toxic effect.

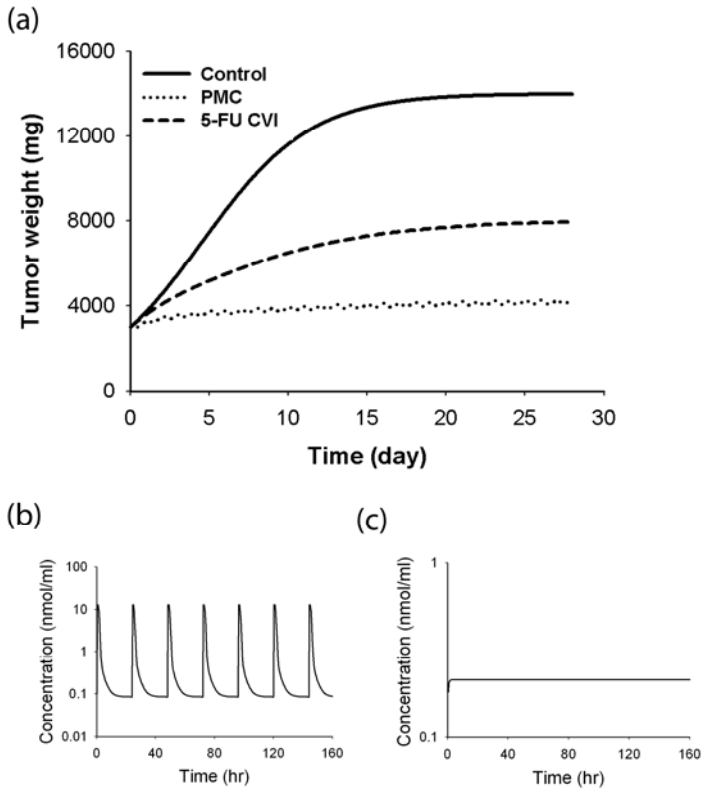

Figure 2.11 Simulation of pharmacokinetic-modulating chemotherapy (PMC)

(a) Predicted tumor growth in response to two different dosing regimens, pharmacokinetic modulating chemotherapy (PMC), and continuous intravenous infusion of 5-FU (5-FU CVI). 5-FU concentration profile in tumor after (b) PMC (c) 5-FU CVI. Total dosage of 5-FU was same at 40 mg/kg/day. Combination of oral UFT and continuous venous infusion (CVI) of 5-FU resulted in enhanced pharmacokinetic profile and tumor growth inhibition than the same dose of 5-FU CVI alone.

2.4 Discussion

2.4.1 The construction of PBPK model and PD model

The PBPK model was fitted to the concentration profiles of three compounds in four different organs for two different dosing conditions. In total, 24 concentration profiles were used for fitting the PBPK model. Simulation results of the developed PBPK model showed a good fit to the experimental data from literature (Kawaguchi et al. 1980), with exception of 5-FU concentration in the tumor and uracil concentration in the liver. In both cases the observed pharmacokinetics showed a slower clearance than predicted, which suggests possible binding mechanisms not included in the model. The most serious deviation occurred in case of 5-FU in the tumor after UFT administration, which implies that the simple competitive inhibition mechanism assumed in the model may not be sufficient to fully describe the interaction between 5-FU, uracil and DPD enzyme. For example, it is possible that there may be different active sites on DPD enzyme for 5-FU and uracil, and the inhibition kinetics for 5-FU and uracil may be more complex. Another possibility is that in addition to the degradation by DPD, they may also be competing for the transport into cells, since they are known to share the same facilitated transport mechanism (Wohlhueter et al. 1980).

Three different models for tumor cell growth were tested and compared with experimental data for the colon cancer cell line (HCT-116) treated with various concentrations of 5-FU (Figure 2.6) (Yoshikawa et al. 2001). A cell cycle specific model is often used to model the growth of tumor cells treated with chemotherapeutic agents, since many chemotherapeutic drugs are known to be cell cycle specific (Mager et al. 2003). 5-FU is also known to be G1/S phase-specific (Yoshikawa et al. 2001), thus it is reasonable to divide the cell population into a sensitive and a resistant group.

A transit compartment model is also often used to model the growth of tumor cells under the influence of chemotherapeutic agent, where transit compartments are assumed to mimic the time delay in the process of cell killing (Sun and Jusko 1998; Lobo and Balthasar 2002).

We also tested the modified form of the transit compartment model, with two different groups of transit compartments. The idea of having two different groups of compartments arose from the fact that there is more than one mechanism of action of 5-FU on tumors. Currently there are three known mechanisms of action (DNA misincorporation by FdUTP, RNA misincorporation by FUTP and TS inhibition by FdUMP) (Longley et al. 2003). Since TS is an enzyme responsible for de novo synthesis of thymidylate, the cause of cytotoxicity by 5-FU can be roughly divided into either DNA based mechanism or RNA based mechanism. There is evidence that the primary mechanism of action depends on the concentration range of 5-FU; high 5-FU concentration is known to cause RNA disruption, whereas low 5-FU concentration causes DNA disruption (Spiegelman et al. 1980; Parker and Cheng 1990; Yoshikawa et al. 2001). By incorporating two separate sets of transit compartments in the model, two separate mechanisms of action can be captured.

The simulation result of the three different PD models showed that the dual transit compartment model showed the best fit to the experimental data. It is interesting to note that the optimized KC50 and τ values for the two sets of transit compartments differ from each other. KC50 and τ for the first set of transit compartments are 0.0074μM and 20.1 hours and KC50 and τ for the second is 2.81μM and 2.59 hours, respectively. Since DNA inhibition is known to be dominant at low concentration of 5-FU (Parker and Cheng 1990), the first set of transit compartments may represent the DNA inhibition mechanism. RNA inhibition is known to be dominant at high concentration of 5-FU (Spiegelman et al. 1980), therefore the second

set may represent the RNA inhibition mechanism. It is also interesting to note the difference in the τ values. τ represents a theoretical residence time which the cells stay in each transit compartment during the progression to the cell death, therefore low τ value represents an rapid response, whereas high τ value means slower response of tumor cells to the drug. In a study by Petak, colon carcinoma cell lines treated with 5-FU went through either acute apoptosis or delayed apoptosis depending on their genotypes (Petak et al. 2000), also suggesting dual mechanism of action. We believe that the dual transit compartment model can be an adequate model to describe this dual action of 5-FU on tumor cells. However, the parameters for the two pathways were obtained by fitting and they do not have molecular basis. Relating the transit compartments in our model with specific states in the molecular pathways was not straightforward since the exact molecular mechanisms that mediate further downstream events have not been fully elucidated (Longley et al. 2003). However, there have been continued research efforts to elucidate molecular mechanisms of 5-fluorouraicl toxicity (Takeda et al. 1999; Li et al. 2004; Chinery et al. 1997). As more information becomes available, specific molecular mechanisms could be integrated into the transit compartment model.

2.4.2 Finding Optimal UFT Combination Ratios for Various DPD Activities

In Figure 2.8, varying the combination ratio of uracil and Tegafur resulted in a significant change in the pharmacokinetic and pharmacodynamic profiles. Increasing uracil results in more inhibition of 5-FU degradation, improving the pharmacokinetic profile. In a study by Fujii, the optimal combination ratio was determined by comparing the tumor-to-blood ratio of 5-FU (Fujii et al. 1979). The rationale behind this approach was that the efficacy of the drug would be proportional to the 5-FU in

the tumor, and the systemic toxicity would be proportional to the 5-FU in the blood. Therefore, the ratio of uracil to Tegafur that gives the maximum value of the tumor-to-blood ratio of 5-FU would be the most ideal ratio. The molar ratio of 4 to 1 was determined to be the optimal ratio of uracil to Tegafur, giving the highest tumor to blood ratio of 5-FU. Our PK-PD simulation results were close to the experimental result since the ratio of the efficacy and the toxicity index reaches maximum at the ratio of uracil to Tegafur between two and four. Increasing the combination ratio beyond that point would result in a better efficacy, but too much toxicity. We believe that this agreement further validates our PBPK model, since the model parameters were optimized based on the study by Kawaguchi (Kawaguchi et al. 1980), which is a separate study from Fujii (Fujii et al. 1979). In figure 2.9, we assessed the effect of having different DPD activities. The importance of DPD enzyme in 5-FU related chemotherapy has been widely recognized (Wei et al. 1996; Ichikawa et al. 2003; Kornmann et al. 2003; van Kuilenburg 2004). DPD activity *in vitro* in tumor cells is strongly related to 5-FU sensitivity such that the lower the enzymatic activity, the greater the cytotoxicity (Ichikawa et al. 2003). *In vivo* DPD activity can also be related to the efficacy of 5-FU; It was demonstrated that a high DPD level was associated with 5-FU resistance (Kornmann et al. 2003), and Salonga et al. reported that a colorectal cancer patients with a low DPD activity responded better to 5-FU treatment than the patients with a high DPD activity (Salonga et al. 2000). The DPD level has also been associated with toxicity of 5-FU. There is ample evidence that a deficiency of DPD is associated with severe toxicity after 5-FU administration (van Kuilenburg 2004). Based on these findings, a pharmacokinetic-based test to prevent severe 5-FU toxicity has been proposed (Bocci et al. 2006). The individual variations in the DPD enzyme level is known to be quite common. According to a study on population characteristics of human DPD enzyme levels, 14% of the population would be at risk

of developing severe 5-FU related toxicity (Van Kuilenburg et al. 2002). In another study using 138 donor liver samples, DPD activity followed a normal Gaussian distribution, and the lowest DPD activity and the highest DPD activity showed about 20 fold difference (Lu et al. 1995). It has also been found that there is a circadian variation in the DPD activity (Lévi et al. 1992). Therefore, quantitative analysis of the pharmacokinetic profiles of 5-FU in patients with different DPD activities is crucial to optimizing and individualizing the dosing strategy of 5-FU related chemotherapy.

The PK-PD model predictions in Figure 2.9 agree with previous clinical findings. Low DPD activity caused unacceptable toxicity, whereas high DPD activity compromised the efficacy of the drugs. In addition, using the combined PK-PD model dosage was optimized in the cases of abnormal DPD level. In a clinical situation, the DPD enzyme level in a patient can be analyzed by measuring the DPD activity in tumor or liver tissue obtained from surgery. Measurement of DPD activity in peripheral blood mononuclear cells was suggested to circumvent the practical issue of obtaining biopsy samples (Lu et al. 1993). Advances in pharmacogenetics have also identified genetic mutations responsible for DPD deficiencies, allowing high-throughput screening of DPD activity in a patient (Park et al. 2003; van Kuilenburg 2004; Deeken et al. 2007). Combined with these methods, the PK-PD model may be a useful tool for the individual optimization of the dosing strategies of 5-FU based chemotherapy.

Pharmacokinetic modulating chemotherapy (PMC) has been developed as a strategy to maximize the anti-tumor effect of 5-FU based chemotherapy. Continuous infusion provides a baseline of low 5-FU concentration while periodic administration of UFT provides an increase in the 5-FU concentration. In a study by Fujii, PMC greatly enhanced the pharmacokinetic profile of 5-FU and anti-tumor effects without severe toxicities (Fujii et al. 1989). In a clinical trial involving 58 patients having

hepatic colorectal cancer, combination of 5-FU infusion with periodic UFT administration gave a dramatic improvement in 5-year survival rate (59% vs. 27%) and a decrease in hepatic recurrence (34.2 vs. 18.4 months) compared to administration of UFT alone (Kusunoki et al. 2000). Such an enhancement in the anti-tumor activity observed with combination of two different dosing regimens, although using the same drug, is attributed to a dual anti-tumor effect of 5-FU on cell cycle (Yoshikawa et al. 2001). In this study, where tumor cell lines were treated with various 5-FU concentrations, tumor cells showed different responses depending on the concentration. For example, G2 arrest was seen after 24-72 hour exposure to 10ng/ml of 5-FU, while G1 arrest was seen after 12-24 hour of exposure to 100ng/ml. These results suggest that 5-FU acts on the tumor cells via different pathways depending on the dose, and PMC exploits the dual pathways of 5-FU by exposing the tumor to different concentration ranges in a time dependent manner. A PK-PD model is an ideal tool to test such a hypothesis. Figure 2.11 shows that a significant enhancement in the pharmacokinetics of 5-FU can be achieved with PMC, resulting in enhanced anti-tumor activity compared to 5-FU continuous infusion. It clearly demonstrates that even with the same total drug dose, the pharmacological effect of the drug can vary considerably simply by varying the administration strategy.

Extrapolation of animal model analysis to human model is not always straightforward and the verification of animal model does not warrant the successful implementation of human model (Aarons 2005). However, during a drug development or risk assessment process, a rat model is often considered to be a surrogate species for a human model, because it is the most commonly used animal species for ADME (absorption, distribution, metabolism and excretion) characterization (Theil et al. 2003). For extrapolation of animal to human, an allometric scaling have often been (Luttringer et al. 2003), and a corollary approach was used in rat to human

extrapolation by comparing the pharmacokinetics of structurally similar molecules (Williams et al. 1996). While incorporation of human physiological and anatomical data would be relatively simple, metabolism and disposition of the drugs may differ between different species. However, now it is well established that *in vitro* metabolism data obtained from microsomes or hepatocytes can be useful for the prediction of *in vivo* clearance of drugs with appropriate use of mathematical models and scaling factors to account for *in vitro* - *in vivo* differences and the physiology of the liver (Theil et al. 2003). We believe that the PK-PD modeling approach we used in this study for a rat provides a valid mathematical framework for developing a human model as well.

2.5 Conclusion

We developed a combined PK-PD model that describes the response of tumor in a rat to the administration of UFT. A PBPK model and a PD model were developed separately and fitted to experimental data in literature, and a combined PK-PD model was used to describe tumor progression in a rat. It was shown that this mathematical model can be used to test various dosing strategies and simulate the effects of variations in the enzyme levels. Furthermore, the model was used to optimize a dosing strategy to exploit the dual toxicity mechanism of 5-FU. This model should be useful in an effort to individualize cancer chemotherapy on a patient by patient basis. In addition, with the combination of a pharmacokinetic and a pharmacodynamic model, it can be useful in gaining more insight into the mechanism of the cytotoxicity of 5-FU.

REFERENCES

Aarons, L. (2005). "Physiologically based pharmacokinetic modelling: a sound mechanistic basis is needed." Br J Clin Pharmacol 60(6): 581-3.

Adams, C. P. and V. V. Brantner (2006). "Estimating the cost of new drug development: is it really 802 million dollars?" Health Aff (Millwood) 25(2): 420-8.

Adjei, A. A. (1999). "A review of the pharmacology and clinical activity of new chemotherapy agents for the treatment of colorectal cancer." Br J Clin Pharmacol 48(3): 265-77.

Bocci, G., et al. (2006). "A pharmacokinetic-based test to prevent severe 5-fluorouracil toxicity." Clin Pharmacol Ther 80(4): 384-95.

Borner, M. M., et al. (2002). "Patient preference and pharmacokinetics of oral modulated UFT versus intravenous fluorouracil and leucovorin: a randomised crossover trial in advanced colorectal cancer." Eur J Cancer 38(3): 349-58.

Chinery, R., et al. (1997). "Antioxidants enhance the cytotoxicity of chemotherapeutic agents in colorectal cancer: a p53-independent induction of p21WAF1/CIP1 via C/EBPbeta." Nat Med 3(11): 1233-41.

Davies, B. and T. Morris (1993). "Physiological parameters in laboratory animals and humans." Pharm Res 10(7): 1093-5.

de Bono, J. S. and C. J. Twelves (2001). "The oral fluorinated pyrimidines." Invest New Drugs 19(1): 41-59.

Deeken, J. F., et al. (2007). "Toward individualized treatment: prediction of anticancer drug disposition and toxicity with pharmacogenetics." Anticancer Drugs 18(2): 111-26.

Farris, F. F., et al. (1985). "Physiological model for the pharmacokinetics of cis-dichlorodiammineplatinum (II) (DDP) in the tumored rat." J Pharmacokinet Biopharm 13(1): 13-39.

Fujii, S., et al. (1989). "Pharmacokinetic modulation of plasma 5-fluorouracil concentrations to potentiate the antitumor activity of continuous venous infusion of 5-fluorouracil." Jpn J Cancer Res 80(6): 509-12.

Fujii, S., et al. (1979). "Effect of coadministration of uracil or cytosine on the anti-tumor activity of clinical doses of 1-(2-tetrahydrofuryl)-5-fluorouracil and level of 5-fluorouracil in rodents." Gann 70(2): 209-14.

Gill, S., et al. (2003). "Review article: colorectal cancer chemotherapy." Aliment Pharmacol Ther 18(7): 683-92.

Goyle, S. and A. Maraveyas (2005). "Chemotherapy for colorectal cancer." Dig Surg 22(6): 401-14.

Hahn, R. G., et al. (1975). "A double-blind comparison of intensive course 5-flourouracil by oral vs. intravenous route in the treatment of colorectal carcinoma." Cancer 35(4): 1031-5.

Heggie, G. D., et al. (1987). "Clinical pharmacokinetics of 5-fluorouracil and its metabolites in plasma, urine, and bile." Cancer Res 47(8): 2203-6.

Heidelberger, C., et al. (1957). "Fluorinated pyrimidines, a new class of tumour-inhibitory compounds." Nature 179(4561): 663-6.

Ichikawa, W., et al. (2003). "Combination of dihydropyrimidine dehydrogenase and thymidylate synthase gene expressions in primary tumors as predictive parameters for the efficacy of fluoropyrimidine-based chemotherapy for metastatic colorectal cancer." Clin Cancer Res 9(2): 786-91.

Ikenaka, K., et al. (1979). "Effect of uracil on metabolism of 5-fluorouracil in vitro." Gann 70(3): 353-9.

Jacobs, D. A. H. and Institute of Mathematics and Its Applications. (1977). The state of the art in numerical analysis : proceedings of the Conference on the State of the Art in Numerical Analysis held at the University of York, April 12th-15th, 1976. London ; New York, Academic Press.

Jain, R. K. (1988). "Determinants of tumor blood flow: a review." Cancer Res 48(10): 2641-58.

Kajita, J., et al. (2003). "The contribution of cytochrome P450 to the metabolism of tegafur in human liver." Drug Metab Pharmacokinet 18(5): 303-9.

Kawaguchi, Y., et al. (1980). "Studies on the metabolism of 1-(2-tetrahydrofuryl)-5-fluorouracil and uracil co-administered orally to tumor-bearing rats." Gann 71(6): 889-99.

Kelder, W., et al. (2006). "Effects of 5-fluorouracil adjuvant treatment of colon cancer." Expert Rev Anticancer Ther 6(5): 785-94.

Komatsu, T., et al. (2000). "Roles of cytochromes P450 1A2, 2A6, and 2C8 in 5-fluorouracil formation from tegafur, an anticancer prodrug, in human liver microsomes." Drug Metab Dispos 28(12): 1457-63.

Kornmann, M., et al. (2003). "Thymidylate synthase and dihydropyrimidine dehydrogenase mRNA expression levels: predictors for survival in colorectal cancer patients receiving adjuvant 5-fluorouracil." Clin Cancer Res 9(11): 4116-24.

Kusunoki, M., et al. (2000). "Results of pharmacokinetic modulating chemotherapy in combination with hepatic arterial 5-fluorouracil infusion and oral UFT after resection of hepatic colorectal metastases." Cancer 89(6): 1228-35.

Lévi, F., et al. (1992). "A chronopharmacologic phase II clinical trial with 5-fluorouracil, folinic acid, and oxaliplatin using an ambulatory multichannel programmable pump. High antitumor effectiveness against metastatic colorectal cancer." Cancer 69(4): 893-900.

Li, M. H., et al. (2004). "Effect of 5-fluorouracil on G1 phase cell cycle regulation in oral cancer cell lines." Oral Oncol 40(1): 63-70.

Lobo, E. D. and J. P. Balthasar (2002). "Pharmacodynamic modeling of chemotherapeutic effects: application of a transit compartment model to characterize methotrexate effects in vitro." AAPS PharmSci 4(4): E42.

Longley, D. B., et al. (2003). "5-fluorouracil: mechanisms of action and clinical strategies." Nat Rev Cancer 3(5): 330-8.

Lu, Z., et al. (1993). "Dihydropyrimidine dehydrogenase activity in human peripheral blood mononuclear cells and liver: population characteristics, newly identified deficient patients, and clinical implication in 5-fluorouracil chemotherapy." Cancer Res 53(22): 5433-8.

Lu, Z., et al. (1995). "Population characteristics of hepatic dihydropyrimidine dehydrogenase activity, a key metabolic enzyme in 5-fluorouracil chemotherapy." Clin Pharmacol Ther 58(5): 512-22.

Luttringer, O., et al. (2003). "Physiologically based pharmacokinetic (PBPK) modeling of disposition of epiroprim in humans." J Pharm Sci 92(10): 1990-2007.

Mager, D. E., et al. (2003). "Diversity of mechanism-based pharmacodynamic models." Drug Metab Dispos 31(5): 510-8.

Malet-Martino, M. and R. Martino (2002). "Clinical studies of three oral prodrugs of 5-fluorouracil (capecitabine, UFT, S-1): a review." Oncologist 7(4): 288-323.

Park, D. J., et al. (2003). "Tailoring chemotherapy in advanced colorectal cancer." Curr Opin Pharmacol 3(4): 378-85.

Parker, W. B. and Y. C. Cheng (1990). "Metabolism and mechanism of action of 5-fluorouracil." Pharmacol Ther 48(3): 381-95.

Pasetto, L. M., et al. (2006). "Stable disease in advanced colorectal cancer: therapeutic implications." Anticancer Res 26(1B): 511-22.

Petak, I., et al. (2000). "p53 dependence of Fas induction and acute apoptosis in response to 5-fluorouracil-leucovorin in human colon carcinoma cell lines." Clin Cancer Res 6(11): 4432-41.

Pinedo, H. M. and G. F. Peters (1988). "Fluorouracil: biochemistry and pharmacology." J Clin Oncol 6(10): 1653-64.

Ploylearmsaeng, S. A., et al. (2006). "How may anticancer chemotherapy with fluorouracil be individualised?" Clin Pharmacokinet 45(6): 567-92.

Poulin, P. and F. P. Theil (2002). "Prediction of pharmacokinetics prior to in vivo studies. 1. Mechanism-based prediction of volume of distribution." J Pharm Sci 91(1): 129-56.

Quick, D. J. and M. L. Shuler (1999). "Use of in vitro data for construction of a physiologically based pharmacokinetic model for naphthalene in rats and mice to probe species differences." Biotechnol Prog 15(3): 540-55.

Relling, M. V. and T. Dervieux (2001). "Pharmacogenetics and cancer therapy." Nat Rev Cancer 1(2): 99-108.

Rustum, Y. M. (1997). "Mechanism-based improvement in the therapeutic selectivity of 5-FU prodrug alone and under conditions of metabolic modulation." Oncology 54 Suppl 1: 7-11.

Rutman, R. J., et al. (1954). "The catabolism of uracil in vivo and in vitro." J Biol Chem 210(1): 321-9.

Salonga, D., et al. (2000). "Colorectal tumors responding to 5-fluorouracil have low gene expression levels of dihydropyrimidine dehydrogenase, thymidylate synthase, and thymidine phosphorylase." Clin Cancer Res 6(4): 1322-7.

Simeoni, M., et al. (2004). "Predictive pharmacokinetic-pharmacodynamic modeling of tumor growth kinetics in xenograft models after administration of anticancer agents." Cancer Res 64(3): 1094-101.

Spiegelman, S., et al. (1980). "Improving the anti-tumor activity of 5-fluorouracil by increasing its incorporation into RNA via metabolic modulation." Proc Natl Acad Sci U S A 77(8): 4966-70.

Sun, Y. N. and W. J. Jusko (1998). "Transit compartments versus gamma distribution function to model signal transduction processes in pharmacodynamics." J Pharm Sci 87(6): 732-7.

Takeda, H., et al. (1999). "Effect of 5-fluorouracil on cell cycle regulatory proteins in human colon cancer cell line." Jpn J Cancer Res 90(6): 677-84.

Tanaka, F., et al. (2000). "The history, mechanism and clinical use of oral 5-fluorouracil derivative chemotherapeutic agents." Curr Pharm Biotechnol 1(2): 137-64.
Tatsumi, K., et al. (1987). "Inhibitory effects of pyrimidine, barbituric acid and pyridine derivatives on 5-fluorouracil degradation in rat liver extracts." Jpn J Cancer Res 78(7): 748-55.

Theil, F. P., et al. (2003). "Utility of physiologically based pharmacokinetic models to drug development and rational drug discovery candidate selection." Toxicol Lett 138(1-2): 29-49.

van Kuilenburg, A. B. (2004). "Dihydropyrimidine dehydrogenase and the efficacy and toxicity of 5-fluorouracil." Eur J Cancer 40(7): 939-50.

Van Kuilenburg, A. B., et al. (2002). "Increased risk of grade IV neutropenia after administration of 5-fluorouracil due to a dihydropyrimidine dehydrogenase deficiency: high prevalence of the IVS14+1g>a mutation." Int J Cancer 101(3): 253-8.

Vaupel, P., et al. (1989). "Blood flow, oxygen and nutrient supply, and metabolic microenvironment of human tumors: a review." Cancer Res 49(23): 6449-65.

Wei, X., et al. (1996). "Molecular basis of the human dihydropyrimidine dehydrogenase deficiency and 5-fluorouracil toxicity." J Clin Invest 98(3): 610-5.

Williams, R. J., et al. (1996). "Rat to human extrapolation of HCFC-123 kinetics deduced from halothane kinetics: a corollary approach to physiologically based pharmacokinetic modeling." Fundam Appl Toxicol 30(1): 55-66.

Wohlhueter, R. M., et al. (1980). "Facilitated transport of uracil and 5-fluorouracil, and permeation of orotic acid into cultured mammalian cells." J Cell Physiol 104(3): 309-19.

Yamazaki, H., et al. (2001). "Rat cytochrome p450 1A and 3A enzymes involved in bioactivation of tegafur to 5-fluorouracil and autoinduced by tegafur in liver microsomes." Drug Metab Dispos 29(6): 794-7.

Yoshikawa, R., et al. (2001). "Dual antitumor effects of 5-fluorouracil on the cell cycle in colorectal carcinoma cells: a novel target mechanism concept for pharmacokinetic modulating chemotherapy." Cancer Res 61(3): 1029-37.

CHAPTER 3

SILICON MICRO CELL CULTURE ANALOG (μCCA) WITH 3-D HYDROGEL CULTURES FOR ASSESSING METABOLISM-DEPENDENT CYTOTOXICITY OF ANTI-CANCER DRGS[2]

3.1 Introduction

During the preclinical phase of drug development process, evaluation of a New Chemical Entity (NCE) is typically performed using cell-based assays, which are readily adaptable to a high-throughput format. However, current *in vitro* cell-based assays have limitations due to the fact that only a single cell type is used in the assay, and multi-organ interactions cannot be observed. Also, current multi-well plate systems are static systems in which cells are incubated with medium containing test compounds as a bolus dose. The *in vivo* situation is much more complicated; after administration, drugs undergo a complex process of absorption, distribution, metabolism and elimination (ADME). Consequently, changes in pharmacokinetic, pharmacodynamic (PK/PD) profiles due to organ interactions *in vivo* may result in revelation of unpredicted toxicity or lack of efficacy that would otherwise not become apparent until later stages of drug development.

Another important limitation of current *in vitro* cell-based assay systems is that a 2-D monolayer culture of an established cell line is used, which may not replicate the physiological response in human tissue. For example, HepG2/C3A is a hepatoma cell line originated from human hepatocellular carcinoma, but lacks many liver specific functions. The issue of achieving authentic responses from cells can be

[2] This chapter has been modified from, Sung, J. H. and M. L. Shuler (2009). "A micro cell culture analog (microCCA) with 3-D hydrogel culture of multiple cell lines to assess metabolism-dependent cytotoxicity of anti-cancer drugs." Lab Chip 9(10): 1385-94, with permission of Royal Society of Chemistry (http://www.rsc.org/publishing/journals/LC/article.asp?doi=b901377f).

partially addressed with a 3-D hydrogel cell culture. In their natural environment, extracellular matrix (ECM) and cell-to-cell interactions play a significant role in maintaining the physiological function of cells *in vivo* through complex chemical and mechanical signaling mechanisms (Daley et al. 2008). Culturing cells *in vitro* in a 3-D hydrogel has been shown to help cells retain their native tissue-specific functions and differentiated state (Cushing and Anseth 2007). In particular, it has been noted that the combination of a microfluidic system with a 3-D hydrogel cell culture can improve the tissue specific functions of cultured cells, since it can easily mimic the native 3-D tissue environment with blood flow supplying oxygen and nutrients. The potential significance of 3-D hydrogel cell cultures in microfluidic systems has gained increasing attention recently (Choi et al. 2007; Kim et al. 2007; Wong et al. 2008).

In this chapter we report incorporation of 3-D hydrogel cell cultures of multiple cell types into a μCCA for testing drugs for colon cancer. A μCCA was designed based on a human PBPK model, and 3-D hydrogel cultures of colon cancer, liver, and myeloblasts were incorporated into the μCCA using Matrigel and alginate as hydrogel matrix for cell encapsulation. Matrigel is a basement membrane matrix which is a complex mixture of various proteins including laminin and collagen (Brown et al. 2007; Wong et al. 2008). Alginate is a copolymer of mannuronate and guluronate, which forms a gel in the presence of multivalent cations (Peirone et al. 1998). Both hydrogels are widely used for cell encapsulation. The effect of an anti-cancer drug on each cell line was tested using the μCCA to assess tumor kill, hepatotoxicity, and hematological toxicity. There have been several reports of microfluidic systems for assessing toxicity of anti-cancer drugs (Fujii et al. 2006; Lee et al. 2007; Sugiura et al. 2008; Wu et al. 2008), but these systems cannot reproduce the pharmacokinetics of drugs. There are commercial 3-D cell culture system for drug screening such as the ones by Synthecon Inc. or Global Cell Solutions Inc. (Becker

and Blanchard 2007; Lederman 2007), but these systems cannot reproduce the PK-PD profiles and can only test the direct effect of a drug, rather than prodrugs. To our knowledge, this is the first report of a 3-D hydrogel microfluidic cell culture system with medium recirculation that examined the metabolism and the toxicity of an anti-cancer drug on multiple cell types simultaneously.

3.2 Materials and Methods

3.2.1 Chemicals and Cell Line

McCoy's 5a medium was purchased from Sigma Aldrich (St Louis, MO). MEM medium, RPMI 1640 medium, and fetal bovine serum (FBS) were purchased from Invitrogen (Carlsbad, CA). A live/dead viability kit was obtained from Invitrogen. HEPES, sodium chloride, uracil, 5-fluorouracil, and Tegafur were purchased from Sigma Aldrich. The colon cancer cell line, HCT-116, was obtained from American Type Culture Collection (ATCC, Manassas, VA) and cultured in McCoy's 5a medium (Sigma Aldrich) with 10% FBS. A hepatoma cell line, HepG2/C3A (ATCC), was maintained in MEM medium with 10% FBS. Myeloblast cell line Kasumi-1 was maintained in RPMI-1640 medium with 20% FBS. Cell lines were cultured in an incubator at 37℃ with 5% CO_2.

3.2.2 Design and Fabrication of a μCCA

The methods for design and fabrication of a μCCA have been elaborated elsewhere (Sin et al. 2004; Viravaidya et al. 2004). In this study we designed a three-chamber μCCA for liver, colon cancer and bone marrow cells (Figure 3.1). Each chamber was designed so that they would have residence times that closely match the

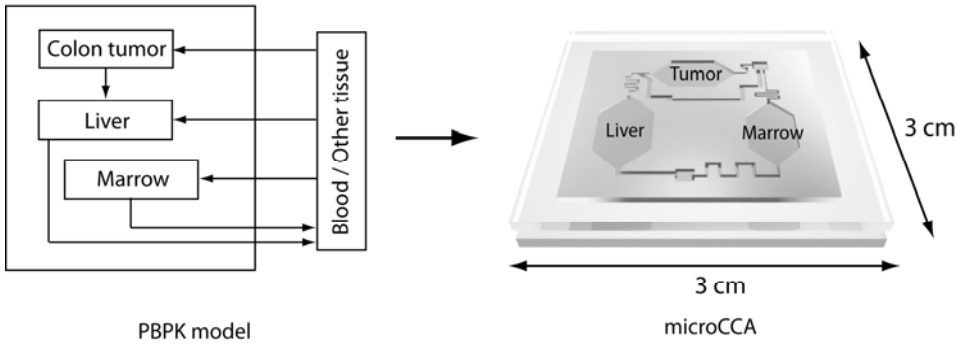

Figure 3.1 A mathematical PBPK model and a corresponding μCCA

A μCCA consists of liver, tumor and marrow chamber, interconnected with channels mimicking the blood flow pattern in human body. The compartments inside the box in the left figure are fabricated on a μCCA chip shown on right, and the blood compartment and all the other organs are represented by medium reservoir, which is not shown in the figure, to match the dynamic hold up of fluid that would be retained in other tissues. Colon cancer cell line (HCT-116) is cultured in the tumor chamber, and hepatoma cell line (HepG2/C3A) is cultured in the liver chamber. Myeloblast cell line (Kasumi-1) was cultured in the marrow chamber.

physiological residence times of blood in the corresponding organs in the human body (Davies and Morris 1993). A medium reservoir that acts as a debubbler represents all other tissues. The flow rates and the pressure drops across a microfluidic network can be analyzed by an analogy to an electric circuit (Ajdari 2003). The resistance across channels and chambers were adjusted by controlling the geometries (widths and lengths) so that chambers would have the desired residence times at given chamber volumes and a flow rate.

The μCCA chips were fabricated using conventional photolithographic techniques. The μCCA was drawn using a software AutoCAD (Autodesk, San Rafael, CA), and a mask was made by GCA/MANN 3600F Optical Pattern Generator (Ultratech, San Jose, CA). Photoresist Shipley 1813 (Shipley, Marlborough, MA) was spin coated on a 50 mm diameter silicon wafer at 3000 rpm, and the pattern from the mask was exposed using a contact aligner (AB-M HTG 3HR Contact Proximity Aligner, San Jose, CA). The pattern was etched by inductively coupled plasma ion etcher (Plasmatherm 770, Zurich, Switzerland) to 100 μm depth. After removing the photoresist, the silicon wafer was cut into 1 inch by 1 inch pieces with a wafer saw.

To measure the fluid velocity more accurately, the movement of polystyrene microspheres (FluoSpheres, 10 μm, blue-green, Invitrogen, Carlsbad, CA) was recorded with a fluorescent microscope (Fisher Scientific; Pittsburgh, PA) and a CCD camera (Fisher Scientific), and the fluid velocity was calculated. The thickness of Matrigel inside a μCCA chamber was measured by comparing the fluid velocity in the presence of the gel with the velocity in the absence of the gel at the same volumetric flow rate. With a given flow rate, the presence of a gel would result in a shallower chamber, resulting in an increased fluid velocity. By comparing the fluid velocity in the two conditions, the thickness of the gel could be back-calculated.

3.2.3 Incorporation of Hydrogel into a μCCA and Assembly of a μCCA Device

Incorporation of cell-embedded Matrigel (BD Matrigel™ Basement Membrane Matrix, 5 ml LDEV-Free, BD Biosciences, San Jose, CA) into a μCCA was achieved by gel formation on μCCA chips with the shrinkage of Matrigel during gelling process (Figure 3.2(a)). The Matrigel™ was thawed in a refrigerator overnight and diluted three-fold in McCoy's 5a medium. A desired number of cells re-suspended in diluted Matrigel in a 1 ml centrifuge tube to the final concentration $1x10^7$ cells/ml. The tubes were kept in an ice bath to prevent premature gel formation. A base frame with a 1 mm thick silicone gasket (Grace Bio Labs, Bend, OR) on top was placed in an ice bath, and a μCCA chip was placed on top of the silicone gasket. 10 μL of cell-Matrigel mixture was pipetted onto a chamber. After 10 minutes at room temperature, 1 ml of DPBS was pipetted onto each μCCA chip, and the polycarbonate top housing was secured with screws. After the assembly, the μCCA devices were incubated at 37℃ for 1 hour for complete gel formation. Since the shrinking process results in withdrawal of outside air through the inlet and outlet holes, 200 μL of cell culture medium was pipetted on the inlet and outlet holes to prevent air withdrawn into the device.

To encapsulate cells in alginate, 1% (w/v) sodium alginate (10/60 LF sodium alginate, FMC biopolymer) was made in HEPES solution (15 mM HEPES, 117 mM sodium chloride), and filtered through a sterile 0.2 μm pore size syringe filter (VWR scientific, West Chester, PA). Cell suspension in the 1% alginate solution at $3x10^6$ cells/ml was prepared and 2 μL of the cell suspension was pipetted into a chamber in a μCCA followed by 30 mM calcium chloride solution (Figure 3.2(b)). After the gel was formed, the μCCA chip was flooded with DPBS and a polycarbonate top cover was closed. Figure 3.3(a) shows the schematic diagram of a μCCA with top and bottom housing pieces, and a picture of an assembled μCCA in Figure 3.3(b).

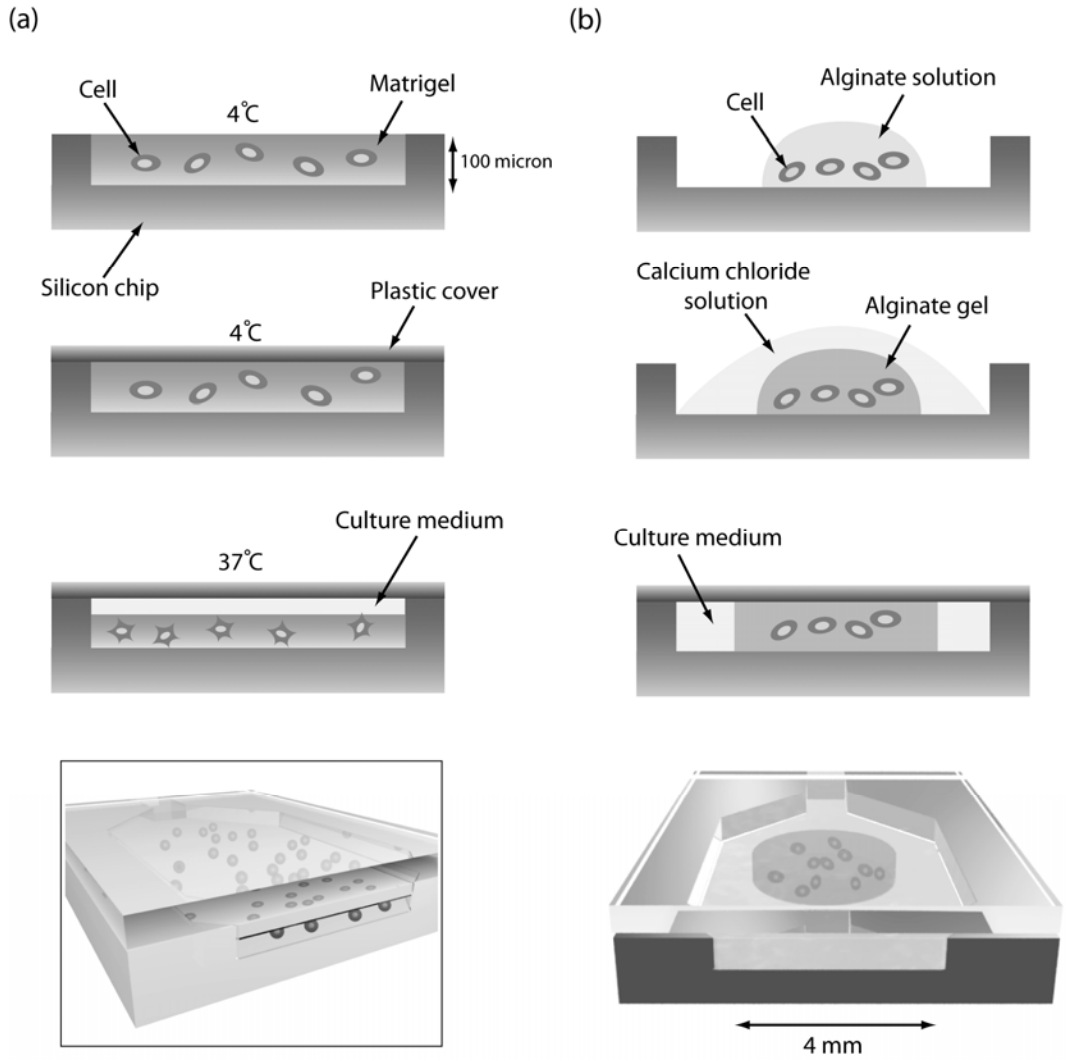

Figure 3.2 Incorporation of hydrogel into a μCCA

(a) Schematic diagrams describing the incorporation of Matrigel hydrogel into a μCCA. Cell-embedded Matrigel is inserted into a chamber in a liquid state and the device is sealed with a plastic top cover and a bottom housing piece. After the sealing, the gel is formed by raising the temperature. (b) Incorporation of alginate hydrogel into a μCCA. A drop of cell suspension in alginate solution is placed inside a chamber and the gel is formed by addition of calcium chloride solution. By sealing with the top cover, a disk-shaped hydrogel is formed inside the chamber.

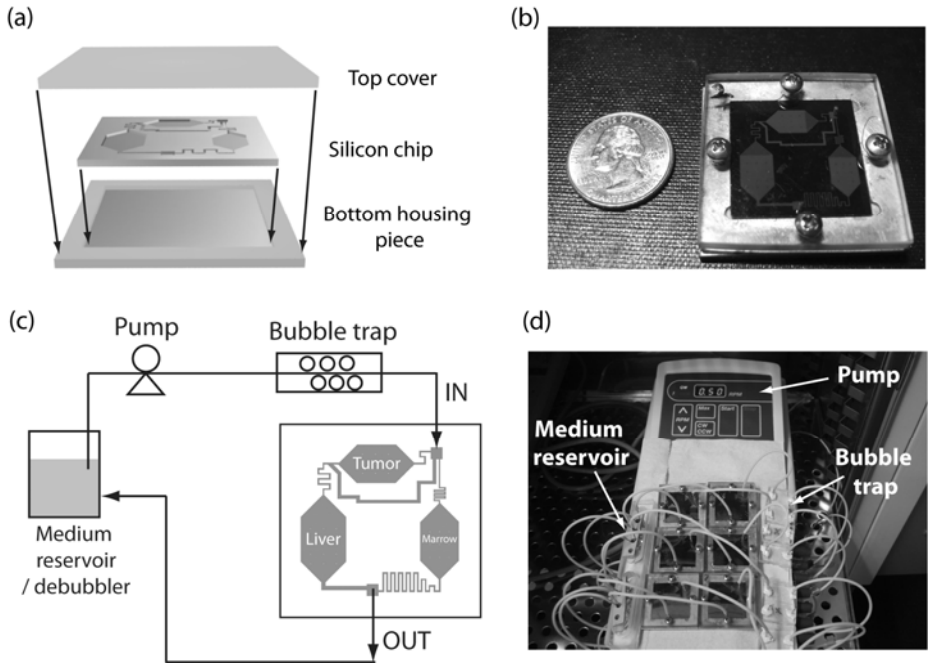

Figure 3.3 Assembly and operation of a μCCA

(a) Schematic diagram showing how the μCCA is assembled. The silicon μCCA chip with features on top is sandwiched between the plastic top cover and an aluminum bottom housing with a recess. The sealing is secured by screws around the edges of the housing. (b) A picture of an assembled μCCA with red dye for visualization of channels and chambers. (c) Schematic diagram of operation setup of a single μCCA with medium recirculation. Medium is withdrawn from a reservoir, which also functions as a debubbler, and goes through a bubble trap for further prevention of bubble trapping inside a μCCA. After circulating through the channels and chambers in a μCCA, medium goes back to the reservoir for recirculation. (d) Picture of the μCCA system with multiple chips.

3.2.4 Operation of a μCCA and Cell Viability Analysis

Before the assembly of a μCCA, sterilized PharMed tubings (0.25 mm inside diameter, Cole Parmer, Vernon Hills, IL) were installed on a peristaltic pump (Watson-Marlow, Wilminton, MA), and 99.5% ethanol (Sigma Aldrich) was passed through the tubing for 1 hour to remove air bubbles. Then the tubing was thoroughly washed with sterile water for 2 hours, and bubble traps were connected to the tubing and flushed with sterile water. A microscale bubble trap was designed to prevent small air bubbles from entering the μCCA and interfering with the flow (chapter 4). The whole system was placed inside an incubator. The flow diagram and a picture of the assembled system are shown in Figure 3.3(c) and 3.3(d), respectively.

Cell viability inside the device was measured by staining the cells with live/dead staining solution (5 μM calcein AM and 5 μM ethidium homodimer-1 in DPBS, Invitrogen). The medium reservoir was switched to the live/dead staining solution and μCCA chips were perfused for 1 hour. The sample was analyzed by fluorescent microscope and a CCA camera. Fluorescent images of cells in a μCCA were taken, and the areas occupied by the live and dead cells were calculated using image-processing software CellProfiler (Broad Institute, Cambridge, MA). The viability of cells was calculated as the ratio of the live cells to the total cells (live + dead cells).

3.2.5 96-well Microtiter Plate Cytotoxicity Assay

In a 96-well microtiter plate assay, cells were resuspended in medium at the concentration of $1x10^6$ cells/ml, and 100 μL of cell suspension was seeded into each well. After overnight incubation, the medium was replaced with medium containing

either 100 μM Tegafur, 5-fluorouracil (5-FU) or nothing (control). 100 μM uracil was also added to all wells to inhibit the rapid degradation of 5-FU (Kajita et al. 2003).

3.2.6 Image Processing

CellProfiler, a software designed for high-throughput image processing, was used for processing the live/dead images of cells inside a μCCA. Briefly, the image processing goes through following cycles. 1) Cropping of the original image. This was done to exclude the edge areas with non-uniform illumination. 2) The cropped image is converted to grayscale. 3) Background illumination function is calculated. 4) Calculated illumination function is applied to the grayscale image to create an image with more uniform background brightness. 5) The area occupied by the cells is calculated. 6) Number of cells inside the image is calculated. The steps 1 through 6 are shown in Figure 3.4.

3.2.8 Simulation of Transport inside a μCCA

Comsol multiphysics modeling software (Burlington, MA) was used to simulate the transport of calcein AM inside a μCCA with alginate. To save simulation time, geometries were reduced to 2D x-y plane. The boundary conditions and parameters used in the simulation are summarized in Table 3.1 and Table 3.2. The simulation was compared with experiment by injecting 5 μM Calcein AM solution in DPBS into a μCCA containing HCT-116 cell-embedded alginate gel and taking fluorescent images of the gel every ten minutes.

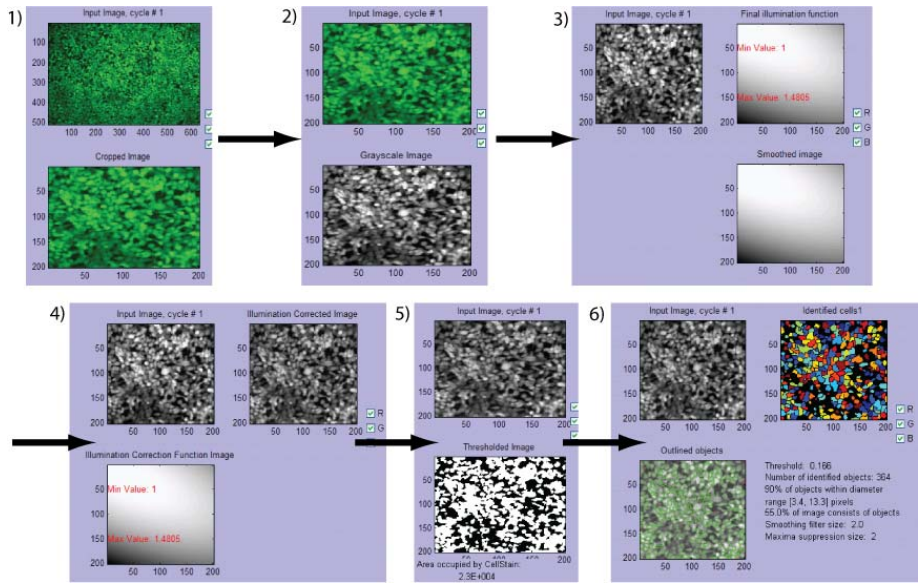

Figure 3.4 Steps of image processing of live cells stained with CalceinAM.

1) Cropping 2) Conversion to grayscale 3) Calculation of illumination function 4) Applying illumination function 5) Calculation of occupied area 6) Calculation of cell number.

Table 3.1 Parameters used in the simulation of diffusion of calcein AM in alginate

Name	**description**	**Value**
v	Average fluid velocity	$1.7*10^{-3}$m/min (from experiment)
$D_{calcein}$	Diffusivity of calcein AM	$2.4*10^{-8}m^2$/min (Choi et al. 2007)
Rho	Density	$1*10^3$ kg m^{-3}
Mu	viscosity	$6*10^{-2}$ kg $m^{-1}min^{-1}$
V_m	Rate constant for calcein AM consumption	$5*10^{-4}$ 1/sec (Choi et al. 2007)
S	Initial substrate concentration	5 μM

Table 3.2 Boundary and sub-domain conditions used in the simulation of diffusion of calcein AM in alginate. N-S: Navier-Stokes, C-D: Convection-diffusion model

Boundary	**N-S**	**C-D**
Inlet	Velocity, u_0=0, v_0=-v	Concentration, c_0=S
Outlet	Pressure, P_0=0	Convective flux
Others	No slip	Insulation/Symmetry
Sub-domain	**N-S**	**C-D**
Perfusion area	ρ=rho, μ=mu	D(isotropic) = $D_{calcein}$
Hydrogel area	No convection	D(isotropic) = D_{ethres}

3.3 Results

3.3.1 Verification of Design and Operation of a μCCA

The residence times and the fluid velocities were measured by tracking the interface between water/fluorescein, and the movement of fluorescent beads, respectively (Table 3.3). Measurement of flow residence time in the liver chamber was not possible since multiple flow channels are merged into the liver chamber, and the interface between two liquids was not maintained. We were able to operate eight μCCA devices simultaneously for 3 days, maintaining good cell viability (>80%). The only limiting factor was the recirculation of cell culture medium. Recirculation eventually led to nutrient depletion and accumulation of metabolic wastes.

3.3.2 Cell Culture in Hydrogel in a μCCA

It was tested whether the assembly process was gentle on cells. The operation of a μCCA with the cell-embedded hydrogel was also tested after 48 hours of operation. Figure 3.5 (a) and (b) shows that cells maintained a high viability immediately after the assembly, and also after 48 hours of a μCCA operation. However, when myeloblasts (Kasumi-1) were also encapsulated in Matrigel and cultured with medium recirculation in a μCCA, unlike other cell types, they failed to remain inside Matrigel after 24 hours. These myeloblasts are a suspension cell type and displayed greater motility than the other cell types used. Therefore, they were encapsulated in alginate, which retained the myeloblasts better than Matrigel in the presence of flow in a μCCA. Figure 3.5(c) shows that myeloblasts encapsulated in alginate in the device remained healthy after 48 hours of culture in the device.

Table 3.3 Comparison of calculated residence times and velocities in each chamber with measured values.

	Tumor	Liver	Marrow
Calculation			
Residence time (s)	70	52	128
Velocity (um/s)	71.5	160.7	53.6
Measurement			
Residence time (s)	69.7±3.8	NA	136.5±2.9
Velocity (um/s)	68.9±1.6	167.9±6.2	58.6±0.5

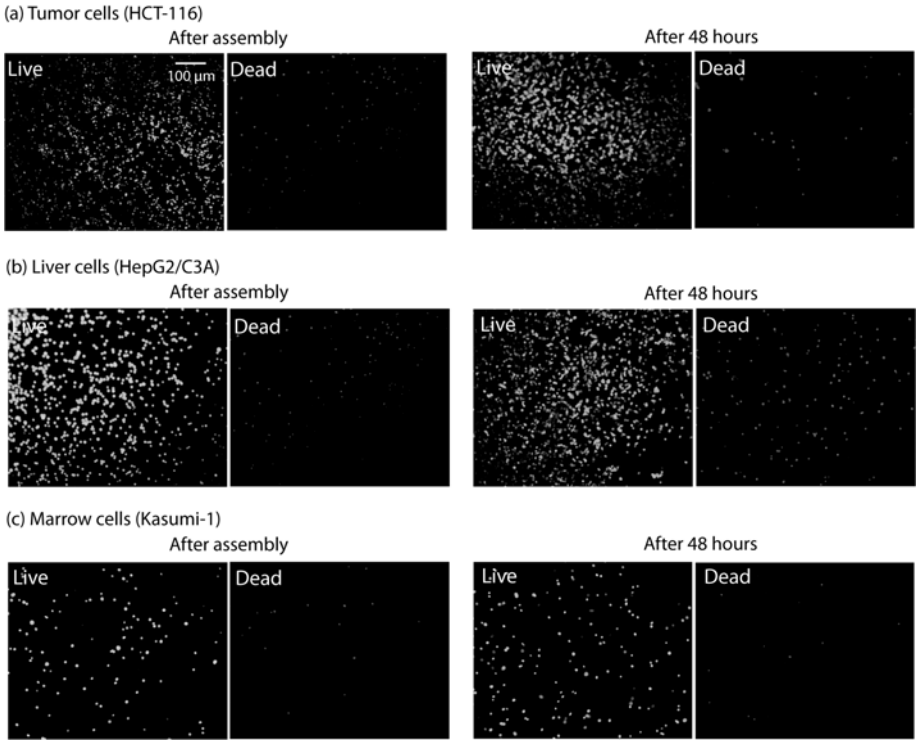

Figure 3.5 Pictures of live/dead staining of cells cultured in a μCCA.

(a) Tumor cells in Matrigel (b) liver cells in Matrigel (c) myeloblast cells in alginate in the device immediately after the device was assembled and after 48 hours of a μCCA operation with medium recirculation.

The thickness of Matrigel was characterized by comparing the flow rate with and without the gel. The presence of Matrigel matrix inside the chambers of a μCCA would result in shallower chamber, and therefore higher flow velocity at a given volumetric flow rate. When multiple μCCA chips were assembled using the described protocol and the flow velocity in each chip was measured, the fluidic velocity increased by approximately 40% over the case when the gel was not inserted, implying the gel thickness of approximately 40 μm in a 100 μm deep chamber.

The morphologies of tumor and liver cells embedded in Matrigel inside a μCCA were compared with the same cells cultured in 2-D monolayer in a μCCA. To culture cells in 2-D monolayer in a μCCA, cells were plated in corresponding chambers in a μCCA the day before, and after overnight incubation for cell attachment, a μCCA was assembled by closing the top and bottom base frames. The pictures shown in Figure 3.6 were taken after 2-days of a μCCA operation in both cases of Matrigel and monolayer culture in a μCCA. Initially cells are round immediately after being encapsulated in Matrigel (Figure 3.5(a) and 3.5(c)), and after two days they were observed to have more elongated morphology (Figure 3.6(a) and (b), left). However, the cells were less elongated when compared to the cells cultured in 2-D monolayer (Figure 3.6, right). The less elongated cell morphologies were similarly observed in cells encapsulated in Matrigel in a 96-well microtiter plate.

3.3.3 Toxicity of Tegafur and 5-FU

5-fluorouracil (5-FU) is an anti-cancer drug that has been widely used for colon cancer (Longley et al. 2003). However, 5-FU has an unpredictable bioavailability when taken orally, and is subject to a rapid degradation by the enzyme dihydropyrimidine dehydrogenase (DPD), resulting in a low response rate when

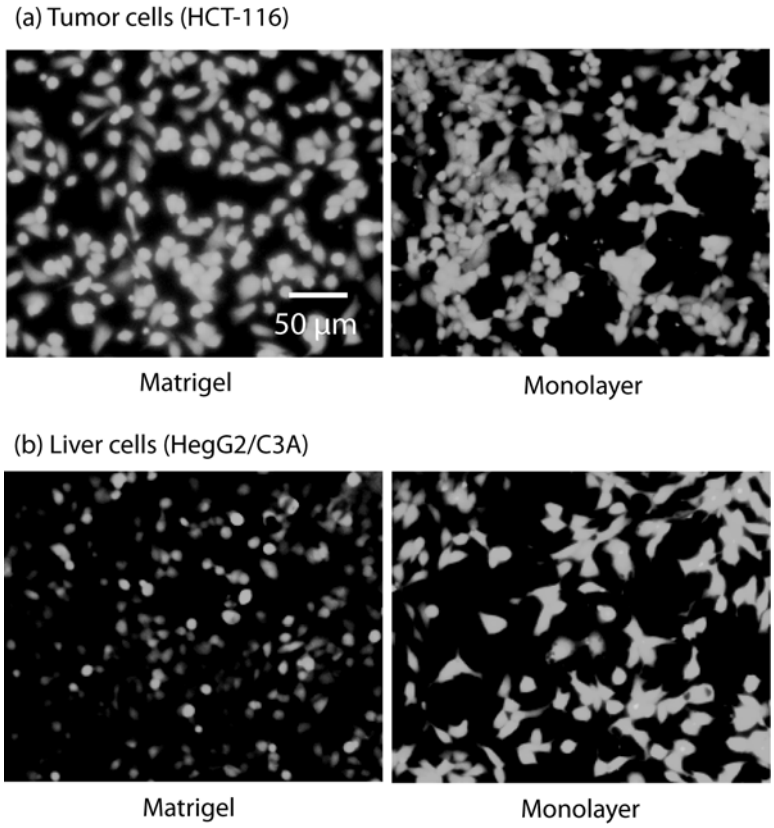

Figure 3.6 Morphology of tumor and liver cells cultured in Matrigel and in monolayer in a µCCA.

administered alone (Malet-Martino and Martino 2002). Tegafur is an oral prodrug of 5-FU, and has a better oral bioavailability. It is not cytotoxic to tumor cells, but becomes cytotoxic after conversion to 5-FU by P450 enzymes in the liver. In addition, uracil is often added to Tegafur to inhibit the degradation of 5-FU by DPD enzyme. Uracil is a natural substrate of DPD, and competes with 5-FU for the enzyme. Since DPD is a major route for elimination of 5-FU, combination of uracil with Tegafur (often called UFT) significantly enhances the pharmacokinetic profile of 5-FU, consequently resulting in a better therapeutic index (see Figure 2.1) (Bissett et al. 2000).

The cytotoxicity of Tegafur on tumor cells was tested in a 96-well microtiter plate first. HCT-116 cells were incubated with medium containing 100 μM Tegafur for three days and cell viability was measured each day by live/dead staining (Figure 3.7(a)). Uracil was added to the medium to inhibit rapid degradation of 5-FU by DPD. Cells incubated with 100 μM Tegafur maintained a high viability for three days almost comparable to the control (no drug), although on day 3 cell viability dropped slightly, possibly due to a spontaneous degradation of Tegafur into 5-FU in the culture medium (Ikeda et al. 2000). On the other hand, 100 μM 5-FU caused a significant decrease in the viability of tumor cells in a time-dependent manner, as expected.

The cytotoxicity of Tegafur was tested in a μCCA containing HepG2/C3A (hepatoma cell line) in the liver compartment, HCT-116 (colon cancer cell line) in the tumor compartment, and Kasumi-1 (myeloblasts) in the marrow compartment. 100 μM Tegafur with 100 μM uracil was added to the recirculating medium (Figure 3.7(b)). The response of tumor cells to Tegafur in a μCCA was different from that of tumor cells in a 96-well plate. Tumor cells treated with Tegafur showed significantly lower cell viability than the control cultures without Tegafur ($p<0.01$). This observation was consistent with the hypothesis that Tegafur was converted to 5-FU by HepG2/C3A

cells in the liver compartment and the metabolite, 5-FU, recirculated into the tumor chamber and exerted the toxic effect on the HCT-116 cells. We tested this by running the same experiment without HepG2/C3A cells. As expected, Tegafur showed a considerably weaker cytotoxic effect than when the liver cells (HepG2/C3A) were present in the system, as seen in Figure 3.7(b). A small drop in the cell viability observed with Tegafur without the liver cells is thought to be due to a low level of Tegafur conversion by HCT-116 cells and by spontaneous conversion, similar to the situation with HCT-116 cells treated with Tegafur in a 96-well microtiter plate. However, as observed in the result, the contribution of the liver cells to the conversion was significantly greater than the contribution of HCT-116 cells and the non-specific conversion, and the removal of liver cells from the system eliminated most of the cytotoxicity due to Tegafur. 5-FU showed toxicity to tumor cells in a time-dependent manner, as expected. It is notable that the cytotoxic effect of 5-FU was observed more quickly than the effect of Tegafur, which can be explained by the time needed for Tegafur to be converted to 5-FU. The effect of uracil as a modulator of Tegafur toxicity was tested in a μCCA by administering Tegafur without uracil (Figure 3.7(c)). As expected, tumor cells treated with Tegafur alone in a μCCA showed a higher viability than the cells treated with Tegafur and uracil in a μCCA.

The toxicity of 5-FU and Tegafur on liver cells and myeloblasts were measured, representing hepatotoxicity and hematological toxicity, respectively. Figure 3.8(a) shows the viability of liver cells (HepG2/C3A) treated with Tegafur or 5-FU in a μCCA. In both cases Tegafur and 5-FU had cytotoxic effect on the liver cells, although the liver cells were considerably less sensitive to the drugs than colon cancer cell line (HCT-116). It is also notable that 5-FU had a greater effect than Tegafur at each time point, similar to Figure 3.7(b). The effect of Tegafur and 5-FU on myeloblast cell line Kasumi-1 was tested in two-day experiment in a μCCA (Figure

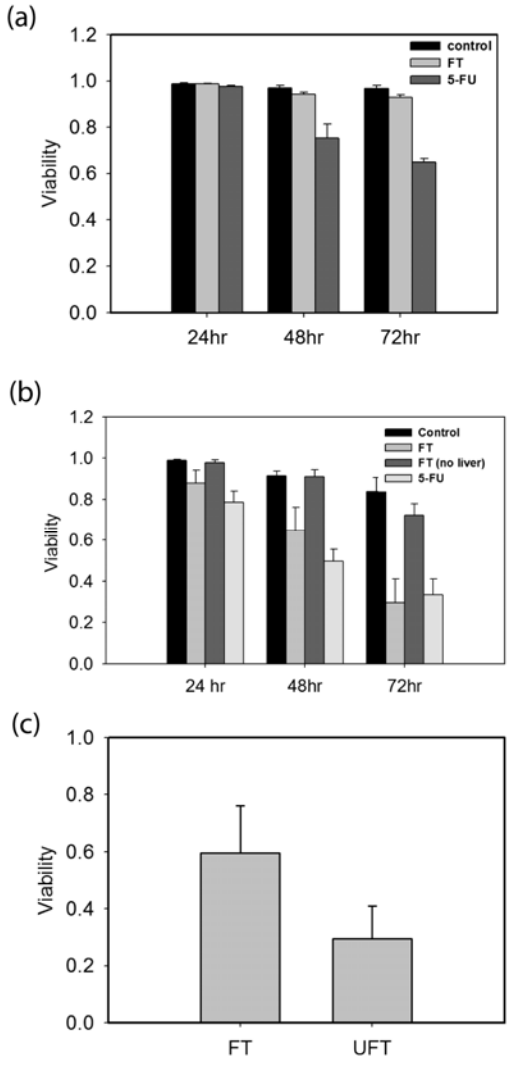

Figure 3.7 Cytotoxicity of Tegafur on tumor cells

(a) Cytotoxicity experiment results of Tegafur in a 96-well microtiter plate. Tegafur does not exert cytotoxic effect on HCT-116 cells (colon cancer cell line), whereas 5-fluorouracil induces cell death after two days. (b) In a μCCA with liver and tumor cells, Tegafur has cytotoxic effect on HCT-116 cells. When liver cells (HepG2/C3A) were removed, the cytotoxic effect of Tegafur was considerably reduced. (c) Effect of a modulator, uracil, on the toxicity of Tegafur in a μCCA with liver and tumor cells.

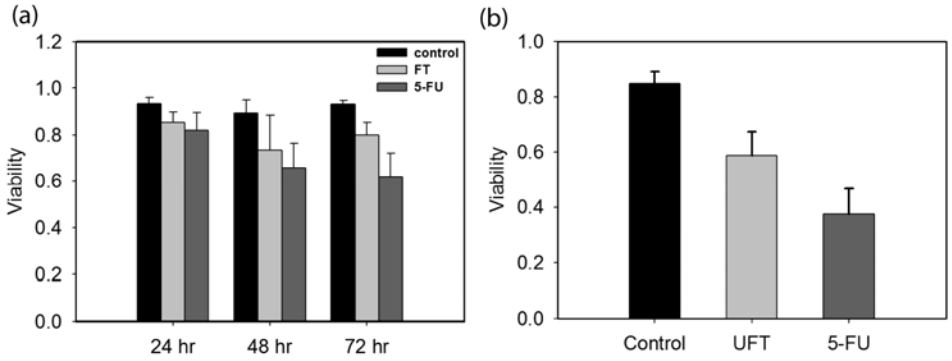

Figure 3.8 Cytotoxicity of Tegafur on liver and marrow cells

(a) Toxicity of Tegafur and 5-FU on liver cells (HepG2/C3A) in a μCCA with liver and tumor cells. Both drugs showed toxicity on the cells, but liver cells are less sensitive to the drugs than tumor cells. (b) Toxicity of Tegafur and 5-FU on myeloblast cells (Kasumi-1) in a μCCA with liver, tumor, and myeloblasts in two-day experiment. Both 5-FU and Tegafur showed toxicity to the cells. The difference between the control and UFT treated myeloblasts was statistically significant ($p<0.01$).

3.8(b)). Myeloblasts showed decreasing viability in response to both 5-FU and Tegafur in a μCCA. The extent of cell death was similar to the tumor cells at 48 hour.

3.3.4 Gradient Formation inside Alginate

It has been known that the transport inside a hydrogel is dominantly diffusive (Brown et al. 2007). Due to the geometry of an alginate gel inside a μCCA, molecules would have to diffuse into the gel to reach the center area. Therefore, it was possible to form a gradient of chemicals across the area of hydrogel inside a μCCA. The formation of a gradient was analyzed by flowing Calcein AM solution through a μCCA. The Calcein AM is cell membrane permeable and can diffuse through alginate and into the cells. Once inside the cell, Calcein AM is hydrolyzed by intracellular esterase enzymes and becomes fluorescent, which is sequestered inside the cell since the hydrolyzed product is not cell membrane permeable. Due to the diffusion limitation inside alginate, cells located near the periphery will be stained faster than the cells located near the center. Figure 3.9(a) shows that the formation of a gradient results in differential fluorescent staining of cells. The mathematical simulation in Figure 3.9(b) also agrees with the experimental result that a gradient of Calcein AM is formed across the diameter of the circular gel. As verified by the experiment and the simulation using Calcein AM, it is expected that a gradient of nutrient would be formed inside the gel. Consequently, it was observed that after three days of operation there was a significant geometric variation in the viability of cells. Although this was undesirable for our purpose, this feature may have an application in case where the formation of gradient is desirable, such as *in vitro* liver zonation (Camp and Capitano 2007).

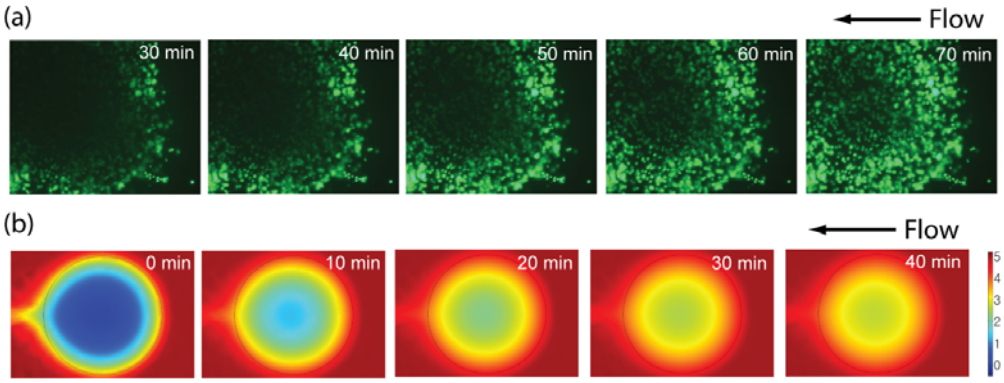

Figure 3.9 Formation of gradient in alginate hydrogel inside a μCCA

(a) Pictures of HCT-116 cells stained with calcein AM. As calcein AM diffuses into the gel, the cells in the peripheral area stain quicker than the cells in the center area. The time shown in the upper-right corner of the pictures is the time after the beginning of perfusion of the staining solution. (b) Mathematical simulation of diffusion of calcein AM into the gel inside a μCCA. Even after 40 minutes the concentration of calcein AM in the center area is maintained relatively low. In both cases the direction of the flow was from right to left. There was a time lag of approximately 30 minutes for the hydrolysis reaction to take place inside the cell and show fluorescent signal.

3.4 Discussion

3.4.1 Long-term Operation of a μCCA

The measurement of residence times of the flow in each chamber in a μCCA verifies that the fabrication of the device was done accurately according to the flow rate calculation. However, during three days of operation, occasional trapping of air bubbles inside the channels or chambers resulted in a drastic change in the flow distribution and cell death in the chambers which did not get enough supply of medium. Thus a way of preventing air bubbles from entering a μCCA during the operation was devised. Bubble prevention was more important in case of long term operation of the device (several days) than short term operation (several hours). Even after extensive flushing with sterile water before the start of experiment, air bubbles were eventually trapped within the system after operating for several days due to air leakage through the interface between the tubing and a μCCA. Installment of a bubble trap on the front end of a μCCA improved the bubble issue significantly, enabling 3-day operation.

3.4.2 3-D Hydrogel Cell Culture in a μCCA

In this study, a hydrogel cell culture in a μCCA was explored using Matrigel and alginate, which have different properties and mechanisms of gel formation. Matrigel is a natural basement membrane matrix obtained from Engelbreth-Holm-Swarm (EHS) mouse sarcoma, and is a mixture of various proteins including growth factors and extracellular matrix proteins such as laminin and collagen, which stays liquid at 4℃ but self-assembles into a gel when incubated at 37℃ (Brown et al. 2007). This feature allows formation of a gel after the sealing of a μCCA, since a gel can be

formed simply by raising the temperature, and there is no need to add extra reagent. Shrinking of a gel during gelling process provides space on top of the gel for medium, resulting in a thin layer of cell-embedded matrix. This characteristic has been exploited to create a thin layer of Matrigel in a microfluidic channel by filling a sealed channel with Matrigel and incubating the device at 37℃ (Frisk et al. 2005). We utilized this technique with modifications to create a thin layer of cell-embedded Matrigel inside a μCCA.

On the other hand, alginate is a linear copolymer of mannuronate (M) and guluronate (G) which forms a gel in the presence of multivalent cations (Peirone et al. 1998). Formation of alginate gel is achieved by adding calcium chloride solution to the alginate solution. The requirement of adding extra reagent for gel formation made it difficult to create a thin layer of cell-embedded hydrogel. Instead, a cylindrical shape of hydrogel (~3 mm in diameter) was created inside the cell culture chamber of a μCCA. The difference in the mode of gel formation and the resulting geometries of hydrogel inside the device would result in a different microenvironment within the hydrogel. For instance, the thin geometry of Matrigel formed essentially eliminated the transport limitation and gradient formation often observed in 3-D hydrogel structure. This was evident from a cell staining experiment, where cells were quickly and uniformly stained within 30 minutes after starting perfusion of the staining solution. In case of alginate, which has a greater diffusion length, a chemical gradient would be observed with cells exhibiting the stain in non-uniform manner.

Three cell lines were used in this study; HCT-116, HepG2/C3A and Kasumi-1. HCT-116 is an epithelial cell originated from colorectal carcinoma, and represents tumor compartment. HepG2/C3A, representing the liver, is a derivative cell line of HepG2, and is originated from hepatocellular carcinoma. It has nitrogen metabolizing activity comparable to perfused rat livers, and relatively higher cytochrome P450

activity than HepG2 cells (Kelly 1994). Kasumi-1 is a myeloblast cell line originated from leukemia, and was chosen from the fact that neutropenia is one of the main hematological toxicities observed in patients treated with 5-FU related chemotherapy (van Kuilenburg 2004; Testart-Paillet et al. 2007). HCT-116 and HepG2/C3A are anchorage-dependent cell types and were well maintained inside Matrigel. Presumably these cells would attach to various proteins in the Matrigel. When Kasumi-1, which is suspension cell type, was cultured inside Matrigel, they escaped from the hydrogel matrix upon medium perfusion. From a separate study where the same cells were encapsulated in Matrigel and placed in a 96-well microtiter plate, they remained viable inside Matrigel for several days. Therefore, it seemed that the presence of fluid flow was causing the loss of cells from Matrigel in a μCCA. Since alginate retained myeloblasts better in the presence of flow than Matrigel, we encapsulated the cells in alginate and other anchorage-dependent cell types in Matrigel.

One important factor in achieving a realistic pharmacokinetic profile of a drug *in vitro* is the authentic behavior of cells, especially liver cells. A microfluidic system with 3-D hydrogel cell culture can be a potential partial solution to the issue of achieving authentic cell response. When cells are cultured in a μCCA, ECM proteins constituting Matrigel can provide chemical signals while medium perfusion provides mechanical signals. Although cells are embedded in Matrigel and are not directly exposed to the flow, the Matrigel layer inside a μCCA is relatively thin (~40μm thick), and since Matrigel is easily deformed, the mechanical cues can be propagated through the 3-D matrix of Matrigel to the embedded cells. It has been found that chondrocytes embedded in collagen gels respond to mechanical stimulation by altered gene expression profiles and extracellular matrix synthesis (Hunter et al. 2002).

3.4.3 Toxicity of Chemotherapeutic Agents in a 96-well Plate and a μCCA

When the cytotoxic effect of Tegafur and 5-FU on HCT-116 cells was tested in a 96-well microtiter plate, Tegafur showed only a slight cytotoxic effect, whereas 5-FU caused significant cell death during the 3-day culture. A small drop in the viability of cells treated with Tegafur on day 3 is thought to be due to a small amount of 5-FU produced from spontaneous conversion of Tegafur *in vivo* (Tanaka et al. 2000). In a separate experiment, we observed a small but detectable P450 1A2 activity in the tumor cell line (HCT-116), although much lower than that of HepG2/C3A (data not shown). With P450 1A2 being one of the major enzymes involved in the conversion of Tegafur into 5-FU (Komatsu et al. 2000), incubation of Tegafur with HCT-116 cells could have generated a low level of 5-FU, which caused a small, but detectable toxicity to the cells. In contrast, Tegafur exerted toxic effect on cells when it was tested in a μCCA. In addition, combining uracil with Tegafur was shown to enhance the cytotoxic effect of Tegafur on tumor cells. The cytotoxic effect of Tegafur and the enhancement of anti-tumor effect of Tegafur by uracil observed are consistent with previous findings in animal and human clinical studies (Rustum 1997; Bissett et al. 2000; Tanaka et al. 2000; Malet-Martino and Martino 2002).

It is interesting to note that the response of tumor cells to 5-FU was greater in a μCCA than in a 96-well microtiter plate. This observation may be partially explained by the fact that when cells are cultured in monolayer in a 96-well microtiter plate, dead cells may detach from the surface and will not be included in the counting of dead cells, whereas when cells are encapsulated in a matrix in a μCCA, most of dead cells will be retained within the matrix even after cell death. Another explanation for the difference in the observed sensitivity of tumor cells to the drugs may be the combined effect of Matrigel environment and a microfluidic environment, such as

shear. It has been reported that the response of tumor cells to anti-tumor agents was drastically different when cultured in 3-D compared from when they were cultured in monolayer (Horning et al. 2008). Tumor cell cycle arrest induced by exposure to shear stress was observed by Chang et al (Chang et al. 2008). Consistent with the explanation, when cells were plated in monolayer in a μCCA and treated with 5-FU, the observed cytotoxic effect appeared to be weaker than when cells were in Matrigel in a μCCA (tumor cells seeded in monolayer in a μCCA showed 71±8.8% viability 48 hours after 5-FU treatment, compared to 50±5.9% for the same cells in Matrigel in a μCCA). It is uncertain which factor contributes the most to the different response of tumor cells, and the effect may be synergistic.

The responses of liver cells (HepG2/C3A) and marrow-related cells (Myeloblasts, Kasumi-1) to Tegafur and 5-FU were also examined. In general, the responses were consistent with tumor cells, in that both Tegafur and 5-FU showed toxicity to both the HepG2/C3A and Kasumi-1 cell lines, with slightly greater response to 5-FU than Tegafur. However, there were some quantitative differences in the responses, depending on the cell types examined. Liver cells were considerably less sensitive to Tegafur and 5-FU than tumor cells, whereas the sensitivity of myeloblasts to the drugs was similar to the tumor cells. Typically, hematological toxicity is a more serious, often dose-limiting toxicity of 5-FU related chemotherapy, whereas hepatotoxicity is a relatively less serious problem (van Kuilenburg 2004; Testart-Paillet et al. 2007), which is consistent with the observed response in a μCCA. The mode of action of Tegafur combined with uracil is an example of complex interaction of multiple organs; the conversion of Tegafur to 5-FU and inhibition of 5-FU degradation by uracil mainly occur in the liver, whereas the cytotoxic effect of 5-FU is observed in the tumor. Previously, *in vivo* experiments have been the only way to test the effect of a combination of Tegafur and uracil. For example, the optimal

combination ratio of uracil to Tegafur was determined based on a test using a rat where the concentrations of 5-FU in the tumor and the blood were measured after administration of various combination ratios (Fujii et al. 1979). However, doing a similar study in human clinical trials would be difficult, since the number of patients required would be high. We believe that the μCCA system can be useful in complementing animal and human studies.

3.5 Conclusion

A micro cell culture analog (μCCA) with 3-D hydrogel cell cultures was developed and used to test Tegafur, the oral prodrug of an anticancer drug, 5-Fluorouracil. Matrigel and alginate were used to encapsulate cells that were inserted into chambers of a μCCA. Using a μCCA, the cytotoxic effect of Tegafur was observed, which was not seen in a 96-well plate. The toxicity of the drug on tumor cells, liver cells, and myeloblasts were assessed to quantify tumor killing effect, hepatotoxicity, and hematological toxicity, respectively. The response of those cell lines to Tegafur and 5-FU combined with uracil were consistent with previously published clinical results. These results demonstrate that a μCCA is able to test the metabolism-dependent toxicity of anti-cancer drugs.

REFERENCES

Ajdari, A. (2003). "Steady flows in networks of microfluidic channels: building on the analogy with electrical circuits " Comptes Rendus Physique 5(5): 539-546.

Becker, J. L. and D. K. Blanchard (2007). "Characterization of primary breast carcinomas grown in three-dimensional cultures." J Surg Res 142(2): 256-62.

Bissett, D., et al. (2000). "Oral fluoropyrimidines in the treatment of colorectal cancer." Clin Oncol (R Coll Radiol) 12(4): 240-5.

Brown, D. A., et al. (2007). "Analysis of oxygen transport in a diffusion-limited model of engineered heart tissue." Biotechnol Bioeng 97(4): 962-75.

Camp, J. P. and A. T. Capitano (2007). "Induction of zone-like liver function gradients in HepG2 cells by varying culture medium height." Biotechnol Prog 23(6): 1485-91.

Chang, S. F., et al. (2008). "Tumor cell cycle arrest induced by shear stress: Roles of integrins and Smad." Proc Natl Acad Sci U S A 105(10): 3927-32.

Choi, N. W., et al. (2007). "Microfluidic scaffolds for tissue engineering." Nat Mater 6(11): 908-15.

Cushing, M. C. and K. S. Anseth (2007). "Materials science. Hydrogel cell cultures." Science 316(5828): 1133-4.

Daley, W. P., et al. (2008). "Extracellular matrix dynamics in development and regenerative medicine." J Cell Sci 121(Pt 3): 255-64.

Davies, B. and T. Morris (1993). "Physiological parameters in laboratory animals and humans." Pharm Res 10(7): 1093-5.

Frisk, T., et al. (2005). "A concept for miniaturized 3-D cell culture using an extracellular matrix gel." Electrophoresis 26(24): 4751-8.

Fujii, S., et al. (1979). "Effect of coadministration of uracil or cytosine on the anti-tumor activity of clinical doses of 1-(2-tetrahydrofuryl)-5-fluorouracil and level of 5-fluorouracil in rodents." Gann 70(2): 209-14.

Fujii, S., et al. (2006). "Microbioassay system for an anti-cancer agent test using animal cells on a microfluidic gradient mixer." Anal Sci 22(1): 87-90.

Horning, J. L., et al. (2008). "3-D tumor model for in vitro evaluation of anticancer drugs." Mol Pharm 5(5): 849-62.

Hunter, C. J., et al. (2002). "Mechanical compression alters gene expression and extracellular matrix synthesis by chondrocytes cultured in collagen I gels." Biomaterials 23(4): 1249-59.

Ikeda, K., et al. (2000). "Bioactivation of tegafur to 5-fluorouracil is catalyzed by cytochrome P-450 2A6 in human liver microsomes in vitro." Clin Cancer Res 6(11): 4409-15.

Kajita, J., et al. (2003). "The contribution of cytochrome P450 to the metabolism of tegafur in human liver." Drug Metab Pharmacokinet 18(5): 303-9.

Kelly, J. H. (1994). Permanent human hepatocyte cell line and its use in a liver assist device. US patent. No. 5,290,684.

Kim, L., et al. (2007). "A practical guide to microfluidic perfusion culture of adherent mammalian cells." Lab Chip 7(6): 681-94.

Komatsu, T., et al. (2000). "Roles of cytochromes P450 1A2, 2A6, and 2C8 in 5-fluorouracil formation from tegafur, an anticancer prodrug, in human liver microsomes." Drug Metab Dispos 28(12): 1457-63.

Lederman, L. (2007). "High-content screening." Biotechniques 43(1): 25, 27, 29.

Lee, P. J., et al. (2007). "Microfluidic System for Automated Cell-based Assays." JALA Charlottesv Va 12(6): 363-367.

Longley, D. B., et al. (2003). "5-fluorouracil: mechanisms of action and clinical strategies." Nat Rev Cancer 3(5): 330-8.

Malet-Martino, M. and R. Martino (2002). "Clinical studies of three oral prodrugs of 5-fluorouracil (capecitabine, UFT, S-1): a review." Oncologist 7(4): 288-323.

Peirone, M., et al. (1998). "Encapsulation of various recombinant mammalian cell types in different alginate microcapsules." J Biomed Mater Res 42(4): 587-96.

Rustum, Y. M. (1997). "Mechanism-based improvement in the therapeutic selectivity of 5-FU prodrug alone and under conditions of metabolic modulation." Oncology 54 Suppl 1: 7-11.

Sin, A., et al. (2004). "The design and fabrication of three-chamber microscale cell culture analog devices with integrated dissolved oxygen sensors." Biotechnol Prog 20(1): 338-45.

Sugiura, S., et al. (2008). "Pressure-driven perfusion culture microchamber array for a parallel drug cytotoxicity assay." Biotechnol Bioeng 100(6): 1156-65.

Tanaka, F., et al. (2000). "The history, mechanism and clinical use of oral 5-fluorouracil derivative chemotherapeutic agents." Curr Pharm Biotechnol 1(2): 137-64.

Testart-Paillet, D., et al. (2007). "Contribution of modelling chemotherapy-induced hematological toxicity for clinical practice." Crit Rev Oncol Hematol 63(1): 1-11.

van Kuilenburg, A. B. (2004). "Dihydropyrimidine dehydrogenase and the efficacy and toxicity of 5-fluorouracil." Eur J Cancer 40(7): 939-50.

Viravaidya, K., et al. (2004). "Development of a microscale cell culture analog to probe naphthalene toxicity." Biotechnol Prog 20(1): 316-23.

Wong, A. P., et al. (2008). "Partitioning microfluidic channels with hydrogel to construct tunable 3-D cellular microenvironments." Biomaterials 29(12): 1853-61.

Wu, L. Y., et al. (2008). "Microfluidic self-assembly of tumor spheroids for anticancer drug discovery." Biomed Microdevices 10(2): 197-202.

CHAPTER 4

MICROSCALE BUBBLE TRAP[3]

4.1 Introduction

Microfluidics is the technology of systems that process or manipulate small (10^{-9} to 10^{-18} liters) amount of fluids, using channels with dimensions of tens to hundreds of micrometers (Whitesides 2006). Advance in the microfluidics technology and has contributed to the development of a new research area known as 'lab-on-a-chip' (Dittrich and Manz 2006; Haeberle and Zengerle 2007). In particular, integration of the microfluidics technology and a cell culture technique has yielded a 'cells-on-a-chip', which can be exploited to answer biological questions that cannot be answered with conventional macroscale systems (Park and Shuler 2003; El-Ali et al. 2006). The advantages of microfluidic cell culture systems are many-fold. In addition to reduced sample consumption and an efficient heat and mass transfer, the small length scale creates laminar flow and a controlled gradient of chemicals (Keenan and Folch 2008). Moreover, the microscale length scale mimics that of biological systems, allowing researchers to create cellular environment mimicking physiological environment better than their macroscale counterparts (Bhadriraju and Chen 2002; Leclerc et al. 2004; Baudoin et al. 2007; Fisher and Peattie 2007).

The technique for culturing cells *in vitro* has been well established. However, culturing cells in a microfluidic system requires biocompatibility of materials, good sealing of a device, maintenance of sterility during cell culture, and prevention of bubble accumulation within the system. Several of these issues with microfluidic

[3] This chapter has been modified from an article, Sung, J. H. and M. L. Shuler (2009). "Prevention of air bubble formation in a microfluidic perfusion cell culture system using a microscale bubble trap." Biomed Microdevices 11(4): 731-8, with permission of Springer.

perfusion culture of mammalian cells have been discussed in detail (Kim et al. 2007). While some of these problems are manageable by careful selection of materials or protocols, bubble accumulation is an obstacle that is extremely difficult to avoid in a microfluidic system, particularly if fluid is recirculated through the device. Unlike macroscale systems, surface tension is often dominant at the microscale, causing air bubbles to stick easily to the inner surface. These air bubbles inside microscale systems are extremely difficult to remove. Occurrence of air bubbles not only obstructs the fluidic path and distorts the flow, but also can damage the cells at the liquid-gas interface. Any attempt to remove the bubbles by increasing the flow rate inside the system can also result in further damage to the cells due to shear. This issue is especially important in long-term microfluidic cell cultures, since small air bubbles tend to coalesce and accumulate.

The accumulation of air bubbles has been a constant problem in microfluidic systems, and several strategies have been developed to solve the problem. To avoid capturing bubbles in a microscale free-flow electrophoresis chip, a semi-impermeable membrane or arrays of bubble-blocking microchannels has been used to block entry of bubbles (Kohlheyer et al. 2008). Meng and his colleagues reported a degassing plate with hydrophobic bubble capture area which can be distributed across a microfluidic device at critical locations (Meng 2006). Yang et al. developed an ultrasonic micro-degassing device intended for used with portable dialysis system and evaluated the degassing process (Yang 2002). Although these novel strategies can remove bubbles in a microfluidic system, they are not always compatible with microfluidic cell culture systems which pose the additional requirement of maintaining cell viability. In addition, intricate modules may add complexity to the system which hinders consistent operation. One method is to integrate a bubble trap before the main system so that any fluid that goes into the main system is free of bubbles (Eddington 2006). Typically,

such bubble traps utilize the buoyancy of an air bubble, and capture bubbles by providing an area where bubbles can float and be separated from the flow. However, such a scheme depends on other parameters, such as the flow rate inside the device and the size of bubbles. In case of low Reynolds number fluid, the rising velocity of a spherically-shaped bubble is mainly determined by the drag and the buoyancy forces, and can be expressed by Stokes equation (Zheng and Yapa 2000),

$$v = \frac{g\Delta\rho d^2}{18\mu} \qquad (4.1)$$

where g is gravity acceleration, $\Delta\rho$ is the density difference between a bubble and ambient fluid, d is the diameter of a bubble, and μ is dynamic viscosity of ambient fluid. Since the rising velocity is proportional to the square of a diameter, it can be predicted from the equation that a smaller bubble will rise considerably slower than a bigger bubble. Depending on the flow rate and the dimension of a bubble trap, it is possible that a small bubble may still escape from the bubble trap and enter the cell culture area.

Recently, Kang et al reported a practical analysis model of air bubble elimination through a gas-permeable PDMS microfluidic channels (Kang et al. 2008). In this study the authors used a positive pressure to force out the bubbles, and cultured human breast cancer cells (MCF-7) in a microfluidic device for 5 days by periodically removing bubbles. However, the disadvantage of this system is that the medium supply has to be stopped and cells are exposed to a high pressure during the bubble removal process. Another example is an active bubble trap and debubbler which can trap and remove air bubbles maintaining continuous flow in the microfluidic device (Skelley and Voldman 2008). It utilizes a pneumatic valve-like geometry to trap bubbles and removes the trapped bubbles by applying vacuum. Using this device, they

were able to trap bubbles up to 25 µl and remove them in under 3 hours. However, this device requires an additional vacuum connection to work. Moreover, the bubbles were removed through a restricted area, resulting in a slow bubble removal rate (0.0023 µl/s), which means that if bubbles accumulate fast, it may eventually fill up the trap and invade cell culture area.

In this chapter, we report a microscale bubble trap which mechanically traps air bubbles while allowing fluidic paths to be unhindered. It consists of two-layer PDMS channel structure; larger top-layer channels provide the space for bubbles, and narrower bottom-layer channels provide alternative fluidic paths. Rather than relying solely on the buoyancy of air bubbles in liquid, it physically traps the bubbles within the structure of two-layer channels and the barrier. Barriers located in the middle of the bubble trap acts as a sieve that blocks bubbles larger than the channel size in the main system, offering controllability over the size of bubbles captured. We demonstrate the ability of the bubble trap to confine air bubbles within the device, and examine the pattern of the flow to verify that the presence of the bubble trap does not cause distortion of the flow. The bubble trap was able to trap bubbles up to 10 µl, and the trapped bubbles could be easily removed by degassing the device for 15 minutes, resulting in the bubble removal rate of 0.01 µl/s. We also demonstrate that the presence of a bubble trap enhances the operation of microfluidic cell culture by using a micro cell culture analog (µCCA).

4.2 Materials and Methods

4.2.1 Materials

PDMS monomer and curing agents Sylgard 184 was obtained from Dow Corning (Midland, MI), and Fluorescein was purchased from Sigma Aldrich (St. Louis,

MO). PharMed tubing with inside diameter of 0.25 mm (Cole Parmer, Vernon Hills, IL) was used to connect a bubble trap, a microfluidic device, and liquid reservoir. A peristaltic pump (Watson-Marlow, Wilminton, MA) was used to pump liquid into a bubble trap and a microfluidic device. Live/dead staining solution (calcein AM green and ethidium homodimer-1) was purchased from Invitrogen (Carlsbad, CA).

4.2.2 Design of a Bubble Trap

A bubble trap consists of a two-layer PDMS structure, as in Figure 4.1. The main function of the two-layer channels is to capture air bubbles while still allowing liquid flow. Because of the large surface area inside a microscale bubble trap, captured air bubbles fill the top channel but not the narrower bottom channels. Additional sieve-like barriers blocks further migration of trapped bubbles towards an outlet. The sizes of the sieve-like structures become smaller as they get closer to the outlet. The last sieve-like structure has the size of 100 μm, which is smaller than the narrowest channel in a main microfluidic device. Therefore, any air bubbles that are large enough to occlude the channels in the main microfluidic device will be trapped inside the bubble trap, whereas bubbles that were small enough to pass through the bubble trap will be able to pass through the main microfluidic device without being trapped. The device could be designed for trapping smaller bubbles (for example 10 μm), if smaller channels are in use.

Two different types of bubble traps were designed. In the first type, a bubble trap was built as an independent module and was connected to a main microfluidic device using tubes (Figure 4.2(a)). In the second type, a bubble trap was integrated into the main microfluidic device so that no external connection was necessary (integrated module, Figure 4.2(b)).

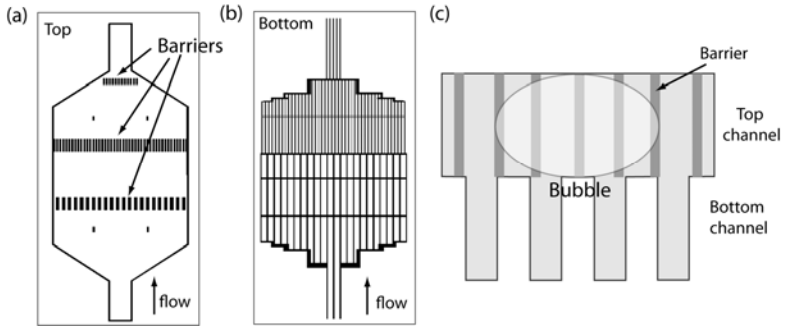

Figure 4.1 The schematic diagrams of design of a bubble trap

(a) Top-layer (b) Bottom-layer. (c) Cross-section view of a bubble trap. A top-layer contains barriers which block air bubbles from migrating further downstream. A bottom-layer contains alternative fluidic paths for liquid when air bubbles are captured in the-top layer.

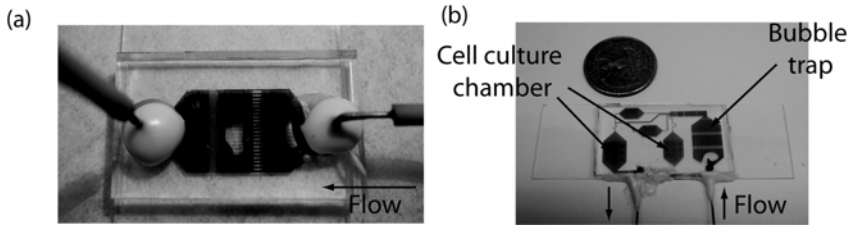

Figure 4.2 Pictures of a bubble trap

(a) An independent module bubble trap, which is connected to a μCCA (not shown in the picture) by additional tubing. (b) An integrated bubble trap. A bubble trap is integrated with a μCCA to eliminate the need of additional tubing. In each picture, a captured air bubble is seen inside the trap. The sizes of the bubble trap are the same in both modules.

4.2.3 Fabrication of a Bubble Trap

The design of a bubble trap was drawn using AutoCAD (Autoworks, San Rafael, CA), and the design was converted and exposed onto a Chrome-coated glass mask using GCA/MANN 3600F Optical Pattern Generator (Ultratech, San Jose, CA). Two separate masks were made for top and bottom layer with alignment marks. A SU-8 master for a bubble trap was fabricated on a 4 inch diameter silicon wafer. The first layer (wider channels) of 50 μm thickness was made by spin coating SU-8 50 (MicroChem, Newton, MA) at 2000 RPM for 30 seconds. After soft-baking at 65 ℃ for 6 minutes the temperature was raised to 95 ℃ and left for 20 minutes. The pattern on a first layer mask was exposed to SU-8 coated silicon wafer at 350 mJ/cm2 using EVG620 contact aligner (EV Group, Tempe, AZ). After exposure of the first layer, the second layer of SU-8 was spin coated at 2000 RPM to create a 50 μm thickness layer. The second layer was exposed at 350 mJ/cm2 after aligning the second layer mask with the exposed first layer using EVG620 contact aligner. Then post-exposure bake was done at 65 ℃ for 1 minute and 95 ℃ for 10 minutes, and the master was developed in a SU-8 developer solution for 6 minutes with agitation.

PDMS monomer and a curing agent were mixed in 10:1 ratio. After degassing to remove foams, the mixture was gently poured onto a SU-8 master. The PDMS was cured at 65 ℃ for 90 minutes and the PDMS structure was cut and peeled off from the master. A bubble trap and a 3x1 inch plain microscope glass slide (Fisher Scientific, Pittsburg, PA) were treated with air plasma cleaner (Harrick Plasma, Ithaca, NY) for 4 minutes and immediately bonded together for irreversible sealing. Inlet and outlet holes were punched with 23 gauge stainless steel needle and sealed with Torr Seal (Varian, Palo Alto, CA).

4.2.4 Bubble Trap Efficiency

The efficiency of bubble removal was tested (Figure 4.3(a)). The inlet of a bubble trap was connected to a reservoir containing water, and water was pumped through tubing and the bubble trap using a peristaltic pump. Bubbles were artificially generated in the reservoir by vigorous pipetting. The outlet of a bubble trap was connected to a waste reservoir where the liquid was collected. For easy visualization of the liquid and the bubbles, calligraphy color ink (blue and green, Winsor & Newton, Harrow, Middlesex, England) was used when photographs were taken.

It was tested whether the presence of captured air bubbles in the bubble trap causes alterations in the flow pattern. The liquid residence time in each chamber was measured by alternating the liquid source between water and fluorescein and tracking the interface. Measurements were initially taken without the presence of bubbles, and the same measurements were taken again after the bubble trap was partially filled with air bubbles. The comparison was made for both a separated bubble trap and an integrated bubble trap.

4.2.5 Finite-Element Simulation of Flow

The velocity profile inside a bubble trap was simulated by finite-element simulation using Comsol software (Comsol, Burlington, MA). The model was simplified to 2-dimensional structure. The Navier-Stokes equation was solved using the following set of parameters; density = $1x10^{3}$ kg/m^{3}, viscosity = $1x10^{-3}$ Pa·s, inlet velocity = $1x10^{-3}$ m/s.

4.2.6 Cell Culture Test Using Micro Cell Culture Analog (μCCA)

The human hepatoma cell line, HepG2/C3A, was cultured in a microfluidic device using an independent module bubble trap. The HepG2/C3A cell line was obtained from American Type Culture Collection (ATCC, Manassas, VA) and maintained in MEM medium (Invitrogen, Carlsbad, CA) with 10% FBS (Invitrogen) at 37℃ with 5% CO2. In this study, a micro cell culture analog (μCCA) was used as the main microfluidic cell culture device connected to a bubble trap. HepG2/C3A cells were cultured in a chamber of a μCCA connected to a bubble trap, and cell culture medium was recirculated through a bubble trap and a μCCA for 72 hours.

Cells were seeded and attached to the surface of chambers in a μCCA overnight. The next day, μCCA devices were assembled and connected with bubble traps. Before the assembly of a μCCA, tubes were thoroughly rinsed with ethanol to remove air bubbles within the tubes, followed by rinsing with sterile water to wash out ethanol. Devices were assembled, and the whole system was placed inside an incubator maintained at 37 ℃ with 5% CO_2. After 72 hours of cell culture in a μCCA, the reservoir was switched to a live/dead staining solution in DPBS (5μM calcein AM and 5μM ethidium homodimer-1, Invitrogen). The pictures were taken using a fluorescent microscope (Olympus, Tokyo, Japan).

4.3 Results and Discussion

4.3.1 Design and Fabrication of a Bubble Trap

Figure 4.1(a) shows the top-layer channel, which provides the space for trapping bubbles and also barriers to block further migration of the trapped bubbles. The gaps in the first line of barriers are 200 μm apart, and the size of the gaps becomes

smaller as they get closer to the outlet, down to 100 μm. It was designed so that any air bubbles with a diameter greater than 100 μm will be blocked by the barriers, since the narrowest channel in the main microfluidic system (μCCA) was 100 μm wide. Figure 4.1(b) shows the bottom-layer channels, which are narrower channels designed to be a by-pass in case the top-layer becomes occupied by bubbles. The bottom-layer channels are 30 μm to 50 μm wide, and both top and bottom-layers are 50 μm deep. The aspect ratio of the bottom channels ensures that the bubble that is trapped in the top space will not fill the bottom space completely, as illustrated in the schematic diagram of the cross sectional view of the bubble trap in Figure 4.1(c).

Figure 4.2 shows pictures of two different types of a bubble trap. Figure 4.2(a) shows an independent bubble trap module. In an experiment, the bubble trap would be connected before the main microfluidic device so that the flow will go through the bubble trap. An independent module requires additional connection between the bubble trap and the μCCA, which leaves the possibility of air bubbles entering at the interface between the device and tubing. To eliminate such a possibility, an integrated version of bubble trap was fabricated. In this design, an SU-8 master was made with a bubble trap integrated with a μCCA, and a PDMS structure from the master was bonded to a glass slide (Figure 4.2(b)). Such a design eliminates the requirement of additional connection and the possibility of bubbles originating from interfaces.

4.3.2 Trapping and Removal of Bubbles

The efficiency of bubble removal was tested using the bubble trap. Liquid was withdrawn from a source reservoir using a peristaltic pump, and passed through a bubble trap and collected in a collection reservoir. Air bubbles were artificially created in the source reservoir. In case a bubble trap was not used, air bubbles were withdrawn

into tubes and traveled to a collection reservoir. On the other hand, the presence of a bubble trap successfully prevented the migration of bubbles to the collection reservoir as seen in Figure 4.3, verifying that the bubble trap was efficiently trapping the bubbles. The bubbles in a trap still remained in place even after the flow rate was increased to ten-fold of normal operating rate to a value of 50 μl/min to increase the pressure. The location within the bubble trap where the bubble was captured was examined under a microscope, and it was verified that the bubble was trapped, with liquid flowing through the bottom-layer channels.

By measuring the time it takes to fill the bubble trap with air at a known volumetric pumping rate, it was observed that the bubble trap was able to capture bubbles of up to 10 μl volume, which is close to the calculated volume of the trap. The trapped air bubbles could be easily removed by degassing the trap with in-house vacuum line (relative pressure of negative 78 kPa) for 15 minutes. According to the analysis model of bubble elimination through a PDMS membrane, the bubble removal rate can be expressed as follows (Kang et al. 2008);

$$-\frac{dV}{dt} = \frac{PA(P_2 - P_1)}{b} \cdot \frac{T}{273} \cdot \frac{76}{P_{atm}} \tag{4.2}$$

where P is the permeability of PDMS (1.92x10-15 m2s-1Pa-1), p2-p1 is net pressure difference (-78 kPa), b is the membrane thickness (1 mm), A is the membrane area through which the bubble is removed (100 mm^2), T is temperature in Kelvin, and P_{atm} is the atmospheric pressure in cmHg. Using given parameters, the bubble removal rate in our device is predicted to be about 0.01 μl/s. Consistent with the calculation, when the trap was filled with bubbles and placed under vacuum, bubbles disappeared within 15 minutes of degassing. In the study by Skelley, they reported that the bubble

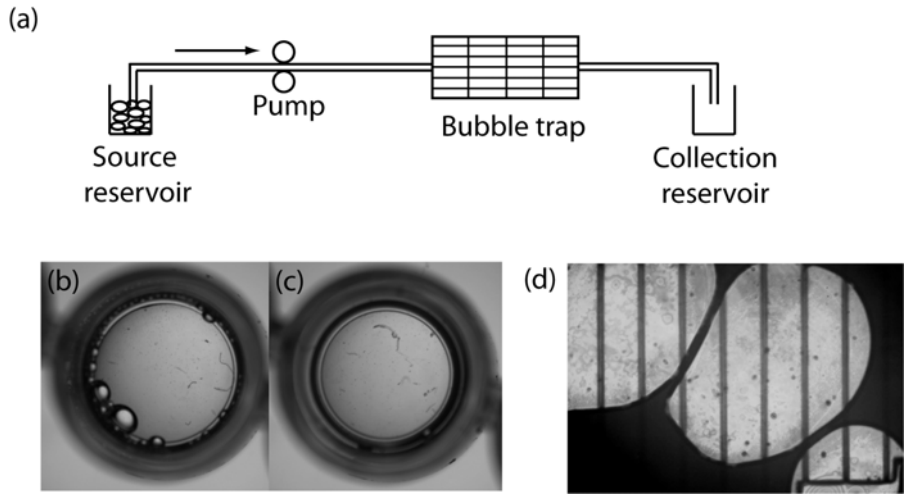

Figure 4.3 Testing bubble trap efficiency

(a) Testing the efficiency of bubble removal by an independent bubble trap module. Bubbles are artificially created in the source reservoir by pipetting, and water and bubbles were pumped into the collection reservoir. (b) Picture of the collection reservoir in the case where a bubble trap was not used. (c) Picture of the collection chamber where a bubble trap was used. The presence of a bubble trap prevented bubbles from travelling through the tubes and reaching the collection reservoir. (d) A picture of bubbles trapped in a bubble trap. Narrow bottom channels can be seen where liquid is flowing underneath the bubbles. Color ink was used to visualize the channels.

removal times were proportional to the bubble volumes, because the bubble was exposed to vacuum in a restricted area only, giving a constant bubble removal rate. In our device, the exposed area is proportional to the bubble volume. Therefore, the bubble removal rate is proportional to the bubble volume, resulting in a constant bubble removal time regardless of the bubble volume. The short bubble removal time (~15 minutes) allows temporarily detaching the bubble trap from the main μCCA device and removing the bubbles, without compromising the viability of cultured cells.

4.3.3 Microfluidic Cell Culture Test

The function of a bubble trap is to prevent the formation of bubbles in a microfluidic system, therefore it must not distort the flow going into the main microfluidic system. The potential distortion of the flow inside the bubble trap was tested by mathematical simulation and experiment. The simulation results of the flow inside a bubble trap and the exit channel with or without a bubble are shown in Figure 4.4. The results show that even though the presence of a bubble results in temporary distortion of the velocity profile inside the bubble trap, the profile returns to the original parabolic profile after going through the exit channel. The velocity profiles across the exit channel did not show differences in both cases (Figure 4.4(c) and (d)).

To verify this simulation result experimentally, the flow rate in each chamber in a μCCA was measured. The μCCA consists of microfluidic network, and the geometry of the circuit was calculated and designed so that each chamber would have specific liquid residence times. The liquid residence time is a critical parameter in a μCCA in that it controls the extent of reaction in a chamber. The liquid residence time in each chamber is designed to be similar to the residence time of blood flow in the corresponding organ in human body. By comparing the residence times in each

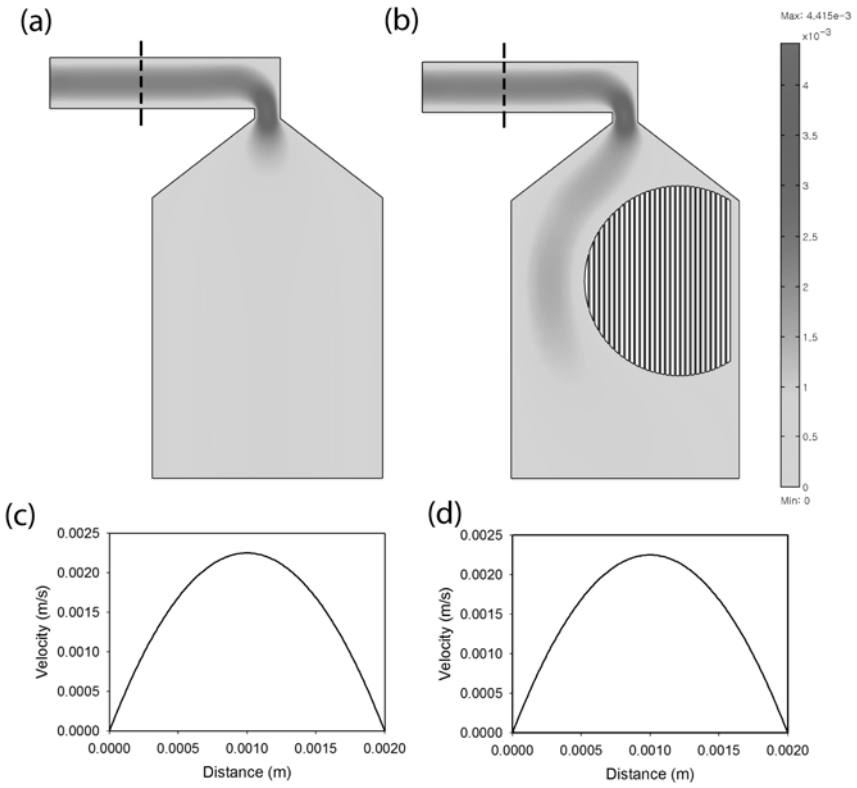

Figure 4.4 Finite-element simulation of the flow inside a bubble trap.

(a) Without bubbles inside, a parabolic velocity profile is maintained. (b) With a bubble trapped inside, the velocity profile is disrupted but restored to the original parabolic profile after going through the exit. (c) Velocity profile of the flow in the exit conduit without a bubble in the trap. (d) Velocity profile of the flow in the exit conduit with a bubble trapped. The location where the cross-sectional velocity profile was taken from is marked by a dashed line.

Table 4.1 Residence times of flow in each chamber in a microfluidic device attached after a separate bubble trap module.

Chamber	With bubble	Without bubble
1	67.3±2.5	67.7±2.5
2	69.0±3.6	66.0±4.3
3	48.0±2.0	47.3±3.1
4	132.7±1.1	132.3±9.7

Table 4.2 Residence times of flow in each chamber in a microfluidic device with integrated bubble trap.

Chamber	With bubble	Without bubble
1	85.3±2.5	79.7±4.51
2	68.7±2.3	66.3±1.5
3	83.0±6.1	82.0±7.6
4	166.0±5.3	175.3±6.8

chamber of a μCCA with and without bubbles in a bubble trap, we could test if the presence of bubbles causes any distortion in the flow pattern. Table 4.1 summarizes the measured residence times in each chamber. The result verifies that an independent bubble trap module does not change the residence times even when the bubble trap was occupied with bubbles. In case of an integrated bubble trap, the presence of bubbles caused small amount of deviations in the flow residence times, but the deviation was less than 10% in all cases (Table 4.2). We speculate that the independent bubble trap was more robust from alterations in the flow pattern since the tubing connection from a bubble trap and a μCCA was several centimeters in length providing enough distance for complete re-mixing, whereas in case of an integrated bubble trap the distance between the bubble trap and a μCCA is millimeter range. However, in both cases, a consistent flow pattern was established after passing through the bubble trap to ensure robust flow pattern in a μCCA.

In general, formation of air bubbles in a microfluidic system during long-term perfusion cell culture can originate from two main sources; residual air bubbles that were present in the system due to incomplete priming (Kim et al. 2007), or formation air bubbles at the sites with incomplete sealing, such as the connections between a device and tubes (Christensen 2005). From our experience, priming the system with liquid with lower surface tension and better wettability than water such as ethanol before the experiment considerably decreased the chance of air bubble formation. In addition, care was taken to make sure the connections at the end of tubes were tight to minimize the chance of air entering through a loose connection. Even after such precautionary steps, without the presence of a bubble trap, it was difficult to completely avoid formation of air bubbles during long-term (> 24 hours) operation of microfluidic cell culture system with medium recirculation, which eventually led to

the failure of system. Medium recirculation is a particularly stringent test since small bubbles are retained in the system and can eventually coalesce.

The use of a bubble trap in a microfluidic cell culture system was tested to examine the long-term efficiency of bubble removal and cell-compatibility. An independent bubble trap module was connected to the front end of a μCCA, as shown in Figure 4.5(a). The μCCA system was operated with medium recirculation in a cell culture incubator for 72 hours. After 72 hours of medium recirculation, the viability of cells inside a μCCA was assessed by live/dead staining. The bubble traps at the front end of μCCA devices considerably decreased the air bubble formation during the 72-hour period. In an experiment where half of the μCCA devices were connected directly to the medium reservoir without bubble traps and the other half was connected with bubble traps, μCCA devices with bubble traps had significantly fewer air bubbles in the culture chambers than the μCCA devices without bubble traps. Although it was difficult to quantitatively compare the amount of captured air bubbles in the system, this result verifies that the bubble trap efficiently removes air bubbles in a long-term experiment. Figure 4.5(b) shows typical fluorescent images of cells in a μCCA after the operation. The majority of cells are viable, with less than 10% of cells stained dead. This picture also verifies that the bubble trap is cell culture compatible. Although the pictures in Figure 4.5(b) are three-day results, in general it was possible to operate the device with a bubble trap for up to four days. After four days the waste accumulation and nutrient depletion in the recirculating medium prevented further experiment. However, the bubble trap was still functioning after four days and it was possible to continue using it. The limit was on cell viability due to recirculation of medium without addition of fresh medium, and not on the bubble removal process.

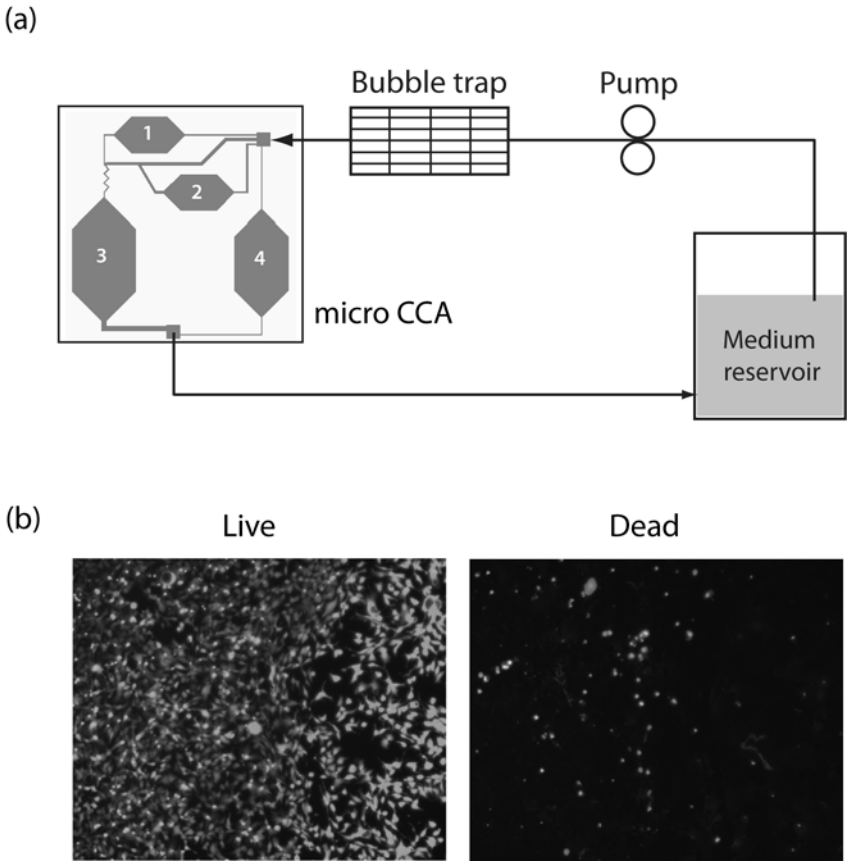

Figure 4.5 Cell culture compatibility of a bubble trap

(a) Schematic diagram of setup for microfluidic perfusion cell culture system. Medium is pumped from a reservoir into a bubble trap, and into a μCCA, which is a main microfluidic cell culture device. After circulating through the chambers, medium flows back into the reservoir for recirculation. (b) Live/dead staining results of HepG2/C3A cells in a μCCA device connected to a bubble trap after 72 hours of operation with medium recirculation. Live cells were stained with calceinAM and dead cells were stained by ethidium homodimer-1.

4.4. Conclusion

A bubble trap with two-layer PDMS structure was designed and fabricated using soft lithography technique. The two-layer structure with barriers physically traps air bubbles rather than relying solely on the buoyancy of air bubbles, while allowing fluidic paths to remain connected. The fabricated bubble trap was able to remove air bubbles efficiently to enable successful culture of HepG2/C3A cells in a microfluidic device with medium recirculation for three days. The proposed device may work as an independent or integrated module for microfluidic cell culture systems.

REFERENCES

Baudoin, R., et al. (2007). "Trends in the development of microfluidic cell biochips for in vitro hepatotoxicity." Toxicol In Vitro 21(4): 535-44.

Bhadriraju, K. and C. S. Chen (2002). "Engineering cellular microenvironments to improve cell-based drug testing." Drug Discov Today 7(11): 612-20.

Christensen, A. M., Change-Yen, D., Gale, B.K. (2005). "Characterization of interconnects used in PDMS microfluidic systems." J Micromech Microeng 15: 928-934.

Dittrich, P. S. and A. Manz (2006). "Lab-on-a-chip: microfluidics in drug discovery." Nat Rev Drug Discov 5(3): 210-8.

Eddington, D. (2006) "Chips & Tips: In-line microfluidic bubble trap." Lab Chip

El-Ali, J., et al. (2006). "Cells on chips." Nature 442(7101): 403-11.

Fisher, R. J. and R. A. Peattie (2007). "Controlling tissue microenvironments: biomimetics, transport phenomena, and reacting systems." Adv Biochem Eng Biotechnol 103: 1-73.

Haeberle, S. and R. Zengerle (2007). "Microfluidic platforms for lab-on-a-chip applications." Lab Chip 7(9): 1094-110.

Kang, J. H., et al. (2008). "Analysis of pressure-driven air bubble elimination in a microfluidic device." Lab Chip 8(1): 176-8.

Keenan, T. M. and A. Folch (2008). "Biomolecular gradients in cell culture systems." Lab Chip 8(1): 34-57.

Kim, L., et al. (2007). "A practical guide to microfluidic perfusion culture of adherent mammalian cells." Lab Chip 7(6): 681-94.

Kohlheyer, D., et al. (2008). "Bubble-free operation of a microfluidic free-flow electrophoresis chip with integrated Pt electrodes." Anal Chem 80(11): 4111-8.

Leclerc, E., et al. (2004). "Microfluidic PDMS (polydimethylsiloxane) bioreactor for large-scale culture of hepatocytes." Biotechnol Prog 20(3): 750-755.

Meng, D. D., Kim, J., Kim, C. (2006). "A degassing plate with hydrophobic bubble capture and distributed venting for microfluidic devices." J Micromech Microeng 16: 419-424.

Park, T. H. and M. L. Shuler (2003). "Integration of cell culture and microfabrication technology." Biotechnol Prog 19(2): 243-53.

Sin, A., et al. (2004). "The design and fabrication of three-chamber microscale cell culture analog devices with integrated dissolved oxygen sensors." Biotechnol Prog 20(1): 338-45.

Skelley, A. M. and J. Voldman (2008). "An active bubble trap and debubbler for microfluidic systems." Lab Chip 8(10): 1733-7.

Whitesides, G. M. (2006). "The origins and the future of microfluidics." Nature 442(7101): 368-73.

Yang, Z., Matsumoto, S., Maeda, R. (2002). "A prototype of ultrasonic micro-degassing device for portable dialysis system." Sens Actuators A Phys 95: 274-280.
Zheng, L. and P. D. Yapa (2000). "Buoyant velocity of spherical and nonspherical bubbles/droplets." Journal of Hydraulic Engineering-Asce 126(11): 852-854.

CHAPTER 5

IN SITU FLUORESCENCE OPTICAL DETECTION SYSTEM FOR INTEGRATION WITH μCCA FOR REAL-TIME ANALYSIS[4]

5.1 Introduction

Microfluidic perfusion cell culture systems can serve as biological models to study complex biological processes with a precise control over cellular microenvironment (Pihl et al. 2005; Sivaraman et al. 2005; Cheng et al. 2007; Kim et al. 2007). One disadvantage of microfluidic systems is that the analysis and detection of physiological functions is difficult due to their closed and miniaturized nature. Therefore, the development of a non-invasive analytical technique for use in microfluidic cell culture devices is crucial. Fluorescence detection is a popular method for non-invasive detection of cellular response. Fluorescent probes have been used for detecting cell viability, oxygen concentration, protein expression, and metabolic activity (Bambot et al. 1994; Giepmans et al. 2006). For example, drug metabolism is often assessed by cytochrome P450 enzyme activity, by incubating cells with a fluorogenic substrate, which yields fluorescent product upon enzyme reaction (Donato et al. 2004). Typically, these products are analyzed with a fluorescent microscope, or a fluorescent plate reader for high-throughput measurement, but they are not optimized for microfluidic perfusion cell culture systems. One issue is that mammalian cell culture requires temperature and CO_2 control, which interferes with real-time detection. The tubes and fluidic connections associated with microfluidic devices would have to

[4] This chapter has been modified from following articles. Oh, T. I., et al. (2007). "Real-time fluorescence detection of multiple microscale cell culture analog devices in situ." Cytometry A 71(10): 857-65, and Sung, J. H., et al. (2009). "Fluorescence optical detection in situ for real-time monitoring of cytochrome P450 enzymatic activity of liver cells in multiple microfluidic devices." Biotechnol Bioeng (accepted), with permission of Wiley Interscience.

be disconnected for measurements in a fluorescent plate reader, which not only interferes with continuous operation of microfluidic devices, but also raises the possibility of bacterial contamination and introduction of air bubbles.

Obtaining real-time data from an operating microfluidic device, i.e., simultaneous fluidic perfusion and detection, is important because it allows easier extraction of information. For instance, enzyme kinetic parameters can be more easily and reliably extracted from real-time data than end-point measurements. Since the miniaturized and closed nature of microfluidic systems makes real-time analysis difficult, the systems are generally analyzed by end-point measurements, i.e., by collecting data of perfused medium or the cells after an experiment (Sivaraman et al. 2005). If a microfluidic system does not require a cell culture, it is relatively easier to operate the device under a microscope for real-time investigation. However, if cells are cultured inside the device, real-time investigation becomes even more challenging. For example, Garcia et al. utilized laminar flow in a microfluidic channel to generate a concentration gradient of inhibitor molecules and studied the enzyme inhibition kinetics in a high-throughput manner (Garcia et al. 2007). Since immobilized enzymes were used in this study, they were able to use an epifluorescence microscope for monitoring the fluorescence in the system. If a similar study were to be done using a microfluidic cell culture system, it would have been difficult to obtain real-time data using a microscope without the use of expensive and specialized incubator stages. One approach to this problem was suggested by Yu et al., who developed a plate-reader compatible microchannel array that can be readily integrated and operated with a conventional fluorescence plate reader (Yu et al. 2007). Although this system allows easy integration with a plate reader, its utilization is limited since it did not involve simultaneous fluidic perfusion and detection.

There have been research efforts towards the development of an integrated optical detection system for microfluidic systems. Novak et al. reported an integrated fluorescence detection system for lab-on-a-chip applications, inspired by mass-produced optical systems such as DVD, consisting of a blue LED for excitation and a photodiode for detection (Novak et al. 2007). However, the reported optical system was a single channel system, and consequently does not support an automated multichannel measurement for high-throughput analysis. Also the authors did not show that the system was compatible with cell culture, which typically requires more stringent operating conditions.

In this chapter, we use an *in situ* fluorescence optical detection system (ISFODS), which is designed for detection of fluorescent signal in a micro cell culture analog (μCCA). The system employs a minimal number of optical components to reduce artifacts associated with imaging aberration. The compact design allows the whole system to be placed inside a cell culture incubator with the microfluidic device including a pump. We use this system for two main purposes; real-time detection of cell viability during toxin application, and real-time measurement of enzymatic activity of hepatoma cell line in a microfluidic. In the first study, to measure cell viability, an imaging detector array is used to capture the image of live cells inside the device. Using this setup, we were able to monitor the acute cell-killing effect of ethanol, and also monitor the long-term growth of cells in the device for 85 hours. For the second study a single photodetector is used for easier quantification of fluorescent signal directly from the cell culture medium in the device. The system was used to monitor, in real-time, the P450 1A1/1A2 enzyme activity of liver cells. The P450 enzymes are a major enzyme family in liver metabolism, and fluorescence-producing substrates are known for various isoforms of P450 enzyme family (Stresser et al. 2002; Donato et al. 2004). The ethoxyresorufin-O-dealkylase (EROD) fluorescence assay,

which measures the conversion of ethoxyresorufin to a fluorescent product resorufin, has been widely used for quantification of both P450 1A1 and 1A2 enzyme activity of liver cell line (Donato et al. 1993; Kelly and Sussman 2000; Coward et al. 2005; Camp and Capitano 2007). A mathematical model was developed to characterize the enzymatic reaction and the transport of substrate and fluorescent product, which was then compared to experimental data for improved quantification and extraction of reaction associated parameters.

5.2 Materials and Methods

5.2.1 Cell Culture and Chemicals

The cell lines used in this study (HepG2/C3A and MES-SA) were obtained from ATCC (American Type Culture Collection, Manassas, VA). All cell lines were cultured in the media recommended by ATCC, with 10% FBS (Invitrogen, Carlsbad, CA). Media used for culture the cell lines were MEM and McCoy's 5a medium from Sigma Aldrich (St Louis, MO). CalceinAM and cell tracker green were purchased from Invitrogen, and ethanol was purchased from Sigma Aldrich. MES-SA cell line has been transfected to express the fusion protein H2B-GFP, which is a human histone protein fused at the amino terminus to EGFP. The viability of a cell can be determined by measuring the fluorescence intensity of the cell.

5.2.2 ISFODS for Cell Viability Measurement

The optical system, is shown in Figure 5.1 and employs a high-power light emitting diode (LED) and a charge coupled device (CCD) camera, respectively, as a light source and a detector. The overall imaging system is designed to offer low

magnification (M ~ 5.8) in order to provide cell status information on the basis of statistical average by imaging a large number of cells simultaneously. Light from a high power royal blue LED (Luxeon LXHL-BR02, Philips, San Jose, CA, U.S.A.) of peak wavelength at λ = 455 nm (manufacturer provided) and optical power at 220 mW lumens is focused by an imaging lens L1 (f = 35 mm, d = 24.5 mm) to excite EGFP on μCCA samples. Excited fluorescence is imaged by L1, occasionally relayed by L2 (f = 150 mm, d = 50 mm), to a CCD (QICAM FAST 1394, Qimaging, Burnaby, BC, Canada). A pinhole aperture is placed for baffling out the noise from background. The center wavelength / band width of the excitation filter (F1) and emission filter (F2) in a fluorescence filter cube (31054GFP, Chroma Technology, Rockingham, VT, U.S.A.) is respectively given by 455 nm / 70 nm and 525 nm / 30 nm (provided by the manufacturer). The effect of non-collimation through F2 is minimal because the sample-to-L1 distance is close to the focal length of L1 and thus the image distance from L1 is large relative to the overall size of the system. Two μCCA chips were mounted on a motorized stage (UTM100CC1DD, Newport, Irvine, CA, U.S.A.) with a linear resolution of 1 μm. The total dimension of the optical system is 30(L) x 23(W) x 20(H) cm3. Potentially, the system can be made more compact to accommodate more μCCA chips.

The light source spectra have been measured by an optical spectrometer. Maximum power has been measured at λ = 459.5 nm with the full width-half maximum as 25 nm. Thus, slight discrepancy exists between measured and manufacturer provided peak wavelengths. The cutoff wavelength, defined as the wavelength at which the optical power is reduced to 1% of the maximum is 524 nm without using F1. This overlaps the emission spectrum of EGFP signal. When the excitation filter F1 is mounted on the LED, the cutoff wavelength is decreased to 498 nm, which removes the source interference due to excitation of EGFP. Using

programmed control, μCCA samples have been exposed minimally at 0.7~5 seconds for each measurement to protect cells from getting photobleached. Since a CCD is inherently afflicted with dark current noise, thermal noise characterization is required at an incubating temperature 37.5°C. From an initial test of a CCD, the dark current noise has been determined to be saturated at a constant level 25 minutes after the system was installed in an incubator. The maximum change in the dark current noise is a 10% increase, compared to that of room temperature. Experimental measurements were initiated at least 30 minutes after a CCD was turned on. The transition between chambers has been made mechanically. The transition time has been controlled to be short for minimal disparity between measurement conditions and yet sufficiently long to take observable time not to affect the drug diffusion process in μCCA. Registration error of the motorized stage was less than 1 μm, which is far smaller than the cell size. Thus, misregistration in the images taken at different time points was minimal.

The μCCA used in this study is shown in Figure 5.2(a). The liver hepatoma cell-line HepG2-C3A was seeded on the liver chamber (A) and a uterine cancer cell line, MESSA H2B-GFP was seeded on the uterus cancer chamber (B). The normal colon cell chamber (C) and colon tumor cell chamber (D) were not used in this study. For cell seeding, the chips were immersed in piranha solution for 20 minutes to remove organic residues, and autoclaved for sterilization. Then the chips were coated with 0.1 mg/ml poly-D-lysine (Sigma-Aldrich, St. Louis, MO, U. S. A.), followed by washing with PBS and coating with 50 μg/ml fibronectin (Chemicon International, Temecula, CA, U. S. A.). Cells were trypsinized and resuspended in medium to the final concentration of 7.5 x 105 cells/ml. An appropriate volume of cell suspension (20 μl ~ 50 μl) was placed on each chamber to completely cover the chamber without spilling over. Chips loaded with cells were incubated at 37.5°C with 5% CO_2 overnight.

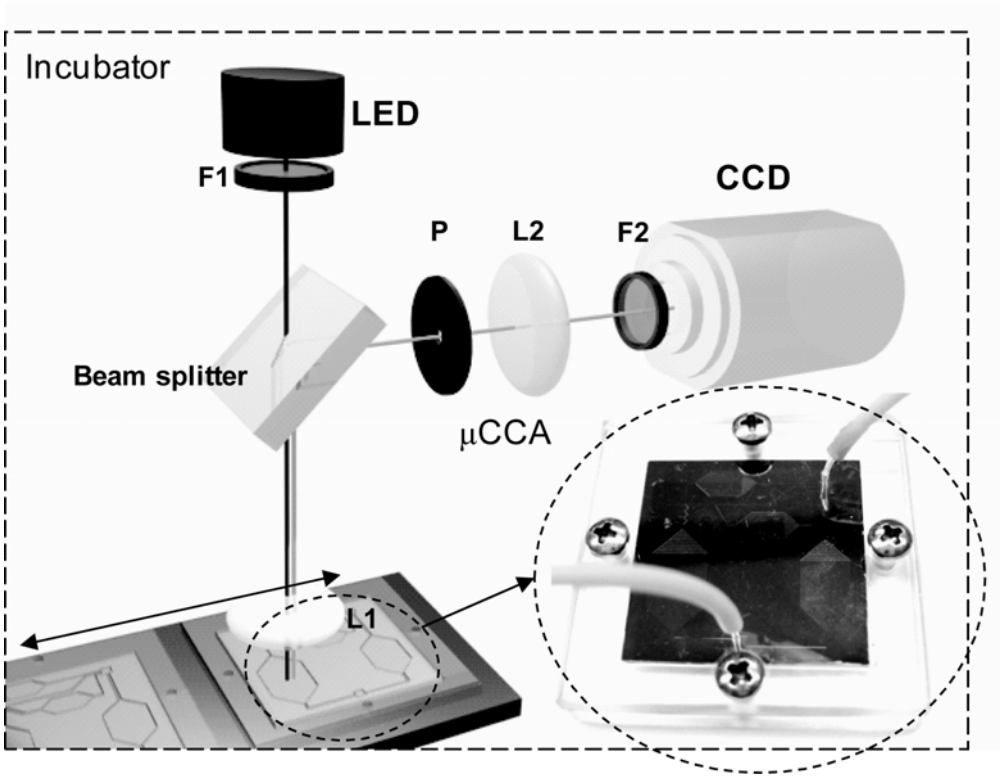

Figure 5.1 Overview of ISFODS for cell viability measurement

The black and gray solid lines represent an illuminating and emitted beam, respectively. The rectangle with dotted line represents the incubator, and inside the dotted circle is shown a μCCA. (F1: excitation filter, F2: emission filter, L1, imaging lens, L2: relay lens, P: pin-hole, and BS: beam splitter).

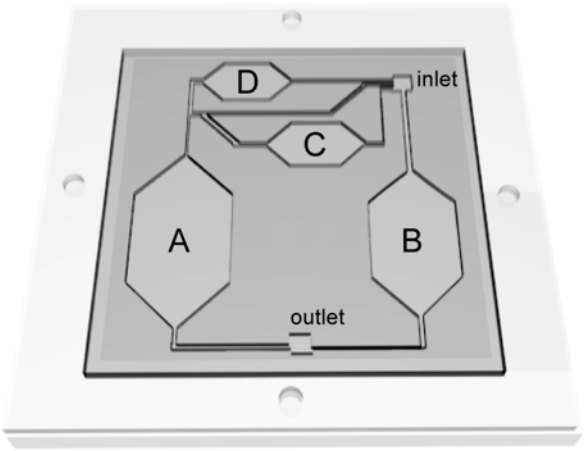

Figure 5.2 A μCCA used with ISFODS for cell viability measurement.

In case it was necessary, the whole chip was stained with calceinAM in order to distinguish live cells. Before assembling the CCA device, whole chip was immersed in 2μM calceinAM solution for 30 minutes. Then the chips were assembled and sealed with a PMMA holder. Silicone tubes (PharMed Pump Tubing, inside diameter = 0.25 mm, Cole-Parmer, IL, U.S.A.) were used to connect the assembled CCA with a medium reservoir. A peristaltic pump was used to supply the medium at a constant speed (0.5 RPM equivalent to 2 μl/min approximately).

5.2.3 Ethanol Toxicity Experiment

In order to verify that the optical system is able to detect the process of cell death in real-time, the cells in the CCA device were treated with various concentrations of ethanol. For this experiment, the cells on the chips were stained with calceinAM prior to the assembly of the CCA device. After setting up the CCA device and the optical system, initial measurements were made for 20 minutes while supplying media with a peristaltic pump, in order to ensure that the cells were being monitored consistently. After 20 minutes have passed, various concentrations of ethanol (0%~20% v/v) in MEM media were flown into the system to induce a rapid cell death. The measurements were continued until there were no live cells detected, which took up to 120 minutes depending on the concentration of ethanol.

5.2.4 Cell Growth Monitoring

The long-term growth of cells in the CCA device was monitored with the optical system in order to verify that the system can be operated for several days while making real-time measurements. For the long-term growth study, MES-SA and

HepG2/C3A cell line transfected with H2B-GFP gene were used. Cells transfected with H2B-GFP express GFP protein constitutively, thus giving off green fluorescent signal as long as they are healthy. The CCA chips loaded with both cells lines were assembled and the whole optical system with the CCA device and a peristaltic pump were put in an incubator which was kept at 37℃, 5% CO2. For the long-term growth experiment, the CCA device was connected to a medium reservoir via silicone tubes, and the media coming out of the CCA device were fed back into the medium reservoir, therefore the media were being recirculated into the system for the whole time. The volume of the medium reservoir was 200 μL, which supports the growth of cells for about three days, and the measurements were made for 90 hours until the nutrients in the media became depleted and the accumulation of toxic wastes by cells eventually caused the cells to die.

5.2.5 Image Processing

Intensity graphs have been produced from acquired fluorescent images using Cell Profiler® after several steps of removing the effect of background noise. The steps involve cropping, illumination correction, and cell-number counting. In general, image processing based on cell numbers, occupied areas of cells, and the image intensity provided consistent results.

5.2.6 ISFODS for Metabolic Activity Measurement

The ISFODS was constructed with discrete optical components for optimum optical performance and ease of assembly (Figure 5.3(a)). The light from a green LED (Luxeon LXHL-MM1D, Philips, San Jose, CA) with peak wavelength at λ = 530 nm

and luminous flux at 53 lumens (typical, manufacturer provided) passes through a 50/50 dichroic beam splitter and is collimated by a lens (f = 35 mm, = 25.4 mm) to excite resorufin in the detection chamber. Fluorescence emission from resorufin is focused by a lens and detected by a low-power photodiode (818-UV, Newport, Irvine, CA). The system employs a filter set that consists of fluorescence excitation and emission filters. The center wavelength/bandwidth of the excitation and emission filter is 535/40 nm and 630/60 nm, respectively (Model #: D535/40m and D630/60m, Chroma Technology, Rockingham, VT). This filter set has a cutoff wavelength at 570 nm; therefore, it can discriminate fluorescence emission of resorufin from the source light. For detection at multiple locations, a transition between detection chambers was made by a motorized stage (UTM100CC1DD, Newport, Irvine, CA) with a linear resolution of 1 μm (manufacturer provided). The data acquisition and linear translation between chambers were all controlled by LABVIEW (National Instrument, Austin, TX). The ISFODS was operated in a working condition inside a cell culture incubator (water-jacketed incubator, model 3187, Forma Scientific, Marietta, OH) with 5% CO2, 37ºC temperature, and humidity control. The overall dimension of the entire set-up is approximately 30 cm (L) x 20 cm (W) x 20 cm (H), excluding an external personal computer.

For cell culture in a μCCA, we followed the previous methods, with some modifications to culture cells in 3-D matrix of hydrogel (Sung and Shuler 2009). In short, the surface of a μCCA was filled with medium (MEM, Invitrogen, Carlsbad, CA). After sealing, the μCCA was kept in a refrigerator at 4ºC. HepG2/C3A cells were trypsinized and an appropriate number of cells was resuspended in 100 μL of Matrigel^{TM} (BD Biosciences, San Jose, CA) to the final concentration of 1.5 x 107 cells/mL, unless specified otherwise. The cell mixture was kept in an ice bath to prevent polymerization. Approximately 6 μL of the cell suspension in Matrigel^{TM} was

withdrawn using a gel loading tip (VWR, West Chester, PA), and was slowly introduced into the liver chamber of the μCCA device. The number of cells introduced into a chamber was approximately 100,000 cells. After the cell loading, the μCCA device was placed in a cell culture incubator at 37ºC to initiate gel formation.

A detection chamber was made from an 8-well strip plate (VWR). After separating a single well, holes punched using a sharp needle heated with a flame at two opposite locations on both sides of the well. As seen in Figure 5.3(b), the location of the inlet/outlet holes allows the medium to flow into the detection chamber at bottom, fill up the chamber and flow out through the top. The total volume of the medium in the detection chamber is always kept constant at 300 μL. Therefore, any change in the fluorescence signal from the detection chamber reflects a change in the concentration of fluorescent molecules. A 23-gauge stainless steel needle was inserted into the holes and fixed with epoxy glue (Epotek 301, Epoxy Technology, Billerica, MA). It should be noted that the custom-made detection chamber has the same geometry and dimensions as the individual well of a 96-well microtiter plate, preventing any potential differences caused by differences in the detection environment when compared to a commercial fluorescence plate reader using a 96-well microtiter plate. 3 mL BD syringes (Fisher Scientific, Pittsburg, PA) and the custom-made detection chambers were filled with medium containing 1 μM or 10 μM ethoxyresorufin (Sigma, St. Louis, MO). The syringes, μCCA chips, and detection chambers were connected using Teflon tubing (1/16 inch inside diameter, Small Parts Inc., Miramar, FL). For detection at multiple locations during an experiment using the ISFODS, several sets of a syringe, a μCCA, and a detection chamber were prepared in the same way, as can be seen in Figure 5.3(a). The syringes were installed on a syringe pump (World Precision Instruments, Sarasota, FL), which were used to provide a flow

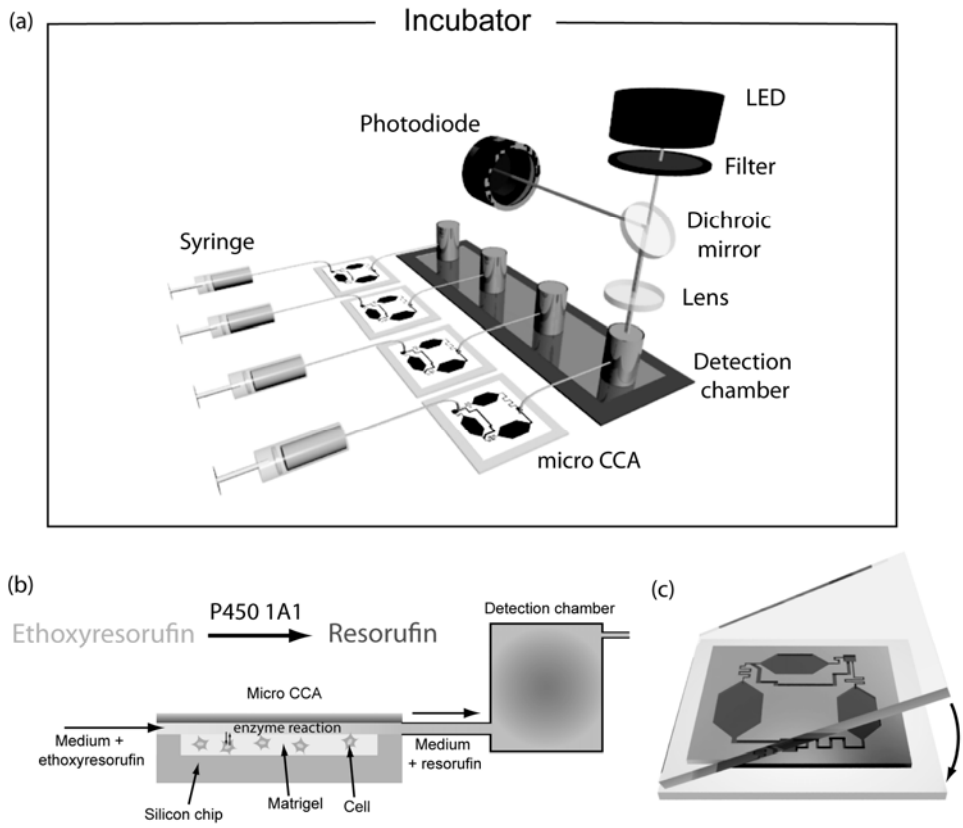

Figure 5.3 *In situ* fluorescence optical detection system (ISFODS) for enzyme activity measurement.

(a) Overall schematics of ISFODS (b) A cross-sectional view of a μCCA, with cell-embedded Matrigel^{TM}. (c) A schematic diagram of a μCCA device assembled with top and bottom frames. A μCCA consists of a liver, tumor and marrow chamber (Sung and Shuler 2009). In this study only liver chamber was used and the other two chambers were left empty.

at 2 μL/min. The fluorescent intensity in the detection chamber was measured every five minutes for three hours.

Additionally, two different conditions for the cells, uninduced and chemically induced by 3-Methyl Cholanthrene (3-MC), were tested. 3-MC is known to induce P450 genes by binding to ligand-binding nuclear receptor AHR (Sivaraman et al. 2005). Uninduced cells were taken directly from cultured cells and used for experiment. In the case of chemical induction, cells were incubated in a 96-well plate in culture medium containing 5 μM 3-MC. After 48 hours of incubation, cells were trypsinized and inserted into a μCCA for experiment.

5.2.7 Linearity Calibration of Fluorescence Intensity

The performance of the ISFODS on μCCA chips was calibrated with that of a commercial fluorescence plate reader (Molecular Devices, Sunnyvale, CA) in 96-well plates in response to various concentrations of resorufin solution in medium. Resorufin solutions in MEM medium were prepared in concentrations ranging from 50 nM to 10 μM.

5.2.8 96-well Plate Experiment for Cell Metabolic Activity Measurement

96-well experiments were performed as a control modality in contrast to μCCA. HepG2/C3A cells were initially trypsinized and suspended in MEM medium, and seeded in the wells of Corning 96-well plate (Fisher Scientific, Pittsburg, PA) at the final concentration of 100,000 cells per well. The medium in the wells were replaced with pre-warmed medium containing 10 μM ethoxyresorufin and the 96-well plate was incubated at 37ºC with 5% CO_2 for 3 hours. The enzymatic conversion of

ethoxyresorufin to resorufin was monitored using a fluorescent plate reader for 3 hours at the excitation wavelength of 544 nm and emission wavelength of 590 nm. For chemical induction of the cells, cells were cultured and pre-treated with 3-MC for 48 hours prior to experiment. After 48 hour incubation, cells were trypsinized, suspended in Matrigel™ solution, and cell-Matrigel™ mixture was pipetted into the wells. After incubation for 15 minutes at 37ºC, 300 µL medium with ethoxyresorufin was added to each well. After P450 1A1/1A2 activity was assessed, the protein content in each well was assessed by using Bradford method (Sigma Aldrich, St. Louis, MO) to normalize the enzyme activity on the per-mg-protein basis. In case of cells cultured in a µCCA, it was difficult to recover the intact cells and measure the protein content inside the microfluidic device. Therefore the total enzyme activity was compared, while the total cell number was kept the same in both µCCA and 96-wells.

5.2.9 Mathematical Simulation

A two-compartment mathematical model was set up to interpret the results obtained by µCCA integrated with the ISFODS (Figure 5.4(a)). The first compartment represents the liver cell chamber in a µCCA, and the second compartment represents the detection chamber. If both compartments are well-mixed, the concentration of the product resorufin is described by the following set of equations,

$$\frac{\mathrm{d}C_{CCA}}{\mathrm{d}t} = \frac{V_m \cdot C}{K_m + C} - \frac{Q \cdot C_{CCA}}{V_{CCA}} \tag{5.1}$$

$$\frac{dC_d}{dt} = \frac{Q \cdot C_{CCA}}{V_{CCA}} - \frac{Q \cdot C_d}{V_d} \tag{5.2}$$

where CCCA and Cd represent the concentration of resorufin in a µCCA and in a detection chamber, respectively. Q denotes the flow rate in and out of the chamber.

V_{CCA} and V_d are the volume of a μCCA and a detection chamber, respectively. V_m is a maximum reaction rate and Km a Michaelis-Menten constant. Equations 5.1 and 5.2 were solved by using the ode45 routine in MATLAB (Mathworks, Natick, MA).

Since the well-mixed model does not account for the transport phenomenon, a more detailed convection-diffusion model was constructed (Figure 5.4(b)). The flow inside a microfluidic system is governed by the Navier-Stokes equation, and the diffusion of molecules is described by a mass balance equation as follows:

$$\rho\vec{u}\cdot\nabla\vec{u} = -\nabla P + \mu\nabla^2\vec{u} \quad (5.3)$$

$$\frac{\partial C}{\partial t} + \vec{u}\cdot\nabla C = D\nabla^2 C + R \quad (5.4)$$

where C is the concentration of the molecule, u velocity, and D the diffusion coefficient. R is the reaction rate which is given by the following Michaelis-Menten equation.

$$R = \frac{V_m \cdot C}{K_m + C} \quad (5.5)$$

Equations 5.1~5.5 were solved simultaneously on COMSOL (COMSOL, Burlington, MA). To reduce the size and the simulation time of the model, two-dimensional x-z geometry was assumed. The concentration profiles of resorufin at a fixed point inside the detection chamber were exported and plotted. The parameters for both models and the boundary conditions for the convection-diffusion model are summarized in Table 5.1 and 5.2. The diffusivity of a substrate (ethoxyresorufin) and a product (resorufin) in water was found from literature (Benes et al. 2001). The diffusivity of the substrate and the product in hydrogel was assumed to be 75% of the diffusivity in water, based on the study by Brown et al (Brown et al. 2007).

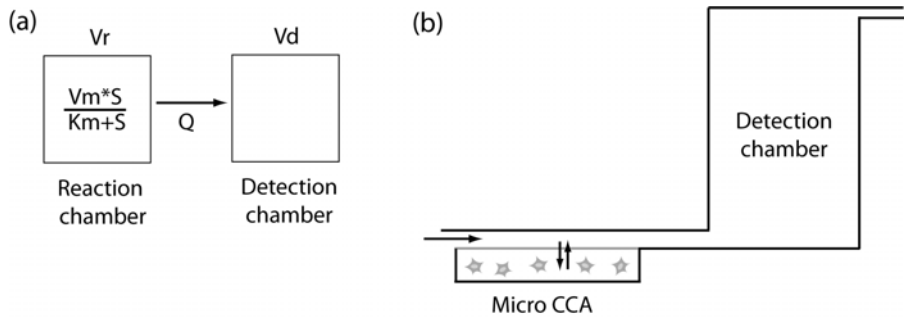

Figure 5.4 Mathematical models describing the micro cell culture analog system and a detection chamber.

(a) Simple two-compartment model. It is assumed that the two compartments are well-mixed and homogeneous. In the first compartment enzymatic reaction occurs, which is described by the Michaelis-Menten kinetics. The two compartments are connected by flow rate Q. (b) Convection-diffusion model. The exact geometries were drawn and the Navier-Stokes equation and mass balance equation were solved simultaneously to obtain concentration profiles of product resorufin. The schematic diagram shown here is not drawn to the actual scale of the system.

Table 5.1 Parameters used in the simulation of a well-mixed model and a convection-diffusion (C-D) model.

Name	description	value
Well-mixed model		
Q	Flow rate	2 μL/min
V_{CCA}	Volume of CCA	5 μL
V_D	Volume of detection chamber	400 μL
V_m	Maximum enzyme activity	44 nM/min (fitted to experimental data)
K_m	Michaelis constant	2400 nM (fitted to experimental data)
C-D model		
V	Average fluid velocity	2.2×10^{-3} m/min (from experiment)
D_{ethres}	Diffusivity of ethoxyresorufin	2.4×10^{-8} m^2/min (Benes et al. 2001)
D_{res}	Diffusivity of resorufin	1.8×10^{-8} m^2/min (Benes et al. 2001)
Rho	Density	1×10^{3} kg m^{-3}
Mu	Viscosity	6×10^{-2} kg $m^{-1}min^{-1}$
V_m	Maximum enzyme activity	44×10^{-13}/min/cell (fitted to experimental data)
K_m	Michaelis constant	2400 nM (fitted to experimental data)
S	Initial substrate concentration	1×10^{4} nM

Table 5.2 Boundary and sub-domain conditions used in the simulation of a convection-diffusion model. N-S: Navier-Stokes, C-D: Convection and Diffusion.

Boundary	**N-S**	**C-D substrate**	**C-D product**
Inlet	Velocity, $u_0=0$, $v_0=-v$	Concentration, $c_0=S$	Concentration, $c_0=0$
Outlet	Pressure, $P_0=0$	Convective flux	Convective flux
Others	No slip	Insulation/Symmetry	Insulation/Symmetry
Sub-domain	**N-S**	**C-D substrate**	**C-D product**
Perfusion area	ρ=Rho, μ=Mu	$D = D_{ethres}$	$D = D_{res}$
Hydrogel area	N/A	$D = 0.75 \times D_{ethres}$	$D = 0.75 \times D_{res}$

5.3 Results

5.3.1 Ethanol Toxicity Experiment

We tested cell response to ethanol addition and in two identical μCCA chips. HepG2/C3A cells were treated with calceinAM for fluorescence detection prior to the packaging of μCCA. Figure 5.5 shows the result in terms of cell viability index (CVI). CVI was defined as the ratio of the cell number at a specific time to the initial cell number. In other words, CVI measures relative increase or decrease in reference to the initial cell number. The graph shows that when the cells were exposed to ethanol, it immediately caused cell death, and all cells died within the time range of few minutes to one hour, depending on the applied concentration of ethanol.

Figure 5.6 shows real-time fluorescence images of HepG2-C3A cells at various EtOH concentrations. Figures 5.5 and 5.6 emphasize the strengths of our system to track the migration and motility of an individual cell and also to observe cell dynamics quantitatively. Here, τ was obtained as a function of EtOH concentration from an exponential fit, i.e. $CVI(t) = CVI(t = 0)\exp(-t/\tau)$, with the reference CVI for cell death set to be 1%. Figure 5.7 presents the necrosis time constant τ over different EtOH concentration values. More specifically, at 20% EtOH, HepG2-C3A cells die quickly in 10 minutes, while it takes 30 and 100 minutes at 10% and 5% EtOH, respectively. In other words, the time constant τ itself is a function of EtOH concentration, as shown in Figure 5.7. Figure 5.7 suggests that the dependence of τ on EtOH is not linear. Good correlation was achieved with an inverse relationship, i.e. $\tau(C_{EtOH}) = A/CEtOHn$, where C_{EtOH} denotes ethanol concentration. A and n are fitting constants and were found to be A = 1300 and n = 1.6.

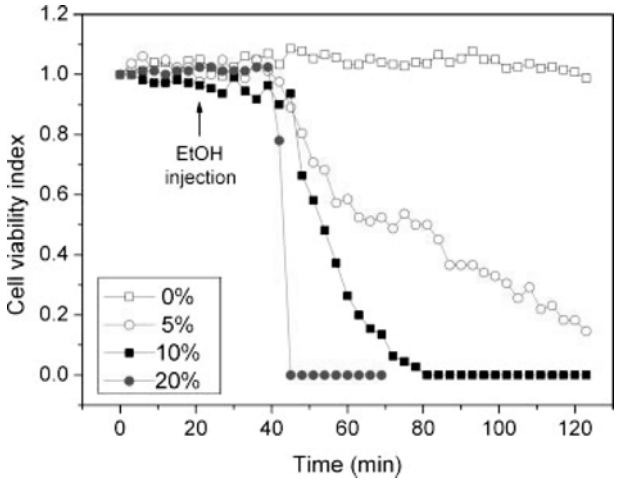

Figure 5.5 Time course of cell viability index in response to ethanol

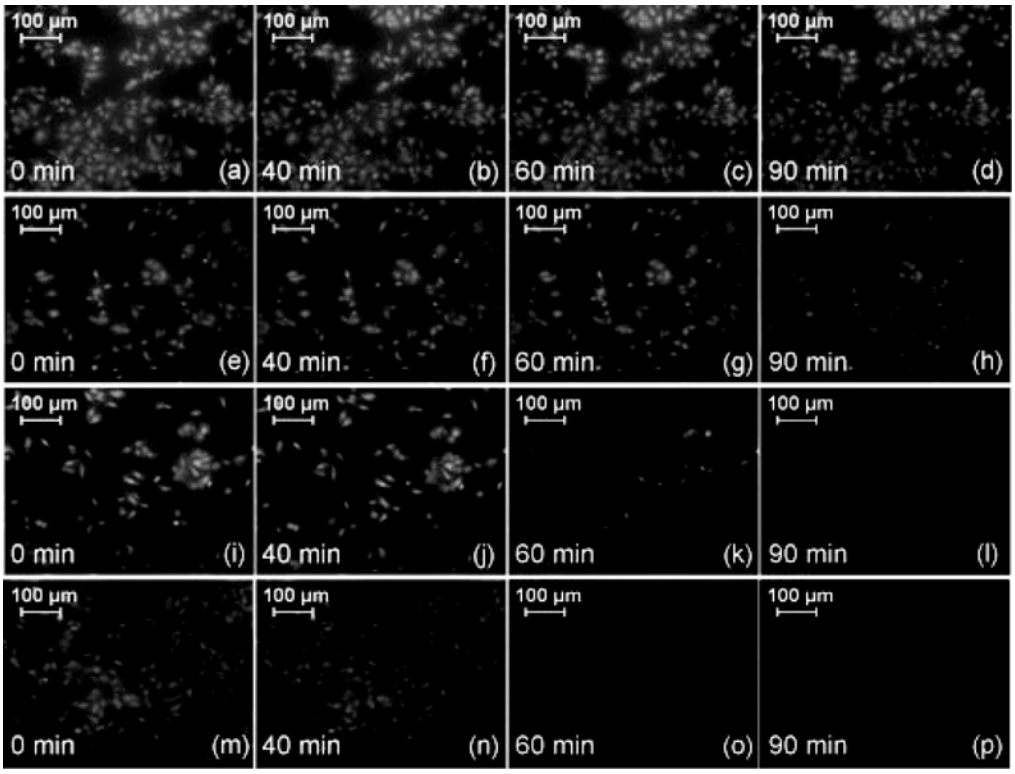

Figure 5.6 Exposure of cells to ethanol

Fluorescence images of HepG2-C3A cells exposed to EtOH concentration of 0% (control, top row, a-d), 5% (second row, e-h), 10% (third row, i-l), and 20% (bottom row, m-p). EtOH was injected 20 minutes after the test was begun.

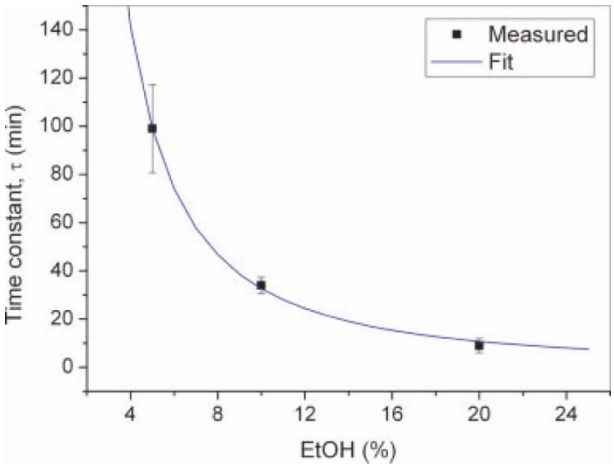

Figure 5.7 Necrosis time constant at various ethanol concentrations

5.3.2 CalceinAM Injection and Cell Staining Experiment

CalceinAM was supplied by injecting it through microfluidic channels. The main purpose of this is to understand the dynamics of calceinAM staining. Results in Figure 5.8 shows that the calceinAM fluorescence intensity increases until 10% EtOH was injected at 90th minute and delivered through a tube to reach cells. Figure 5.8 (b) shows fluorescent images that reflect the dynamics of staining and the fluorescence intensity loss caused by EtOH.

5.3.3 Cell Growth Monitoring

The growth curve of MESSA H2B-GFP cells in the chamber B of the first μCCA chip has been obtained after an experiment for over 85 hours, as shown in Figure 5.9. The growth curve for MESSA H2B-GFP cells shows that cells start proliferating after an initial lag phase (about 30 hours). Cells then grow until about 65 hour (from 0.95 to 1.33 a.u.). After the stationary phase, the cell number starts to decrease. The death of cells can be attributed to nutrient depletion and a change in the pH due to the accumulation of wastes from cell metabolism.

Figure 5.9 also presents the cell growth and maintenance curve of HepG2-C3A H2B-GFP cells in the chamber A of the second μCCA chip. Cell growth index was defined for quantitative comparison as normalized cell number with respective to an initial cell number. The results show that HepG2-C3A H2B-GFP are subject to contact inhibition and cell number does not change significantly, which was expected as the cells were seeded on the chip at about 90% confluency. HepG2-C3A is a derivative cell-line of HepG2 cell-line, selected for strong contact inhibition of growth and high albumin production.

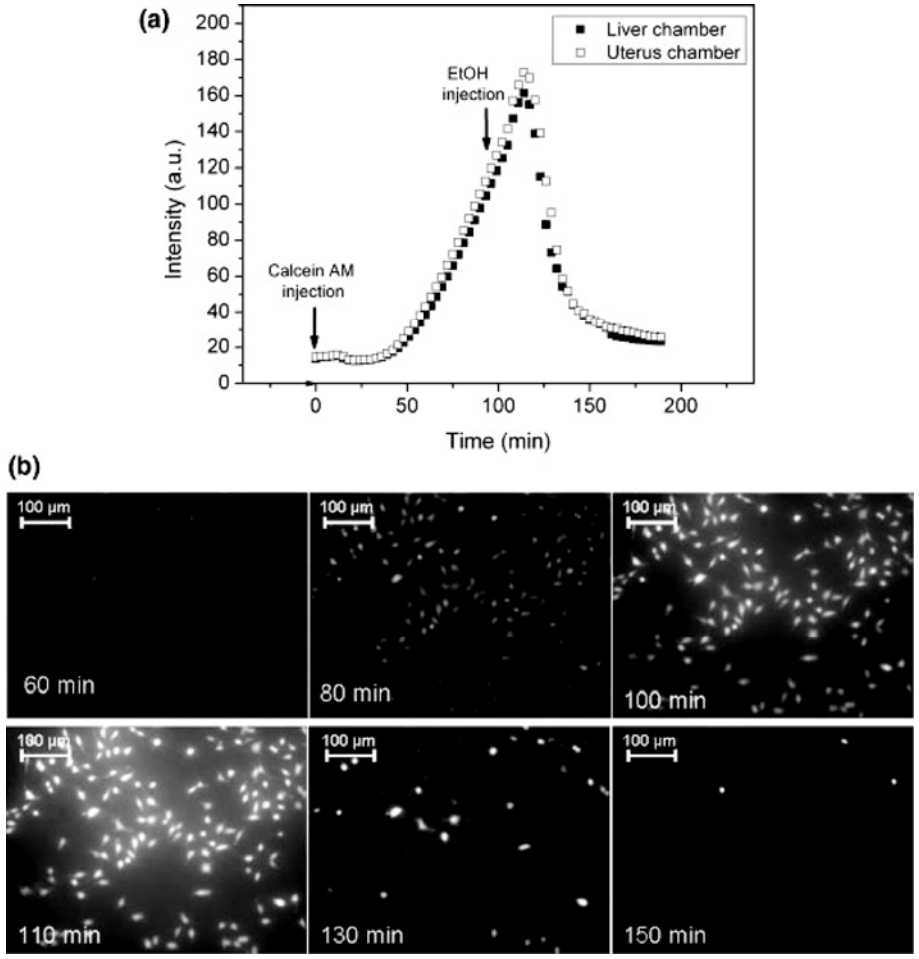

Figure 5.8 Staining/cell death experiment

(a) Fluorescence intensity graph of HepG2-C3A cells in liver and uterus cancer chamber that shows initial calceinAM uptake and following cytotoxicity of 10 % EtOH injected at 90th minute. (b) Corresponding fluorescence images of HepG2-C3A cells in the liver chamber.

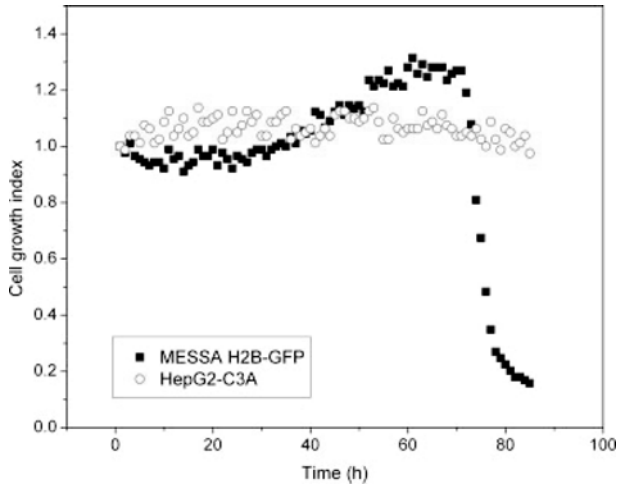

Figure 5.9 Cell growth of MESSA H2B-GFP and HepG2-C3A cells in a μCCA

5.3.4 Linearity Calibration of Resorufin Fluorescent Intensity

Figure 5.10 presents the calibration results measured by a commercial fluorescence plate reader and the ISFODS. Various concentrations of resorufin samples were made and measured with a plate reader and ISFODS. The measured output from the 96-well microtiter plate was recorded for each sample. With the ISFODS, measurements were made in a static environment without flow. These results demonstrate similar sensitivity and response linearity of the ISFODS to those of a commercial fluorescence plate reader.

The lowest detection limit of resorufin in the current experimental setting was approximately 1 nM. In the concentration range of 1 nM to 10 μM resorufin, both systems showed similar bi-phase responses. In the low concentration range (1 nM~1 μM), the data showed linear responses in the fluorescence plate reader and ISFODS with correlation coefficients R2 = 0.9946 and 0.9869, respectively (Figure 3, inset). Highly linear responses were also observed at higher concentrations (1 μM~10 μM) with a decreased slope. Correlation coefficients for the fluorescence plate reader and the ISFODS in this range were 0.9957 and 0.9967, respectively. In both measurement systems, the changes of slopes occur at near 1 μM, which further validates the consistency of the ISFODS with conventional detection systems. In the case of the ISFODS, the y-intercept was not zero, which we believe to be associated with the fact that the incubator door was not completely closed due to the cables connecting the ISFODS and a computer. A small, but noticeable amount of stray light through the opening could have interfered with the system. For the following experiments, the measured output readings from the ISFODS were converted to the corresponding resorufin concentrations.

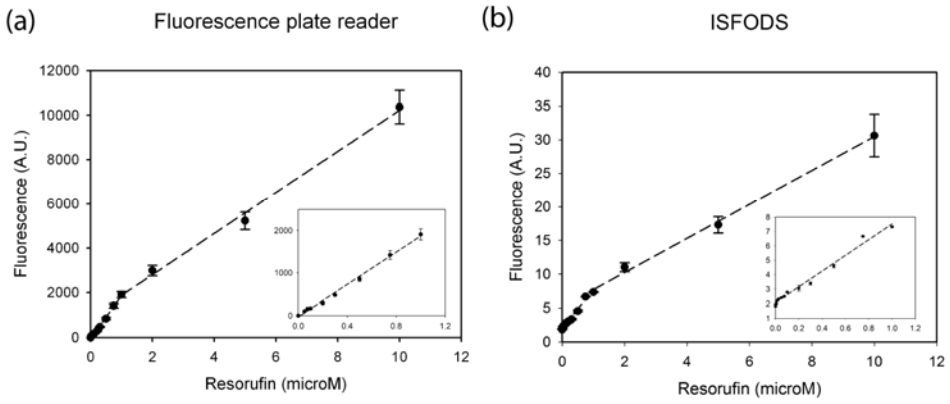

Figure 5.10 Linearity calibration of ISFODS

Comparison of (a) fluorescent plate reader and (b) ISFODS for linearity calibration of fluorescent signal measurement. Both show similar responses to resorufin concentrations with two linear regions between 0 and 10 μM. Shown in the inset is a close-up of the low concentration range. Different slopes of linear responses were observed in the low concentration range (1 nM~1 μM), and the high concentration range (1 μM~10 μM) for both detection systems.

5.3.5 Measurement of P450 1A1/1A2 Enzyme Activity of HepG2/C3A Cells in a 96-well Plate and a μCCA

In this study, we used a hepatoma cell line HepG2/C3A, which is a derivative cell line of HepG2 (Kelly 1994). The P450 1A1/1A2 activity of the cells was tested in two different environments (96-wells and μCCA). In a 96-well plate, cells were cultured in a 2-D monolayer in culture medium containing ethoxyresorufin. As the P450 1A1/1A2 enzymes in the cells convert the weakly fluorescent substrate ethoxyresorufin to a fluorescent product resorufin, the fluorescence intensity of the product was measured using a fluorescence plate reader. In a μCCA, cells were embedded in a matrix of Matrigel^{TM} and medium containing ethoxyresorufin was perfused through a microfluidic channel. As the medium flows over the Matrigel-cell matrix, ethoxyresorufin diffuses into the matrix and is converted to resorufin by enzyme reaction (Figure 5.3(b)). Along with the medium flow, the fluorescent product is moved to the detection chamber and detected by the ISFODS (Figure 5.3(a)). For both the fluorescent plate reader and the ISFODS, multiple measurements were taken in a single experiment ($n > 3$). Field of view changes at each measurement with a fluorescent plate reader, while it is maintained as constant with the ISFODS.

Figure 5.11 shows the fluorescence activity measured in a 96-well plate by a plate reader (a) and in a μCCA by the ISFODS (b). In the case of measuring resorufin in a μCCA with the ISFODS, time zero corresponds to the time for the initial detection of fluorescence activity, rather than the time the medium perfusion was started, due to time delays associated with flow. Note that it would take a certain amount of time (usually 15 to 20 minutes) for medium to flow through channels and reach the detection chamber. In the case of a 96-well plate with a fluorescence plate reader, the time zero corresponds to the time ethoxyresorufin was added, when the enzymatic

reaction starts. In Figure 5.11, both the fluorescence plate reader with a 96-well plate and the ISFODS with a μCCA showed a gradual decrease of background signal, if there were no cells present. The similarity implies that the decrease in background is caused by the object of detection, either the culture medium or the wells, rather than the detection systems. The decrease may be associated with photobleaching or binding of weakly fluorescent molecules in the medium to the surfaces of the wells or the μCCA.

In a 96-well plate, uninduced HepG2/C3A cells showed a detectable, yet a low P450 1A1/1A2 activity. If the cells were chemically induced, they showed significantly higher activity (Figure 5.11(a)). This observation was consistent with a previous report (Kelly and Sussman 2000). On the other hand, the behavior of the cells cultured in 3-D matrix in a μCCA was different from that of the cells in a 96-well plate. Uninduced cells in the μCCA showed a higher P450 1A1/1A2 activity than those cultured in a 96-well plate, whereas the activity of induced cells was not statistically different from the activity of uninduced cells for the first 100 minutes (Figure 5.11(b)). The reason for the lack of response to chemical induction in the 3-D gel cultures in the μCCA is uncertain. One possibility would be that the gel and the microfluidic environment have already acted as an inducer, saturating the induction response of the liver cells. Another possibility is a stress response in the cells due to the extra handling required to move and place the cells in a gel and a microfluidic device. It should also be noted that the inducer 3-MC was observed to reduce cell viability during 48 hours of induction (data not shown). Regardless of the reason, it is important that the dynamics of the system were captured by the ISFODS.

To further explore the sensitivity and the resolution of the ISFODS, we investigated a μCCA with the ISFODS in different conditions and compared the data with simulation results. First, we tested different substrate concentrations (1 μM and

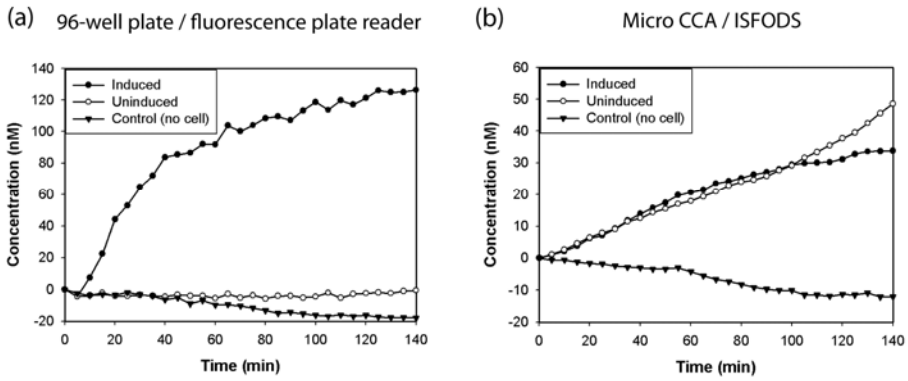

Figure 5.11 P450 1A1/1A2 activity of HepG2/C3A cells as measured by the formation of resorufin

(a) 96-wells + fluorescence plate reader (b) μCCA + ISFODS. In 96-wells, uninduced HepG2/C3A cells showed slightly higher signal than no-cell control, whereas in a μCCA, uninduced cells showed significantly higher activity than no-cell control. In 96-wells, cells induced with 3-MC showed significantly higher activity than uninduced cells, whereas in a μCCA, induction did not increase the enzyme activity. The total number of cells in a 96-well and a μCCA were controlled to be approximately at 100,000 cells.

10 μM, Figure 5.12). As expected, higher substrate concentration resulted in faster conversion kinetics, consistent with simulation results. This data was used to fit the kinetic parameters of P450 1A1/1A2 enzyme in the mathematical models, which were found to be V_m = 44 nM/min and K_m = 2400 nM. In the case of measuring cells in well-plates with a plate reader, the kinetic parameters of P450 1A1/1A2 enzyme are not available to the best of our knowledge. A potential reason for this absence of prior data is that the cells did not show significant activity in a well plate unless they were artificially induced, which makes the acquisition of kinetic parameters difficult. Also note that the measurement performed with a plate reader is not *in situ*, thus obtained kinetic parameters would be subject to larger errors even if they can be extracted. This presents the strength of *in situ* measurement of a μCCA using the ISFODS in extracting reaction coefficients such as conversion rate of ethoxyresorufin into resorufin products on a quantitative basis. Secondly, the cell density inside μCCA was varied, while the substrate concentration was fixed at 1 μM (Figure 5.13). Three different cell densities were tested (1X, 2X, and 4X correspond to 5 x 10^4, 1 x 10^5, and 2 x 10^5 cells/ml, respectively). In general, the higher cell density resulted in the higher P450 1A1/1A2 activity, which was verified with mathematical analysis based on convection-diffusion model. In the experimental data shown as dots in Figure 5.13, when the cell number in a μCCA was increased from 5 x 10^4 cells/ml to 1 x 10^5 cells/ml, the product of enzymatic reaction increased approximately two-fold. For example, after 75 minutes, the resorufin concentration was measured to be 5.52 nM and 10.6 nM in cases of 1X and 2X cell number, respectively. However, in the case where the cell number was increased from 1 x 10^5 cells/ml to 2 x 10^5 cells/ml, the product concentration increased only about 50% (10.6 nM and 16.9 nM). To examine the effect of hydrogel cell culture on the P450 1A1/1A2 activity of HepG2/C3A cells, the cells were encapsulated in Matrigel™ and cultured, both in 96-

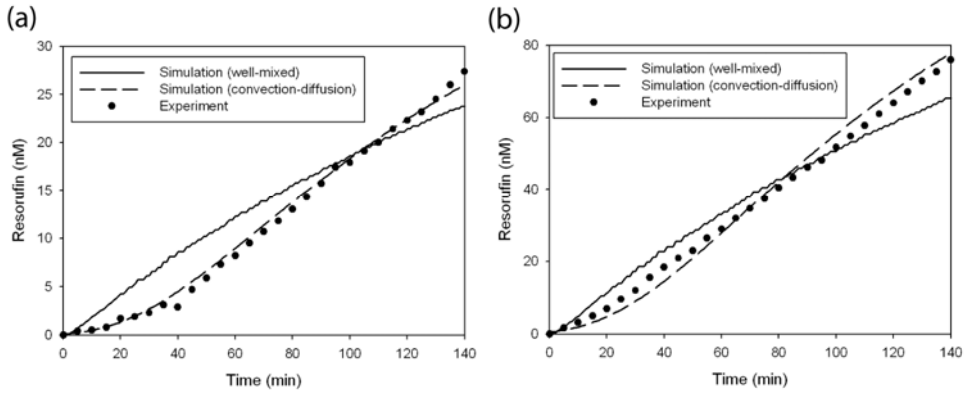

Figure 5.12 Simulated and measured resorufin formation at different substrate concentrations

(a) 1 μM and (b) 10 μM substrate concentration. In both cases, the well-mixed, two-compartment model predicts faster saturation than experimental results or the convection-diffusion model.

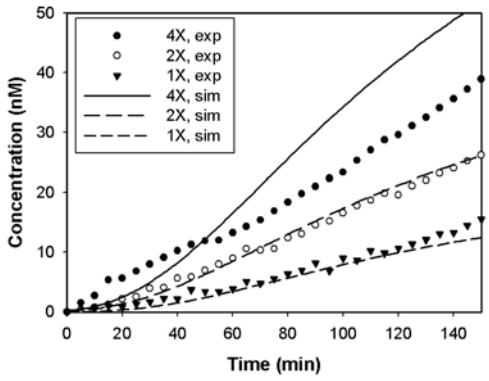

Figure 5.13 Simulated and measured resorufin formation at varying cell concentration. 1X corresponds to 50,000 cells, 2X corresponds to 100,000 cells, and 4X corresponds to 200,000 cells in the liver chamber. The increase in the cell number resulted in the increased enzyme activity, although the amount of increase was not proportional at the highest cell number.

well plates. The P450 1A1/1A2 activities of the hydrogel-embedded cells and cells in monolayer were compared. Cells cultured in Matrigel™ showed slightly higher enzyme activity over the control, although the difference was not statistically significant (Figure 5.14). This result suggests that the microfluidic versus the static environment was responsible for the different responses of the uninduced cells.

5.4 Discussion

5.4.1 Ethanol Toxicity and CalceinAM Staining

The acute toxicity ethanol upon cells was observed in real-time using the ISFODS. As seen in Figure 5.5 and 5.6, cells showed dose-dependent response to ethanol. Ethanol causes an immediate cell lysis and death, and subsequent loss of fluorescence signal of CalceinAM. The major cause of fluorescence loss was due to the damage of cell membrane and leakage of fluorescent calcein molecules from the cytoplasm. The calcein molecules are subsequently washed away by the flow inside a μCCA. At a sufficiently low flow rate, the calcein molecules are not washed away as quickly, and we could observe the whole background getting brighter, due to the calcein molecules leaking. One difficulty associated with observing the cell staining process inside a μCCA was that initially the area of detection is completely dark, so it is difficult to focus onto the cells. To avoid such an issue, we needed to work out in advance the appropriate position of the optical components so that when cells start to become fluorescent, the cells are appropriately focused. Still, we needed to further adjust the focus in a relatively short time to ensure that the early phase images are taken.

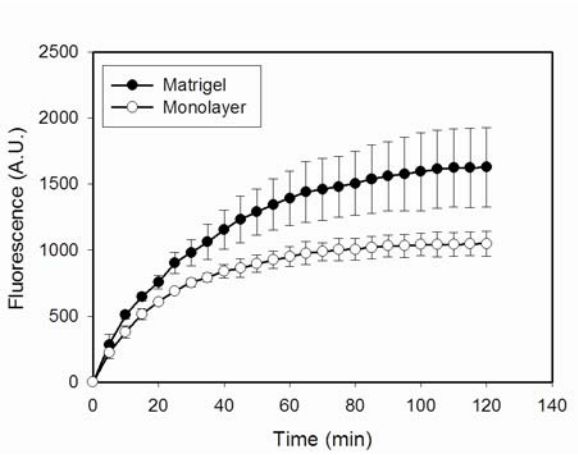

Figure 5.14 P450 1A1/1A2 activities of chemically induced HepG2/C3A cells

5.4.2 Cell Growth Monitoring with ISFODS

It was demonstrated that using the ISFODS, the growth of cells could be monitored for several days while operating a microfluidic device. The reason for seeding the cells at a high density was to ensure that the cells made a good contact to the silicon surface, so that the cells could maintain their viability in the presence of hydrodynamic shear stress. When cells were seeded in a lower density and the flow was introduced, often cells seemed to be less healthy and less spread out, judging from the cell morphology under the microscope. It has been shown that the spreading and making a strong adhesion to the surface is important for the viability of cells (Ruoslahti 1997; Chen et al. 1998).

In the case of HepG2-C3A H2B GFP cells, the cell number does not decrease significantly even after 80th hour, although the decrease appears to start after about 55th hour. This trend is associated with the nature of the HepG2-C3A cell-line that typically adheres to the surface more strongly than the tumor cell-line MESSA H2B-GFP. When HepG2-C3A cells are cultured in culture flasks and trypsinized for a subculture, they are rinsed with 0.25% (w/v) trypsin and 0.53 mM EDTA solution. They generally require a longer incubation time with trypsin-EDTA than other tumor cell-lines until the cells detach from the surface. For an identical incubation time, HepG2-C3A cells likely adhered to the surface even at a critical stage where the tumor cells have already been detached. HepG2-C3A cells may also be more resistant to the stress conditions that inhibit MESSA H2B-GFP cells.

Unlike experiments where cell-based assays are measured for a relatively short period of time, cells in long-term assays undergo a number of cell mitoses that are often accompanied by cell detachment. Unlike static cell culture conditions, in a microfluidic environment mitotic cells can detach from the surface due to shear,

therefore a quiescence state of cells can be obtained depending on the flow rate (Prokop et al. 2004). This means that cell growth index tends to be underestimated, which may explain why cell growth index in the case of HepG2-C3A cells does not grow significantly and relative mild increase for MESSA H2B-GFP cancer cells.

5.4.3 Enzyme Activity Monitoring in μCCA

Experiments with HepG2/C3A cells revealed that the hepatoma cells showed considerably different behavior when they were cultured in 3-D matrix in a microfluidic environment. The level of P450 enzymes in hepatoma HepG2 is reported to be significantly lower than the level in hepatocytes (Wilkening et al. 2003), which was consistent with our 96-well plate experiment result. However, it was observed in this study that the P450 enzyme activity of hepatoma cells cultured in the matrix of Matrigel^{TM} inside a μCCA was significantly higher than the same cells cultured in 2-D monolayer in a well. Possibly the higher activity observed in a μCCA may be because the microfluidic environment inside a μCCA is closer to the physiological microenvironment than a 2-D monolayer cell culture in a 96-well plate. According to recent studies, a culture of hepatocytes with an ECM layer is known to help hepatocytes retain liver-specific functions better (De Smet et al. 2000), and culturing hepatocytes in 3-D scaffold has shown to be advantageous for restoring liver-specific functions (Sivaraman et al. 2005). A sub-lethal shear stress that is present in a microfluidic device can also be advantageous in enhancing P450 activity (Mufti and Shuler 1995). The microenvironment in a μCCA may provide all these factors, since the cells are cultured embedded in Matrigel^{TM}, which is a mixture of various ECM proteins and growth factors. In addition, the medium perfusion may provide an appropriate level of hydrodynamic shear for the cells. To assess the effect of culturing

the cells in Matrigel, P450 1A1/1A2 activity of HepG2/C3A cells in Matrigel was measured in a 96-well plate and a slight increase in the P450 activity was observed (Figure 5.14). Therefore the contribution of a constant flow seems to be greater than Matrigel^{TM}, although the effect may be synergistic. The effect of microenvironment in a hydrogel matrix on the metabolic activity of liver cells inside a microfluidic device is under further study.

5.5 Conclusion

The ISFODS described in this chapter is a compact optical system built to enable integration with an operating microfluidic cell culture system for real-time fluorescence measurements. Combined with mathematical modeling, the system was shown to provide detailed quantitative analysis of reactions within a microfluidic device and extraction of enzyme kinetic parameters without disrupting the operation. In previous studies, we demonstrated that a combined effort of an experimental approach such as μCCA and a mathematical modeling, e.g., a PBPK model, can be a powerful tool in gaining insights into the mechanism of drug toxicity (Sweeney 1995; Ghanem and Shuler 2000). The development of more accurate and detailed mathematical models of a microfluidic system depends critically upon the availability of real-time data measured, for example, by the ISFODS described in this paper. The *in situ* measurement system can be a versatile tool as an analytical module combined with various microfluidic perfusion cell culture devices in diverse formats and can provide real-time, on-chip analysis that may not be available using a plate reader or a conventional microscope. Furthermore, multiplexing the μCCA devices with this type of an optical detection system would facilitate operation in high-throughput modes.

REFERENCES

Bambot, S., et al. (1994). "Optical oxygen sensor using fluorescence lifetime measurement." Adv Exp Med Biol 361: 197-205.

Benes, M., et al. (2001). "Coumarin 6, hypericin, resorufins, and flavins: suitable chromophores for fluorescence correlation spectroscopy of biological molecules." Coll. Czech. Chem. Commun 66: 855-869.

Brown, D. A., et al. (2007). "Analysis of oxygen transport in a diffusion-limited model of engineered heart tissue." Biotechnol Bioeng 97(4): 962-75.

Camp, J. P. and A. T. Capitano (2007). "Induction of zone-like liver function gradients in HepG2 cells by varying culture medium height." Biotechnol Prog 23(6): 1485-91.

Chen, C. S., et al. (1998). "Micropatterned surfaces for control of cell shape, position, and function." Biotechnol Prog 14(3): 356-63.

Cheng, S. Y., et al. (2007). "A hydrogel-based microfluidic device for the studies of directed cell migration." Lab Chip 7(6): 763-9.

Coward, S. M., et al. (2005). "Proliferation rates of HepG2 cells encapsulated in alginate are increased in a microgravity environment compared with static cultures." Artif Organs 29(2): 152-8.

De Smet, K., et al. (2000). "Biotransformation of trichloroethylene in collagen gel sandwich cultures of rat hepatocytes." Arch Toxicol 74(10): 587-92.

Donato, M. T., et al. (1993). "A microassay for measuring cytochrome P450IA1 and P450IIB1 activities in intact human and rat hepatocytes cultured on 96-well plates." Anal Biochem 213(1): 29-33.

Donato, M. T., et al. (2004). "Fluorescence-based assays for screening nine cytochrome P450 (P450) activities in intact cells expressing individual human P450 enzymes." Drug Metab Dispos 32(7): 699-706.

Garcia, E., et al. (2007). "High-throughput screening of enzyme inhibition using an inhibitor gradient generated in a microchannel." Lab Chip 7(2): 249-55.

Ghanem, A. and M. L. Shuler (2000). "Combining cell culture analogue reactor designs and PBPK models to probe mechanisms of naphthalene toxicity." Biotechnol Prog 16(3): 334-45.

Giepmans, B. N., et al. (2006). "The fluorescent toolbox for assessing protein location and function." Science 312(5771): 217-24.

Kelly, J. H. (1994). Permanent human hepatocyte cell line and its use in a liver assist device (LAD). US Patent 5,290,684

Kelly, J. H. and N. L. Sussman (2000). "A fluorescent cell-based assay for cytochrome P-450 isozyme 1A2 induction and inhibition." J Biomol Screen 5(4): 249-54.

Kim, L., et al. (2007). "A practical guide to microfluidic perfusion culture of adherent mammalian cells." Lab Chip 7(6): 681-94.

Mufti, N. A. and M. L. Shuler (1995). "Induction of cytochrome P-450IA1 activity in response to sublethal stresses in microcarrier-attached Hep G2 cells." Biotechnol Prog 11(6): 659-63.

Novak, L., et al. (2007). "An integrated fluorescence detection system for lab-on-a-chip applications." Lab Chip 7(1): 27-9.

Pihl, J., et al. (2005). "Microfluidic technologies in drug discovery." Drug Discov Today 10(20): 1377-83.

Prokop, A., et al. (2004). "NanoLiterBioReactor: long-term mammalian cell culture at nanofabricated scale." Biomed Microdevices 6(4): 325-39.

Ruoslahti, E. (1997). "Stretching is good for a cell." Science 276(5317): 1345-6.

Sivaraman, A., et al. (2005). "A microscale in vitro physiological model of the liver: predictive screens for drug metabolism and enzyme induction." Curr Drug Metab 6(6): 569-91.

Stresser, D. M., et al. (2002). "Cytochrome P450 fluorometric substrates: identification of isoform-selective probes for rat CYP2D2 and human CYP3A4." Drug Metab Dispos 30(7): 845-52.

Sung, J. H. and M. L. Shuler (2009). "A micro Cell Culture Analog (micro CCA) with 3-D hydrogel culture of multiple cell lines to assess metabolism-dependent cytotoxicity of anti-cancer drugs." Lab Chip 9(10): 1385-94.

Sweeney, L. M., Shuler, M. L., Babish, J. G., Ghanem, A. (1995). "A cell culture analogue of rodent physiology: application to naphthalene toxicology." Toxicology in vitro 9(3): 307-316.

Wilkening, S., et al. (2003). "Comparison of primary human hepatocytes and hepatoma cell line Hepg2 with regard to their biotransformation properties." Drug Metab Dispos 31(8): 1035-42.

Yu, H., et al. (2007). "A plate reader-compatible microchannel array for cell biology assays." Lab Chip 7(3): 388-91.

CHAPTER 6

A MICROFLUIDIC DEVICE FOR A PHARMACOKINETIC-PHARMACODYNAMIC (PK-PD) MODEL ON A CHIP

6.1 Introduction

The potential importance of microfluidic systems in improving the drug development process has been widely recognized (Kang et al. 2008). Microfluidics can be especially useful for reproducing the pharmacokinetics of drugs, since structures with multiple components, for example, a metabolizing component and a target component, can be created and connected with fluidic channels for interactions. Recently, Ma et al. developed a three-layer microfluidic system to test metabolism-dependent toxicity of drugs (Ma et al. 2009). The device consists of a top-layer for feeding drugs, a middle layer with sol-gel human liver microsomes bioreactor for metabolism, and a bottom-layer for cell culture chambers. Molecules are transported through the layers via diffusion, and the effect of acetaminophen metabolism on target cells was observed using the system. In another study, a hepatocyte-bioreactor was developed to assess hepato-activated transformation of substrates (Koebe et al. 2000). These systems successfully demonstrated that the metabolism-dependent toxicity of drugs can be observed *in vitro*, but does not reproduce the true dynamics of drug exposure to the human body.

Previously, we developed a micro cell culture analog (μCCA), also known as 'body-on-a-chip', which is a microfluidic device for pharmacokinetic-based drug toxicity test (Sin et al. 2004; Khamsi 2005). Multiple cell types representing different organs are cultured on a single chip, interconnected by channels mimicking the blood flow pattern. The fluid pattern in the μCCA is calculated to mimic the blood

circulation, thus mimicking the pharmacokinetics of drugs. In a proof-of-concept study, a μCCA was used to test the metabolism-dependent toxicity of naphthalene, doxorubicin, and Tegafur (Viravaidya et al. 2004; Sung and Shuler 2009; Tatosian and Shuler 2009). The μCCA was originally conceived as a physical realization of physiologically-based pharmacokinetic (PBPK) modeling approach. It has been demonstrated that the combination of a PBPK modeling and a μCCA can provide an insight into the mechanism of naphthalene toxicity (Ghanem and Shuler 2000).

Although microfluidic systems have a great potential in enhancing the drug development process, actual applications of microfluidic systems in medical or life science area have been limited. One important reason for this is because current microfluidic devices require specialized skills for fabrication and operation, which makes it difficult to be used by non-experts in the field (Meyvantsson et al. 2008). In addition, unlike conventional cell culture systems that have been well-established over the past century, microfluidics have several issues that need more in-depth study, such as biocompatibility of materials, maintenance of sterility, formation of air bubbles, and the effect of shear stress on cells (Kim et al. 2007). We have seen a substantial amount of progress in terms of developing highly-complex microfluidic devices for high-throughput implementation (Yang et al. 2008), but not much progress has been achieved in terms of simplifying the design and improving the usability of microfluidic systems, which will facilitate a wider use of microfluidic devices in the area outside engineering.

The work described in this chapter has two main focuses. First, a microfluidic device was designed to enhance the usability of the device and make a high-throughput operation easier, while allowing 3-D hydrogel cell cultures of multiple cell types to be inserted into separate chambers of a device to reproduce a multi-organ interaction. The simplicity in the device design offers several advantages. The use of

gravity-induced flow eliminates the need for a pump, and prevents formation of air bubbles. 3-D hydrogel cell cultures of defined shape and thickness can be inserted into the device. Secondly, the microfluidic device was combined with a mathematical model to quantitatively analyze the effect of a chemotherapeutic agent, 5-fluorouracil (5-FU). A PK-PD model that describes the response of cells to 5-FU was developed and fitted to experimental results, and the effect of combining the drug with a modulator, uracil, was predicted and compared with experimental results. To the best of our knowledge, this is the first attempt to combine a microfluidic system with an integrated PK-PD modeling approach to achieve 'PK-PD model-on-a-chip'. We believe that this combined approach of an *in vitro*/*in silico* system enables prediction of drug toxicity in a more realistic manner than conventional *in vitro* systems.

6.2 Materials and Methods

6.2.1 Cell Culture and Chemicals

McCoy's 5a medium was purchased from Sigma Aldrich (St Louis, MO). MEM medium, RPMI 1640 medium, and Fetal bovine Serum (FBS) were purchased from Invitrogen (Carlsbad, CA). A Live/Dead viability/cytotoxicity kit for mammalian cells was obtained from Invitrogen. HEPES, sodium chloride, uracil, and 5-fluorouracil (5-FU) were purchased from Sigma Aldrich. The colon cancer cell line, HCT-116, was obtained from American Type Culture Collection (ATCC, Manassas, VA) and cultured in a T-flask in McCoy's 5a medium (Sigma Aldrich) with 10% FBS (Invitrogen). A hepatoma cell line, HepG2/C3A (ATCC), was maintained in MEM medium (Invitrogen) with 10% FBS. Myeloblast cell line Kasumi-1 (ATCC) was maintained in RPMI-1640 medium (ATCC) with 20% FBS. All cell lines were cultured in a mammalian cell incubator maintained at 37℃ with 5% CO_2.

6.2.2 Design and Fabrication of a Micro Cell Culture Analog (μCCA)

The μCCA device consists of multi-layers of PDMS (polydimethyldisiloxane), sealed between aluminum bottom and plexiglass top frames with screws (Figure 6.1). Underneath the top plexiglass top frame, a PDMS fluidic channel layer is placed. This provides the fluidic conduits for three cell culture chambers and inlet and outlet holes for medium recirculation. The geometry of the channels for each chamber is designed to mimic the blood flow distribution of the human body (58%, 18%, and 24% into the liver, tumor, and the marrow compartment, respectively) (Davies and Morris 1993; Sung and Shuler 2009). Beneath the channel layer, cell culture chamber layer is placed. This layer is a 0.2 mm thick silicone layer with three through-holes for cell culture chamber and two through-holes for inlet and outlet. Hydrogel-encapsulated cells representing the liver, tumor and the marrow will be placed in each chamber. The cell culture chamber layer is placed on top of a polycarbonate base, which provides a surface to support the hydrogel matrix. Between the polycarbonate base and the bottom aluminum frame, a 0.5 mm silicone gasket (Grace Bio Labs) is placed, mainly to provide a sealing between the aluminum and polycarbonate pieces. The polycarbonate base and a silicone gasket also have two inlet and outlet through-holes, which are to be aligned with inlet/outlet holes in other layers. All of these layers are clamped between top and bottom frames, as explained in the assembly section.

The channel layer was fabricated using conventional soft-lithography techniques. The design of the channels was drawn using AutoCAD (Autoworks, San Rafael, CA), and the design was converted and exposed onto a Chrome-coated glass mask using GCA/MANN 3600F Optical Pattern Generator (Ultratech, San Jose, CA). SU-8 2075 (MicroChem, Newton, MA) of 225 μm thickness was spin-coated on a silicon wafer by spinning at 300 rpm for 30 seconds. After soft-baking at 65 ℃ for 5

minutes the temperature was raised to 95 ℃ and left for 45 minutes. The pattern on the glass mask was exposed to SU-8 coated silicon wafer at 650 mJ/cm^2 using EVG620 contact aligner (EV Group, Tempe, AZ). Then post-exposure bake was done at 65 ℃ for 1 minute and 95 ℃ for 15 minutes, and the master was developed in a SU-8 developer solution for 12 minutes with agitation. PDMS monomer and a curing agent were mixed in 10:1 ratio. After degassing to remove foams, the mixture was gently poured onto the SU-8 master. The PDMS was cured at 65 ℃ for 90 minutes and the PDMS structure was cut and peeled off from the master. Each channel layer was cut to the size of approximately 30 mm by 30 mm. The cell culture chamber layer was made by punching three holes with 4 mm biopsy punch (Fisher Scientific, Hampton, NH) in a 0.25 mm thickness silicone gasket (Grace Bio Labs, Bend, OR). The polycarbonate base frame was made by cutting a 0.5 mm thickness polycarbonate piece into 30 mm by 30 mm size, and drilling 2 mm diameter holes at two corners for medium recirculation. For the silicon gasket layer, a 0.5 mm thick silicon sheet was cut to the same size, and inlet and outlet holes were punched with a biopsy punch (2 mm, Fisher Scientific). The aluminum bottom and plexiglass top frames were made with a milling machine, by drilling a screw hole on each side. The bottom frame also has two inlet/outlet holes (~ 2 mm diameter) at each corner. A well, or medium reservoir is made by curing a 5 mm thick PMDS sheet, cutting it to 1 cm by 1 cm size, and punching a 4 mm through-hole with a biopsy punch. The PDMS well was fixed on the drilled inlet/outlet hole with biocompatible, non-toxic glue (Epotek 301-2, Epoxy Technology, Billerica, MA). Aluminum was chosen for easy sterilization by autoclaving, and plexiglass was chosen for an easy visual inspection with a microscope. The plexiglass top frame does not need to be sterilized since it is not in a direct touch with cell culture medium, but was wiped with 70% ethanol before use.

6.2.3 Device Assembly and Operation

The device assembly process begins by placing the silicone gasket layer and the polycarbonate base frame on top of the aluminum frame. Then the cell culture chamber layer is placed on top. To prevent wrinkling of the 0.25 mm thin cell layer, a drop of 95% ethanol is placed on top of the polycarbonate base before placing the cell layer. After placing the cell layer on top, the whole device is placed in a hot oven for evaporation of ethanol, leaving the cell culture chamber layer in a uniform contact with the polycarbonate base frame. The assembled aluminum bottom frame, silicone gasket, polycarbonate base, and the cell culture chamber layer are placed in a Pyrex dish (150 x 20 mm, Fischer Scientific), and then sterilized by autoclaving. Cells are prepared by trypsinizing and centrifuging, and resuspending in 2% (w/v) alginate solution at 4x106 cells/ml. The alginate solution was made by dissolving alginate powder (10/60 LF sodium alginate, FMC biopolymer) in a HEPES buffer (15 mM HEPES, 92 mM sodium chloride). The alginate solution was filter-sterilized with 0.2 μm pore size syringe filter (VWR scientific, West Chester, PA). Cell-alginate suspensions of three cell types were prepared (HepG2/C3A, HCT-116, Kasumi-1, representing the liver, tumor and the marrow, respectively), and 10 μl of each cell suspension was placed in corresponding cell culture chamber. A porous polycarbonate membrane filter (8 μm pore size, VWR Scientific, West Chester, PA) was placed on top to flatten the alginate solution, and sterile-filtered 30 mM calcium chloride solution was applied onto each chamber to polymerize the hydrogel. After 30 minutes incubation at room temperature, calcium chloride solution and the membrane filter are removed. Then the top surface is flooded with 1 ml of DPBS, and the PDMS channel layer is closed on top, with channels facing down. The PDMS channel layer needs to be closed in a tilted manner to avoid capturing air bubbles. In addition, the PDMS

channel layer was sterilized by autoclaving the day before the assembly, and immersed in a sterile-filtered 3% pluronic F68 solution (Sigma-Aldrich, St. Louis, MO) overnight. This helps wet the surface of a hydrophobic PDMS surface, and prevents capturing air bubbles upon closing the channel layer. After closing the channel layer, the plexiglass top frame is placed on top, and the whole device is secured with screws. The device assembly and cell seeding process are summarized in Figure 6.1(b). Typically, twelve chips (with three cell types in each device) could be assembled in about two hours, excluding the time for autoclaving.

In case of using Matrigel™ instead of alginate to encapsulate cells, the same protocol was used except three differences. First, instead of a polycarbonate base piece, a glass piece was used for an improved sealing. A more secure sealing was required to use Matrigel in the device, which is softer than alginate. Secondly, gel was polymerized by incubating at 37 ℃, instead of using calcium chloride solution. Lastly, gel was dissolved in DPBS/5 mM EDTA solution to retrieve cells.

After assembly, the device is flipped upside-down, and two PDMS medium reservoirs on the bottom frame were filled with medium. The device in a sterile Pyrex dish was placed on a rocking platform, which was set to change direction at approximately every three minutes. Unless stated otherwise, uracil was added to 5-FU in 5:1 molar ratio, to prevent premature degradation of 5-FU. The whole system was placed inside a temperature-controlled mammalian cell culture incubator with 5% CO^2. After specified amount of time, the device was removed from the incubator and dissembled. Cells were retrieved by dissolving the alginate in a dissolving buffer (55 mM sodium citrate, 30 mM EDTA, 0.15 M NaCl) for 30 minutes at 37 ℃. Cell viability was determined by Trypan-blue exclusion assay using a hemocytometer. At least triplicates were done for each data point.

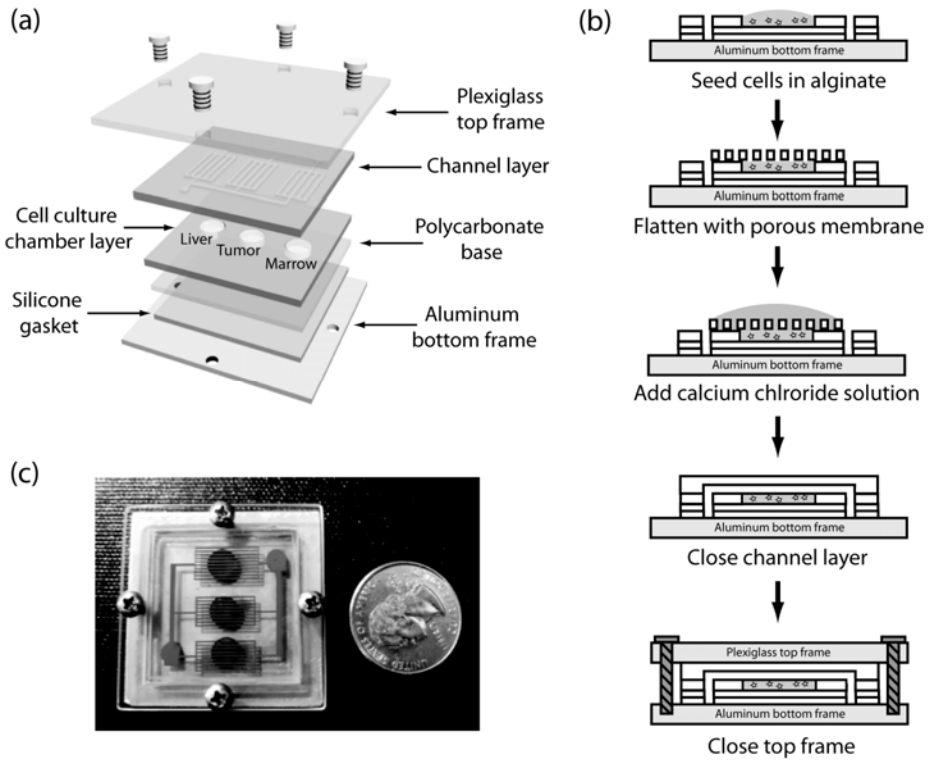

Figure 6.1 Schematics of device assembly

(a) A schematic of device components. A channel layer and a cell culture chamber layer are superimposed and sealed by top and bottom frames. A silicone gasket and a polycarbonate base are inserted for better sealing. (b) Cell seeding and device assembly process. Hydrogel-encapsulated cells are seeded into corresponding holes on a cell culture chamber layer, and flattened with a porous membrane. Alginate gel is formed by wetting with calcium chloride solution for 30 minutes. After gel formation membrane is removed and the channel layer is closed on top, and the top layer is closed for sealing. (c) A picture of the assembled device. A red dye was used for visualization of channels, and a blue dye was mixed with alginate.

6.2.4 Pharmacokinetic-Pharmacodynamic (PK-PD) Modeling

A PK-PD model was developed by constructing a PK and a PD model separately, and then combining the two. A PK model has the same layout as a μCCA device. Inside each compartment, there is a PD model, which predicts how fast cells die in response to 5-fluorouracil. Combination of a PK and a PD model enables prediction of how fast cells would be killed in response to a given dosage of 5-FU and uracil.

To construct a PK model for a μCCA, mass balance equations describing the flow in, flow out, and metabolism were set up for each compartment. Solving the equations requires several parameters, such as physiological parameters (flow rate and size of chambers) and enzyme kinetic parameters for the metabolism of 5-FU and uracil, which are summarized in Table 6.1. The predicted concentration profiles of 5-FU and uracil were used as inputs of a PD model in each compartment. To construct a PD model that predicts the response of cells to the drugs, a transit compartment model was used. A transit compartment is useful for modeling the growth kinetics of tumor in response to chemotherapeutic agents (Lobo and Balthasar 2002). Figure 6.2 shows the design of the three-chamber μCCA device, and a corresponding PK model of the device, and a PD model for each compartment. All of equations for the PK-PD model were solved using the ode45 routine of Matlab software (Mathworks, Natick, MA). The parameters for the PD model were fitted to experimental data by using the lsqnonlin (non-linear least square) routine of the optimization toolbox in the Matlab software. The fitted parameters were K_{max}, KC_{50}, and k_d. Other parameters were fixed at $C_0 = 3000$, $C_{ss} = 14000$, $k_g = 0.001$, tau = 5 (Sung et al. 2009). The viability at each time point was calculated as the ratio of the number of live cells to the number of total cells.

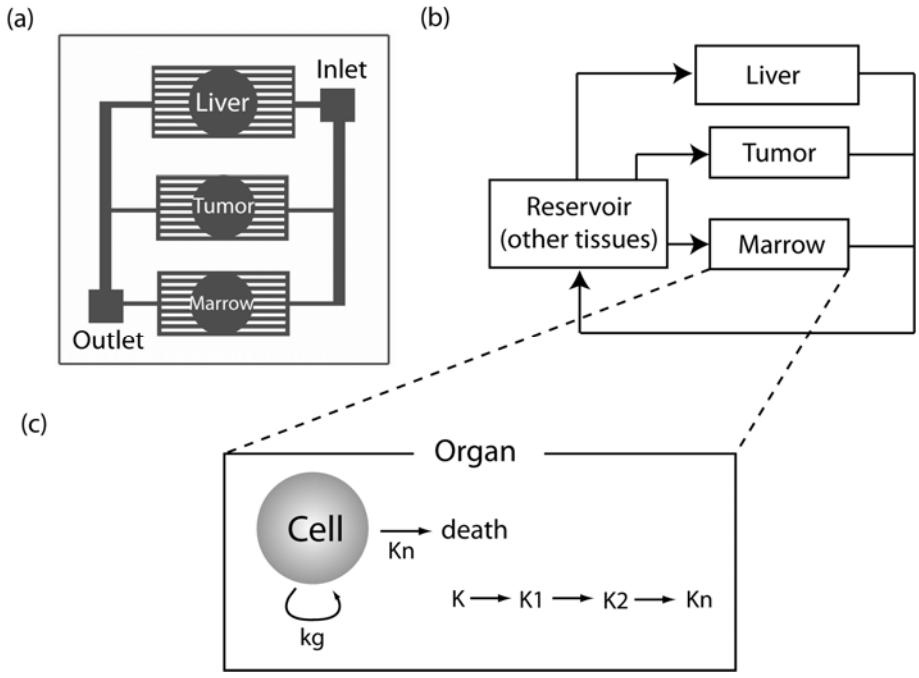

Figure 6.2 A μCCA and corresponding PBPK and PD models

(a) A design of a three-chamber μCCA. (b) A corresponding PBPK model, with the liver, tumor and marrow compartment. (c) A PD model for cell death in each compartment. The 'organ' can be the liver, tumor or marrow.

Table 6.1 Parameters for the PK model of a μCCA

Name	Description	Value
Physiological parameters[1]		
V_L	Volume of liver chamber	11.3 μl
V_T	Volume of tumor chamber	11.3 μl
V_M	Volume of marrow chamber	11.3 μl
V_B	Volume of medium reservoir	300 μl
Q_L	Flow rate into liver chamber	87.6 μl/min
Q_T	Flow rate into tumor chamber	26.7 μl/min
Q_M	Flow rate into marrow chamber	35.6 μl/min
Enzyme kinetic parameters[2]		
Vm_FU	Maximum rate of 5-FU metabolism	2385 nmol/min/ml
Km_FU	Michaelis-Menten constant for 5-FU metabolism	40 nM
Vm_U	Maximum rate of uracil metabolism	1695 nmol/min/ml
Km_U	Michaelis-Menten constant for U metabolism	40 nM
Ki_U[3]	Inhibition constant of uracil on 5-FU metabolism	20 nM
Ki_FU[3]	Inhibition constant of 5-FU on uracil metabolism	10 nM

1. Physiological parameters such as volumes and flow rates of organ chambers were determined based on reported values of organ sizes and blood flow rates in the human body (Davies and Morris 1993; Sung and Shuler 2009)

2. The enzyme kinetic parameters were calculated from the rate of 5-FU and uracil metabolism in a rat (Ikenaka et al. 1979), and reported protein content and cell number in the liver(Quick and Shuler 1999). The reported rates of 5-FU and uracil in a rat and human are comparable (Naguib et al. 1985).

3. Inhibition constants were taken from a previous study (Sung et al. 2009).

6.3 Results

6.3.1 Device Assembly and Gravity-induced Flow

Bonding of PDMS by oxygen plasma treatment is the most common method of sealing a microfluidic device made of PDMS. However, micro cell culture analog requires seeding multiple types of cells in a single device to achieve a multi-organ interaction; therefore the device has to be assembled after seeding each cell in the chambers of the device. The device was sealed by securing a plastic top and aluminum bottom frame with screws, with the PDMS channel layer and a hydrogel layer sandwiched between the frames. Although this method is reversible and may not be as robust as the irreversible sealing by plasma bonding, the sealing was sufficiently robust to prevent the leakage of recirculating medium from the device. The sealing at the interface between the channel and the gel layer was verified by using a fluorescein solution and fluorescent beads. Figure 6.3 shows the microscope pictures of the device after assembling the device, showing the sealing between the channels and the hydrogel. A bright-field image in Figure 6.3(a) shows both of channels and a chamber, and in Figure 6.3(b) the channels are visualized with fluorescein solution. Figure 3(c) shows the fluorescent beads embedded in the hydrogel. When cell-hydrogel mixture is introduced into the chamber, the height of the hydrogel must higher than the surface of the PDMS hydrogel layer to avoid leaking. In addition, gels shrink in volume during gelling process, so excess amount of cell-hydrogel mixture had to be inserted. On the other hand, inserting too much volume of hydrogel would result in blocking the channels above. In case of 0.5 mm thickness hyFdrogel layer, it was calculated that volume of a chamber in a hydrogel layer is about 10 μl. The sealing of the device gave the best result when the amount of cell-hydrogel mixture inserted was 18 μl. In case of

0.2 mm thickness gel, 10 μl volume of mixture was inserted to give the best sealing result.

The recirculation of cell culture medium was achieved by gravity-induced flow (Figure 6.4(a)). Using gravity has several advantages over using an external pump. First, removal of an external pump reduces the total space occupied by the device and enables a high throughput experiment. Secondly, use of silicone tubing often causes adsorption of molecules on the inner surface, and gravity-induced flow eliminates the possibility of unwanted binding. Thirdly, using gravity automatically solves the problem of air bubble formation, since air bubbles are prevented from entering the device due to its buoyancy. The flow rate through the conduits depends on several factors, and can be expressed by following equation (Morier et al. 2004).

$$Q = \frac{\rho g \pi}{8\eta} \frac{\Delta h R^4}{L} \qquad (6.1)$$

Where Q is the volumetric flow rate ($m^3 \bullet sec^{-1}$), ρ is a density ($kg \bullet m^{-3}$), g is the gravity constant ($m \bullet s^{-2}$), η is a fluid viscosity (Pa•s), Δh is a height difference (m), R is the radius of a channel (m), and L is the length of a channel (m). The μCCA device consists of several channels connected in parallel, and can be thought as a single hypothetical single channel when combined together. The equation (1) indicates that the flow rate is linearly proportional to the height difference, and the experimental result shown in Figure 6.4 demonstrates that this is true. However, the line does not converge to zero intercept, as predicted by the equation. A possible cause for such an observation is that after the flow is initiated, the height difference continuously changes as the liquid moves from the higher well to the lower well, which could have introduced an error in the measured height difference. With a smaller initial height difference, the effect of the error would have been greater.

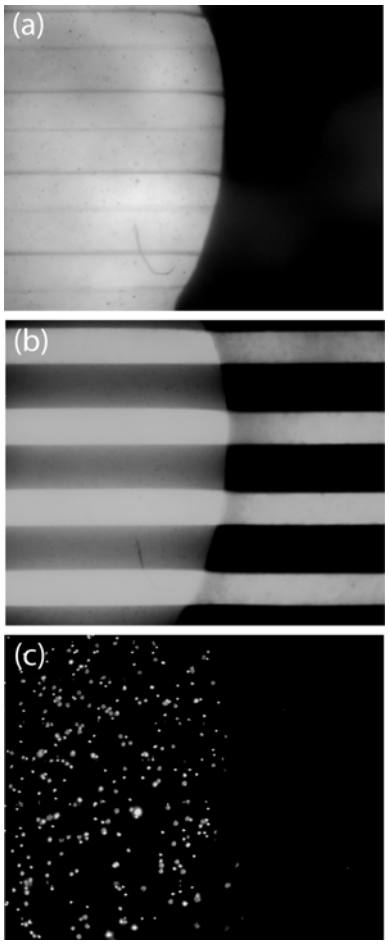

Figure 6.3 Sealing of device

(a) A bright-field picture of the assembled μCCA. A cell culture chamber and channels are shown on the left side of the picture (b) A fluorescein solution was inserted to visualized the channel and test sealing. Channels are shown in bright green. Fluorescein also diffuses into alginate, staining them in light green. (c) A cell culture chamber is seen with red fluorescent beads, which were mixed with alginate and inserted into a μCCA.

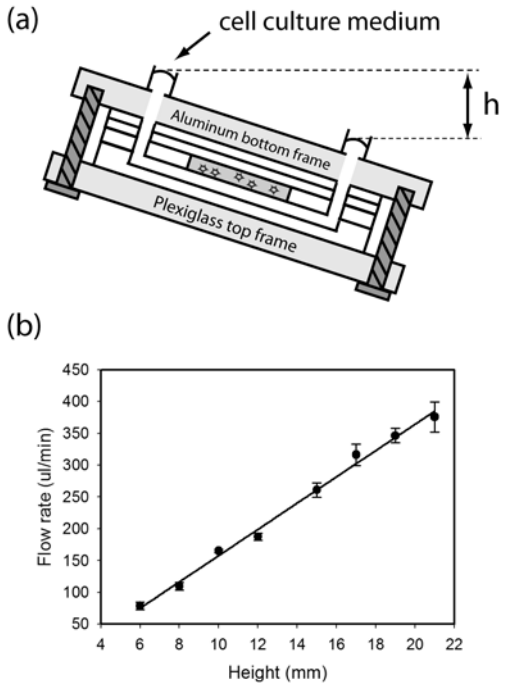

Figure 6.4 Gravity-induced flow

(a) Medium recirculation with gravity-induced flow in a μCCA. Tilting of the device causes liquid to flow from one well to the other well. After three minutes, the rocking platform changes the angle and medium flows in the opposite direction. (b) A plot of measured flow rates against various heights.

Using the gravity induced flow, it was possible to operate the device for several days with cells maintaining good viability. Figure 6.5 shows the live/dead staining result of the three cell types cultured in the device for three days. After three days, cells remained quite healthy, although different viability was observed depending on the cell type. For example, colon cancer cell line (HCT-116) showed viability close to 100%, whereas myeloblast (K-1) and hepatoma cell line (HepG2/C3A) showed somewhat lower viability. This difference demonstrates the variations in the cell response to the 3-D microfluidic environment. The observed trend in the cell viability in Figure 6.5 agrees with the viability measured using Trypan-blue exclusion assay, as will be shown later. In addition, it should be noted that the result shown in Figure 6.5 is for the case where the cell culture medium was recirculated without replenishment. Therefore, eventually a nutrient depletion and waste accumulation in the recirculating medium would have caused a loss of cell viability. In case where the cell culture medium was replaced every day, cells maintained a higher viability for a longer period of time.

6.3.2 Construction of PK-PD model

A PD model for a static hydrogel cell culture was constructed first. In the case of a static cell culture, a PK model is not needed, since a single cell type is cultured at a time, and no multi-organ interaction is expected to occur. A transit compartment model was constructed for each cell type, and the parameters for each cell type were fitted to experimental data. A transit compartment model assumes a series of transit compartments, representing various cell stages eventually leading to the cell death. It has been used for modeling the time-dependent, irreversible effect of a chemotherapeutic agent on tumor cells (Lobo and Balthasar 2002). Figure 6.6 shows

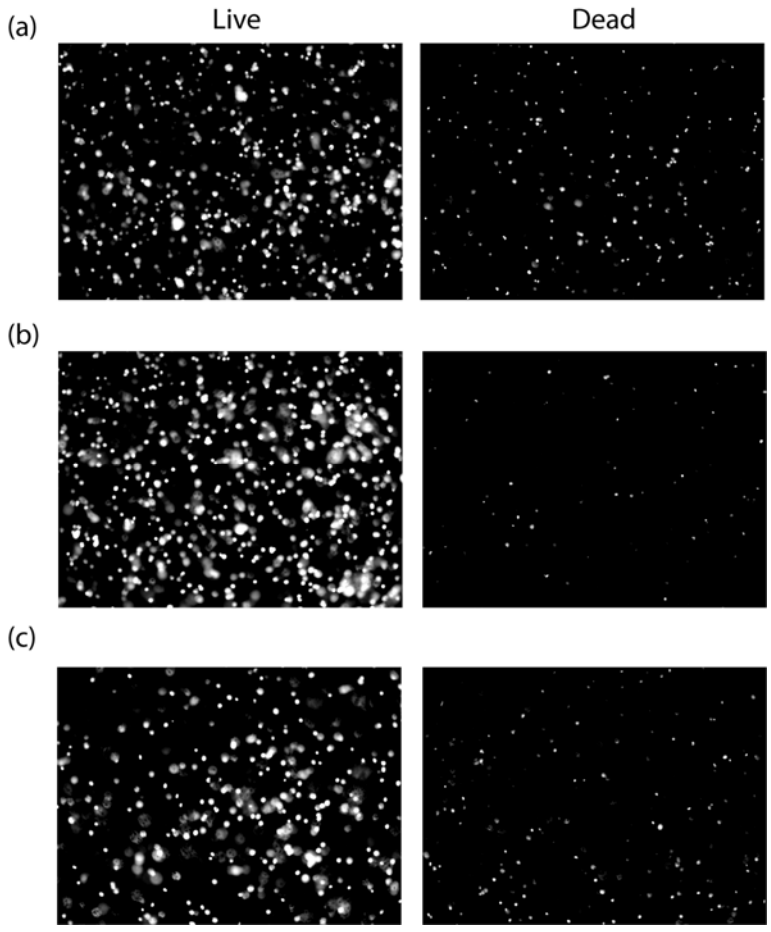

Figure 6.5 Live/dead staining of cells

(a) HepG2/C3A (b) HCT-116 (c) Kasumi-1 cells in a μCCA after three days of operation with medium recirculation

the experimental results with the simulation results of the constructed PD model in static condition. Overall, predicted cell viabilities for the three cell types showed a good agreement with the experimental data. However, some variations in the trend were observed. In case of HepG2/C3A cells, the drop in the viability seemed to be slower in day 2 and day 3, compared with a faster drop in the viability in the case of other cell types. Kasumi-1 cells, in particular, showed a considerable drop in the viability on day 3, when treated with 0.5 mM 5-FU. In general, PD models predicted more linear responses than the experimental result. This could imply that an additional molecular mechanism might be present, which is not accurately described by the transit compartment model. The fitted parameters for the PD model are summarized in Table 6.2.

A PK model was constructed for the μCCA with three different 5-FU concentrations. Figure 6.7(a) shows the concentration profiles of 5-FU in the device for the three dosing conditions. Due to the combination of uracil with 5-FU, metabolism of 5-FU is prohibited, and almost constant concentrations of 5-FU are maintained in all three concentrations. The short residence times in each compartment (100, 240, 180 seconds for the liver, tumor and the marrow compartment) ensure that all compartments are quickly equilibrated with medium reservoir, and the concentration profiles of 5-FU in the liver, tumor and the marrow compartment were similar to one another.

Once the PK model was constructed, the 5-FU concentration profile in each compartment was used as an input for a PD model in the same compartment. The parameters for the PD models were fitted to the cell viability result of the corresponding cell type, which are summarized in Table 6.3. Interestingly, Figure 6.7 shows that all cell types showed drastically different responses from one another, and also different responses from the static condition. In general, all cells showed a higher

sensitivity to 5-FU in a μCCA than in static condition. The high sensitivity of the cells in a μCCA was more evident in case of higher 5-FU concentrations in all cells. Also, when cells were tested in a μCCA, the differences between the cell types were more distinct than when they were tested in static condition. In the case of the static condition, shown in Figure 6.6, all three cell types showed similar trends in response to 5-FU treatment. In the case of a μCCA, in Figure 6.7, tumor (HCT-116) and morrow (Kasumi-1) cell lines were much more sensitive to 5-FU treatment than hepatoma (HepG2/C3A) cell line. The behavior of the cells in the absence of drugs was markedly different, too. When 5-FU concentration was zero, hepatoma cells showed a gradual loss in cell viability. In the case of marrow cell line, cell viability was as low as 60% on day 3, even without 5-FU treatment. The tumor cell line maintained a high viability throughout the three-day period, about 95% on day 3. On the other hand, when the cells were cultured in static condition, the behavior of the cells was similar to one another. At zero 5-FU concentration, all cells showed a gradual decrease in cell viability over three days, and addition of 5-FU caused a similar amount of drop in the cell viability across all three cell types.

6.3.3 Effect of Uracil as a Modulator

The major pathway for the metabolism of 5-FU is known to be through the enzyme dihydropyrimidine dehydrogenase (DPD), mainly present in the liver (Van Kuilenburg et al. 2002). Uracil inhibits 5-FU metabolism, and is often combined with 5-FU to enhance the effect of 5-FU (de Bono and Twelves 2001). The effect of uracil as a modulator of 5-FU was tested by removing uracil from the drug combination. First, using the PK-PD model for a μCCA, the PK profile and the responses of cells to the drugs (5-FU only and 5-FU plus uracil), was simulated (Figure 6.8(a)).

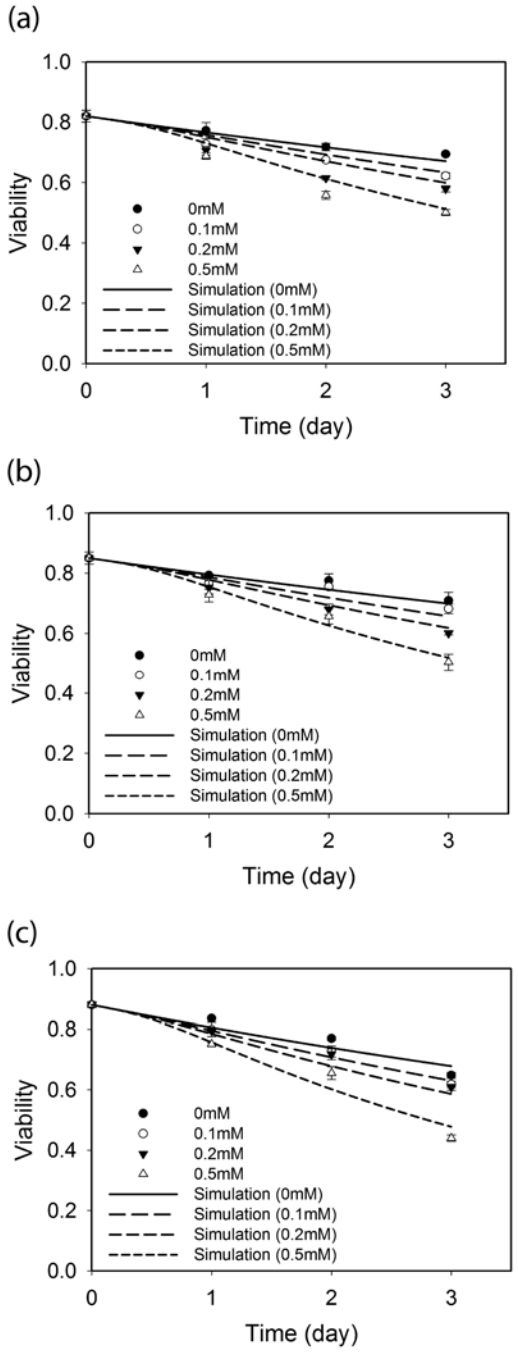

Figure 6.6 Measured and simulated cell viability in static condition

(a) HepG2/C3A (b) HCT-116 (c) Kasumi-1 for four different concentrations of 5-FU (0, 0.1, 0.2, and 0.5 mM).

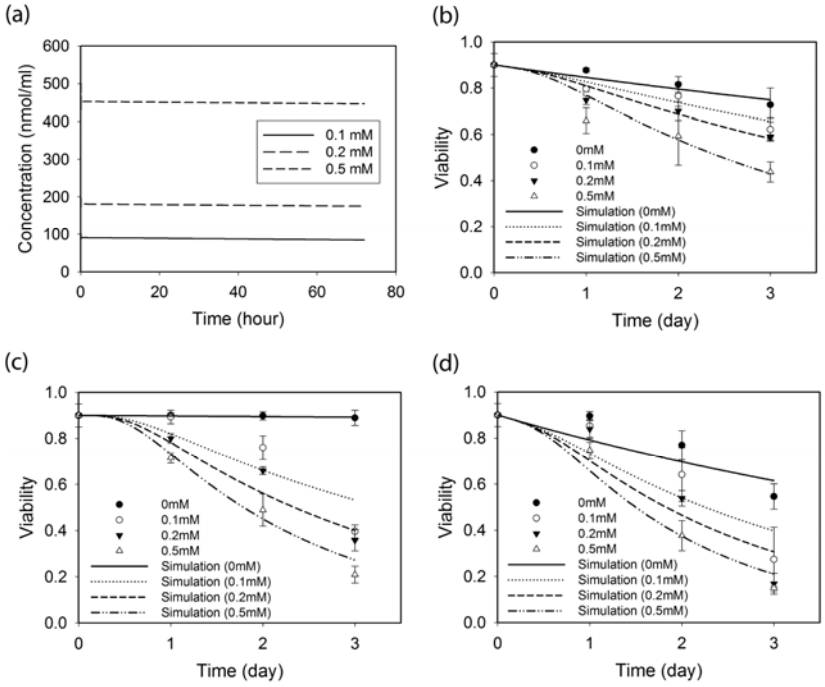

Figure 6.7 Measured and simulated cell viability in a μCCA

(a) Predicted concentration profiles of 5-FU in a μCCA for three different dosages. Measured and simulated viability of (b) HepG2/C3A (c) HCT-116 (d) Kasumi-1 cells in a μCCA treated with four different 5-FU concentrations for three days

Table 6.2 Parameters for a PD model in static condition

	HepG2/C3A	HCT-116	Kasumi-1
K_{max}	0.0578	0.0966	0.0992
KC_{50}	5515.2	8607.9	7409.4
k_d	0.003	0.0029	0.0038

Table 6.3 Parameters for a PD model in a μCCA

	HepG2/C3A	HCT-116	Kasumi-1
K_{max}	0.0470	0.0311	0.0299
KC_{50}	1665.3	205.3	246.6
k_d	0.0027	0.0002	0.0055

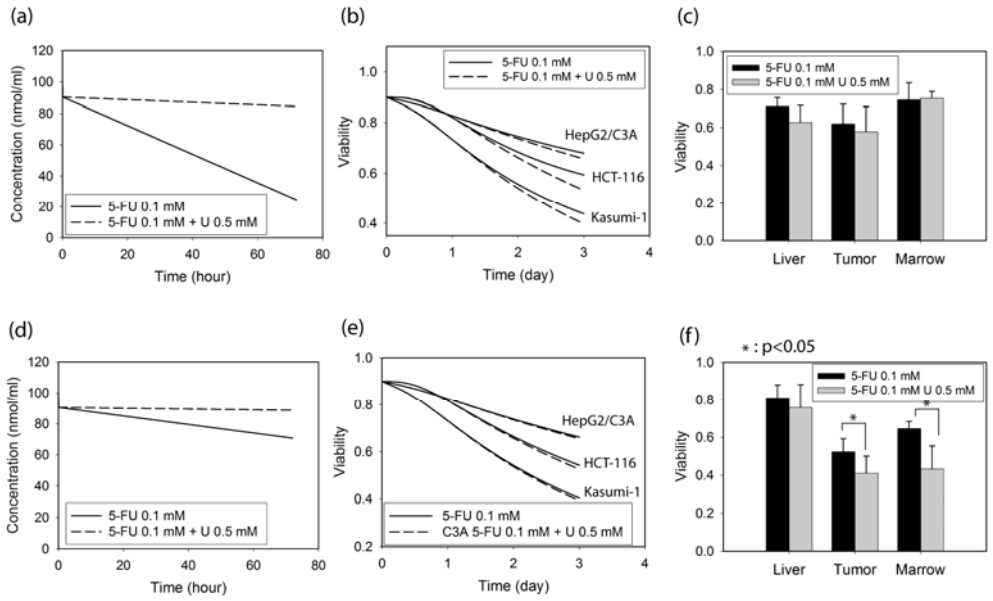

Figure 6.8 Effect of uracil as a modulator

(a) Predicted concentration profiles of 5-FU in a μCCA at two dosing conditions (0.1 mM 5-FU alone and 0.1 mM 5-FU plus 0.5 mM uracil). (b) Viabilities of three cell lines treated with 5-FU alone or 5-FU plus uracil. (c) Viability of three cell lines after 3-day treatment with 5-FU alone or 5-FU plus uracil. Cells were encapsulated in 2% alginate in a μCCA. (d) Predicted concentration profiles of 5-FU in a μCCA at two dosing conditions (5-FU alone and 5-FU plus uracil), with the rate of 5-FU metabolism reduced three-fold. (e) With the reduced metabolic activity, combination of uracil does not enhance the PD profile of 5-FU. (f) Viability of three cell lines after 3-day treatment with 5-FU alone or 5-FU plus uracil. Cells were encapsulated in MatrigelTM in a μCCA.

The absence of uracil is predicted to cause faster metabolism of 5-FU, resulting in about 80% reduction in 5-FU concentration on day 3. Consequently, all three cell types are predicted to have higher cell viabilities when treated with 5-FU only (Figure 6.8(b)). However, when this was tested experimentally using a μCCA, the difference in the cell viability was not significant (Figure 6.8(c)). We hypothesized that this was due to an insufficient metabolic activity of liver cells in the device. This was verified by a mathematical simulation, where the value of V_{max} in the PK-PD model was arbitrarily reduced. In this case, metabolism of 5-FU is slower, and absence of uracil does not have as much effect on the pharmacokinetics of 5-FU (Figure 6.8(d)). Consequently, the predicted cell viabilities in both cases are similar (Figure 6.8(e)). To enhance the metabolic function of HepG2/C3A cells, Matrigel™ was used instead of alginate as an encapsulating matrix. In this case, shown in Figure 6.8(f), combination of uracil with 5-FU showed an enhanced cytotoxic effect compared to 5-FU alone. Furthermore, the liver cells showed similar viabilities in both cases, whereas the tumor and marrow cells showed significantly lower cell viabilities when they were treated with 5-FU plus uracil than 5-FU alone ($p < 0.05$ for both tumor and marrow cells), which was consistent with a model prediction.

6.4 Discussion

6.4.1 Advantages of Layered Design

One of the aims of this work was to develop a 'user-friendly' microfluidic device, with a relatively easy device assembly and operation, high throughput implementation, and data extraction. These conditions had to be met while still enabling multi-organ interaction, which requires culturing multiple cell types in separate chambers in a single microfluidic device, and connecting them with fluidic

conduits. Having to seed multiple cell types sets a challenge in sealing the device, because the device has to be sealed after the cell seeding. The most common way of sealing a PDMS microfluidic device is oxygen or air plasma treatment, which would kill the cells. Equipping the microfluidic device with a fluidic-control system such as pneumatic valves (Unger et al. 2000) would allow to sealing the device before cell seeding, but this approach would increase the complexity of the device, which contradicts our initial objective. The separate layers for the cell culture chambers and fluidic conduits allowed one to seed multiple cell types at a time, and sealing the cell culture chamber layer and the channel layer with top and bottom frames provided a consistent sealing.

This design offered another advantage, that the thickness and the shape of the cell-encapsulated hydrogel could be changed simply by replacing the cell culture chamber layer, without having to modify the whole system. In addition to the 0.2 mm thickness layer used in this study, we also tested 0.5 mm and 1 mm thickness layers successfully. This feature may become useful in future studies, because the transport of oxygen and nutrients inside the system can be controlled by changing the geometry of the cell culture chambers. For example, the liver tissue is known to have a differential oxygen tension across its length, and the local liver function is known to vary depending on the local oxygen concentration, known as liver zonation (Allen and Bhatia 2003). A study with different oxygen concentrations in the system can be performed easily, simply by replacing the cell culture chamber layer with a different thickness, rather than fabricating the whole device. In addition, the use of gravity-induced convective flow eliminated the use of a pump, which enabled a more high-throughput implementation at a lower cost. Another, perhaps a more important advantage was that air bubble formation inside the device was naturally eliminated. The formation of air bubbles is a notorious problem in microfluidic systems, and

several attempts have been made to avoid this by using an external or in-line bubble trap (Kang et al. 2008; Skelley and Voldman 2008; Sung and Shuler 2009). However, the performance of a bubble trap is not always perfect, and it always has a limit in its capacity, that is, in the maximum amount of bubbles it can capture. The μCCA device could be operated in a bubble-free manner by using a gravity-induced flow, since bubbles were prevented from entering the device due to its buoyancy.

6.4.2 Insights from a PK-PD Model of a μCCA

The parameters for a PBPK model of a μCCA were found from the literature and from experimental conditions, whereas the parameters for the PD model were optimized by fitting to experimental data. It should be noted that the use of gravity-induced flow and a rocking platform results in a reciprocating mode of recirculation; instead of a continuous, closed-loop recirculation, the direction of the flow changes every three minutes. The effect of the reciprocating recirculation on the pharmacokinetic profiles of drugs was tested by mathematical simulation, and it was verified that this mode of recirculation causes a negligible deviation on the concentration profiles of both prodrug and metabolite (Figure 6.9). In addition to the PK-PD model for a μCCA, a PD model for the cells treated in static condition was developed, for comparison with a dynamic condition in a μCCA. The growth of cells was assumed to be negligible by setting the growth rate parameter at 0.001, because it was observed that the cell growth was negligible during the three-day period when encapsulated in alginate matrix. This observation was consistent with previous studies by other researchers, where cell growth was poor in alginate due to its inability to attach to the negatively-charged polymers (Grandolfo et al. 1993; Lawson et al. 2004).

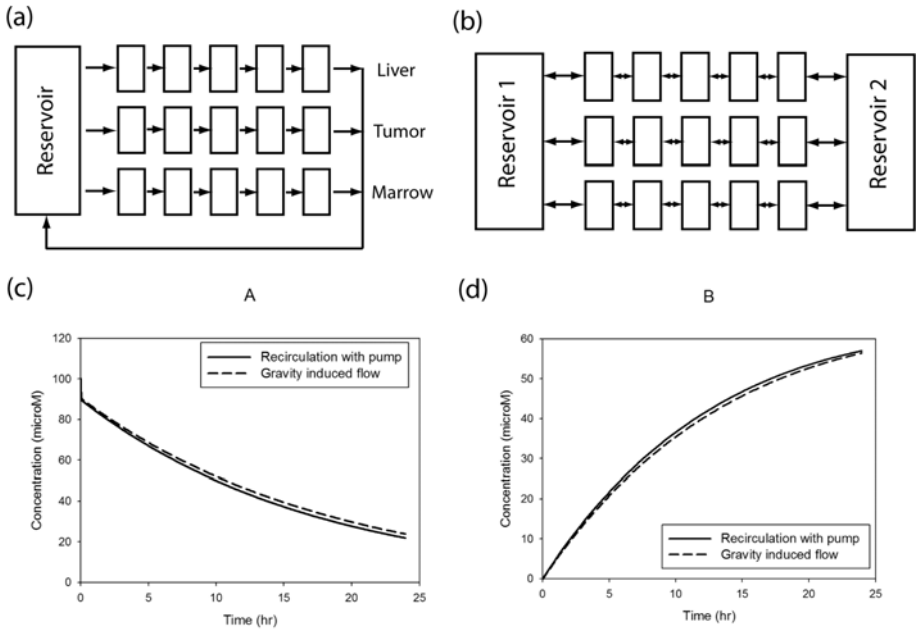

Figure 6.9 Comparison of PK profile for different modes of recirculation

Pharmacokinetic profiles of a hypothetical prodrug (A), and its metabolite (B) were simulated with a mathematical model representing the two modes. Each compartment was segregated into five sub-compartments, since using well-mixed assumption for the compartment neglects any difference that may be caused the reciprocating recirculation. (a) In the first model, a continuous recirculation is shown, where the flow coming out of each compartment goes back into the reservoir for recirculation. (b) In case of gravity-induced flow, the direction of the flow changes every three minutes. (c) Predicted concentration profiles of a prodrug A in both cases. (d) Predicted concentration profiles of metabolite B.

Comparison of optimized parameters gave a further insight into the behavior of cells in various conditions. In the transit compartment model, K_{max} shows how fast cells progress through the cell death mechanisms, and KC_{50} shows the concentration range of the drug in which they are most sensitive. Comparison the graphs in Figure 6.6 and 7 shows that in a μCCA cells go through cell death more rapidly in the static condition. A quantitative comparison of the parameters in static condition (Table 6.2) and the dynamic condition (Table 6.3) demonstrates that the differential response is caused by lower values of KC_{50} in the case of a μCCA, while the values of K_{max} were not changed as much. This implies that in a μCCA, cells were more sensitive in a lower concentration range than in static condition. In addition, differential behaviors between cell types could also be observed. In both static and dynamic conditions, the liver cells (HepG2/C3A) were most resistant to 5-FU, demonstrated by a lower value of K_{max} or a higher value of KC_{50} than other cell types. This observation is consistent with previous clinical findings, where hematological toxicity was the dose-limiting toxicity, and hepatotoxicity was less serious than other toxicities with 5-FU (van Kuilenburg 2004; Testart-Paillet et al. 2007). The value of k_d reveals the 'natural' death rate, of how fast cells die when drugs are not present. In static condition, the values of k_d were similar in all three cell types, whereas in a μCCA, the values varied widely between the cell types, implying that cells have differential adaptability to the microfluidic environment. For example, tumor cells (HCT-116, $k_d = 0.0002$) showed excellent cell viability for the three days in the device, while the viability of marrow cells (Kasumi-1, $k_d = 0.0055$) dropped down to about 60% on day 3 even in the absence of drugs.

In Figure 6.8, we showed the pharmacokinetic profile of 5-FU with two dosing strategies, administration of 5-FU alone or in combination with uracil. A mathematical simulation for the two dosing strategies was performed under two conditions, one with

a normal rate of 5-FU metabolism, and one with a low rate of 5-FU metabolism. In all cases, combination of uracil resulted in a higher concentration of 5-FU than the administration of 5-FU alone, but the amount of improvement was significantly higher only in the case where the metabolizing rate was normal (Figure 6.8(a) and (c)). As a consequence, combination of uracil enhanced the efficacy of 5-FU, that is, cells died more quickly, only when the metabolism rate of 5-FU was normal. Also, it is interesting to note that the difference in the resulting cell viabilities on day 3 is much smaller than the difference in the predicted 5-FU concentrations. This is because the mechanism of cell death due to a chemotherapeutic agent is time-dependent, and often the response of tumor cells is observed in a time-delayed manner (Lobo and Balthasar 2002). This is consistent with experimental observation in Figure 6.8(f), where the differences in the cell viability on day 3 were about 20% to 30%. We speculate that a longer experiment than three days would yield a greater difference in the cell viabilities, which we are planning to pursue in future studies.

6.4.3 Effect of Encapsulating Matrix on Cell Function

HepG2/C3A is a derivative cell line of HepG2, which is originated from the liver and is the most commonly used cell line for assessing the liver function. However, it is known to retain only minimal liver-metabolic activity (Wilkening et al. 2003). Furthermore, it is possible that culturing hepatoma cell in alginate matrix would reduce the metabolic function of the cells, since alginate polymers contain negative charges, which prevent attachment of cells, and do not provide functional groups necessary for proper cell signaling and function (Grandolfo et al. 1993; Lawson et al. 2004). It has been demonstrated that HepG2 cells can aggregate into a spheroid-like structure when encapsulated in alginate and cultured for over seven days

(Elkayam et al. 2006), but this was not observed during the three-day culture period in our experiment. It has been reported that the hepatic function of cultured hepatocytes can be enhanced by culturing them in a more naturally-derived hydrogel such as collagen or MatrigelTM (Brandon et al. 2003; Wang et al. 2008). In this study, a comparative study of encapsulating cells in alginate or Matrigel, and treating them with 5-FU alone or 5-FU plus uracil indicated that the metabolism of 5-FU may be slower in alginate than in Matrigel. We plan to verify this further in the future studies, by analyzing the metabolites in the recirculating medium, and comparing the rate of 5-FU metabolism and other metabolic activities of the liver cells in different conditions. In a preliminary study, it was shown that the P450 1A1/1A2 activity of HepG2/C3A cells can be enhanced when they are cultured in Matrigel, in the presence of flow (Sung et al. 2009). A further in-depth study into the contributing factors of a microfluidic environment with 3-D hydrogel cell cultures to authentic cell functions can yield valuable information about how to retain the liver-specific functions of cultured liver cells *in vitro*.

6.5 Conclusion

A microfluidic device based on a mathematical PK-PD model was developed. The layer-by-layer design and the use of gravity-induced flow allowed an easy assembly and operation of the device for several days. A mathematical model describing the pharmacokinetics (PK) and pharmacodynamics (PD) of 5-FU in the device was constructed, and the optimization of parameters provided an insight into the differential responses of cells to the drug in various environments. Combination of PK-PD modeling and a μCCA can provide a novel *in vitro*/*in silico* platform for testing the effect of drugs in a physiologically realistic manner.

REFERENCES

Allen, J. W. and S. N. Bhatia (2003). "Formation of steady-state oxygen gradients in vitro: application to liver zonation." Biotechnol Bioeng 82(3): 253-62.

Brandon, E. F., et al. (2003). "An update on in vitro test methods in human hepatic drug biotransformation research: pros and cons." Toxicol Appl Pharmacol 189(3): 233-46.

Davies, B. and T. Morris (1993). "Physiological parameters in laboratory animals and humans." Pharm Res 10(7): 1093-5.

de Bono, J. S. and C. J. Twelves (2001). "The oral fluorinated pyrimidines." Invest New Drugs 19(1): 41-59.

Derendorf, H., et al. (2000). "Pharmacokinetic/pharmacodynamic modeling in drug research and development." J Clin Pharmacol 40(12 Pt 2): 1399-418.

Derendorf, H. and B. Meibohm (1999). "Modeling of pharmacokinetic/pharmacodynamic (PK/PD) relationships: concepts and perspectives." Pharm Res 16(2): 176-85.

Dickson, M. and J. P. Gagnon (2004). "Key factors in the rising cost of new drug discovery and development." Nat Rev Drug Discov 3(5): 417-29.

Dingemanse, J. and S. Appel-Dingemanse (2007). "Integrated pharmacokinetics and pharmacodynamics in drug development." Clin Pharmacokinet 46(9): 713-37.

Elkayam, T., et al. (2006). "Enhancing the drug metabolism activities of C3A--a human hepatocyte cell line--by tissue engineering within alginate scaffolds." Tissue Eng 12(5): 1357-68.

Gerlowski, L. E. and R. K. Jain (1983). "Physiologically based pharmacokinetic modeling: principles and applications." J Pharm Sci 72(10): 1103-27.

Ghanem, A. and M. L. Shuler (2000). "Combining cell culture analogue reactor designs and PBPK models to probe mechanisms of naphthalene toxicity." Biotechnol Prog 16(3): 334-45.

Grandolfo, M., et al. (1993). "Culture and differentiation of chondrocytes entrapped in alginate gels." Calcif Tissue Int 52(1): 42-8.

Ikenaka, K., et al. (1979). "Effect of uracil on metabolism of 5-fluorouracil in vitro." Gann 70(3): 353-9.

Kang, J. H., et al. (2008). "Analysis of pressure-driven air bubble elimination in a microfluidic device." Lab Chip 8(1): 176-8.

Kang, L., et al. (2008). "Microfluidics for drug discovery and development: from target selection to product lifecycle management." Drug Discov Today 13(1-2): 1-13.

Khamsi, R. (2005). "Labs on a chip: meet the stripped down rat." Nature 435(7038): 12-3.

Kim, L., et al. (2007). "A practical guide to microfluidic perfusion culture of adherent mammalian cells." Lab Chip 7(6): 681-94.

Koebe, H. G., et al. (2000). "In vitro toxicology in hepatocyte bioreactors-extracellular acidification rate (EAR) in a target cell line indicates hepato-activated transformation of substrates." Toxicology 154(1-3): 31-44.

Kola, I. and J. Landis (2004). "Can the pharmaceutical industry reduce attrition rates?" Nat Rev Drug Discov 3(8): 711-5.

Lawson, M. A., et al. (2004). "Adhesion and growth of bone marrow stromal cells on modified alginate hydrogels." Tissue Eng 10(9-10): 1480-91.

Lin, J. H. and A. Y. Lu (1997). "Role of pharmacokinetics and metabolism in drug discovery and development." Pharmacol Rev 49(4): 403-49.

Lobo, E. D. and J. P. Balthasar (2002). "Pharmacodynamic modeling of chemotherapeutic effects: application of a transit compartment model to characterize methotrexate effects in vitro." AAPS PharmSci 4(4): E42.

Lobo, E. D. and J. P. Balthasar (2003). "Pharmacokinetic-pharmacodynamic modeling of methotrexate-induced toxicity in mice." J Pharm Sci 92(8): 1654-64.

Ma, B., et al. (2009). "Characterization of drug metabolites and cytotoxicity assay simultaneously using an integrated microfluidic device." Lab Chip 9(2): 232-8.

Mager, D. E., et al. (2003). "Diversity of mechanism-based pharmacodynamic models." Drug Metab Dispos 31(5): 510-8.

Mehta, K. and J. J. Linderman (2006). "Model-based analysis and design of a microchannel reactor for tissue engineering." Biotechnol Bioeng 94(3): 596-609.

Meyvantsson, I., et al. (2008). "Automated cell culture in high density tubeless microfluidic device arrays." Lab Chip 8(5): 717-24.

Morier, P., et al. (2004). "Gravity-induced convective flow in microfluidic systems: electrochemical characterization and application to enzyme-linked immunosorbent assay tests." Electrophoresis 25(21-22): 3761-8.

Naguib, F. N., et al. (1985). "Enzymes of uracil catabolism in normal and neoplastic human tissues." Cancer Res 45(11 Pt 1): 5405-12.

Quick, D. J. and M. L. Shuler (1999). "Use of in vitro data for construction of a physiologically based pharmacokinetic model for naphthalene in rats and mice to probe species differences." Biotechnol Prog 15(3): 540-55.

Roy, P., et al. (2001). "Analysis of oxygen transport to hepatocytes in a flat-plate microchannel bioreactor." Ann Biomed Eng 29(11): 947-55.

Sin, A., et al. (2004). "The design and fabrication of three-chamber microscale cell culture analog devices with integrated dissolved oxygen sensors." Biotechnol Prog 20(1): 338-45.

Skelley, A. M. and J. Voldman (2008). "An active bubble trap and debubbler for microfluidic systems." Lab Chip 8(10): 1733-7.

Sung, J. H., et al. (2009). "Fluorescence optical detection in situ for real-time monitoring of cytochrome P450 enzymatic activity of liver cells in multiple microfluidic devices " Biotechnol Bioeng, Accepted.

Sung, J. H., et al. (2009). "A combined pharmacokinetic-pharmacodynamic (PK-PD) model for tumor growth in the rat with UFT administration." J Pharm Sci 98(5): 1885-904.

Sung, J. H. and M. L. Shuler (2009). "A micro cell culture analog (micro CCA) with 3-D hydrogel culture of multiple cell lines to assess metabolism-dependent cytotoxicity of anti-cancer drugs." Lab chip 9(10): 1385-94.

Sung, J. H. and M. L. Shuler (2009). "Prevention of air bubble formation in a microfluidic perfusion cell culture system using a microscale bubble trap." Biomed Microdevices.

Tatosian, D. A. and M. L. Shuler (2009). "A novel system for evaluation of drug mixtures for potential efficacy in treating multidrug resistant cancers." Biotechnol Bioeng 103(1): 187-98.

Testart-Paillet, D., et al. (2007). "Contribution of modelling chemotherapy-induced hematological toxicity for clinical practice." Crit Rev Oncol Hematol 63(1): 1-11.

Unger, M. A., et al. (2000). "Monolithic microfabricated valves and pumps by multilayer soft lithography." Science 288(5463): 113-6.

van Kuilenburg, A. B. (2004). "Dihydropyrimidine dehydrogenase and the efficacy and toxicity of 5-fluorouracil." Eur J Cancer 40(7): 939-50.

Van Kuilenburg, A. B., et al. (2002). "Increased risk of grade IV neutropenia after administration of 5-fluorouracil due to a dihydropyrimidine dehydrogenase deficiency: high prevalence of the IVS14+1g>a mutation." Int J Cancer 101(3): 253-8.

Viravaidya, K., et al. (2004). "Development of a microscale cell culture analog to probe naphthalene toxicity." Biotechnol Prog 20(1): 316-23.

Wang, S., et al. (2008). "Three-dimensional primary hepatocyte culture in synthetic self-assembling peptide hydrogel." Tissue Eng Part A 14(2): 227-36.

Wilkening, S., et al. (2003). "Comparison of primary human hepatocytes and hepatoma cell line Hepg2 with regard to their biotransformation properties." Drug Metab Dispos 31(8): 1035-42.

Yang, S. T., et al. (2008). "Microbioreactors for high-throughput cytotoxicity assays." Curr Opin Drug Discov Devel 11(1): 111-27.

CHAPTER 7

FINAL CONCLUDING REMARKS AND FUTURE DIRECTIONS

The overall goal of this thesis work was to develop an *in vitro* platform to predict the toxicity of drugs better, using a combined approach of mathematical modeling and microfluidics technology. A PK-PD model was developed to describe tumor growth in a rat and its response to the administration of UFT. Various dosing strategies and the effect of metabolizing enzyme were simulated. The mathematical model revealed that the 5-FU chemotherapy can be optimized depending the level of metabolizing enzyme, and the efficacy can be further enhanced by optimizing the dosing schedule and the mode of administration. Based on the previous μCCA works, the μCCA was modified to enable 3-D hydrogel cell culture, which improved the cell functions in the device and allowed studies to reproduce metabolism-dependent toxicity of Tegafur. Among several improvements made over the previous versions, a PDMS microscale bubble trap significantly enhanced the consistency and success rate of device operation. In addition, *in situ* fluorescence optical detection system enabled a real-time monitoring of a μCCA, and it was demonstrated that the viability and the P450 activity of a hepatoma cell line (HepG2/C3A) can be observed and parameters extracted. A novel design of a μCCA was developed, which allowed easier high-throughput implementation. Utilization of a mathematical model to analyze the experimental results from the μCCA gave an insight into the behaviors of different cells in the μCCA or in static condition.

Ultimately, we envision that the μCCA combined with mathematical modeling will be able to supplement animal studies and human clinical trials. Given the high cost of animal/human studies, the ability to obtain prior information about the drug toxicity to allow more efficient design of animal/human studies will contribute

significantly to reducing the overall cost of drug development. Recently, the notion of personalized-medicine has been gaining a wider acceptance as it has become clear that individual variations in patients, whether genotypic or phenotypic, can contribute to differential reactions to the same dosing regimen. Research efforts are directed toward predicting how individuals will respond to a certain therapeutic regimen, and optimizing the regimen correspondingly. The 'body-on-a-chip' approach, described in this thesis work, paves the way towards achieving this goal. It will be possible to observe the response of tissue biopsy samples obtained from individual patients, and optimize dosing regimen on patient-specific basis.

To achieve this goal, several obstacles need to be overcome. The most critical of these is to reproduce authentic cell functions *in vitro*, such as the liver function for drug metabolism or the kidney for elimination of drugs and toxic wastes. Currently, there have been many research efforts to realize such 'artificial organs' *in vitro*, but this has not realized to a satisfactory level. Fortunately, with the advent of microfluidics and cells-on-a-chip technology, novel microscale 'organ' models are beginning to appear (Baudoin et al. 2007; Borenstein et al. 2007; Nahmias et al. 2007). In this perspective, characterization of the effect of microfluidic environment on the behavior of cells can provide important information. From our preliminary results, factors such as the encapsulating matrix, flow rate, and transport process seem to affect the behavior of cells, such as metabolic activity and response to drugs. Richer information about the effect of microfluidic environment on the cell behavior will foster the development of a more realistic μCCA, or 'body-on-a-chip'.

Secondly, high-throughput implementation of a μCCA will enable data collection at statistically meaningful level. However, a critical issue in microfluidic devices is the difficulty in the operation and high-throughput experimentation. What is particularly pertinent to a μCCA is that multiple cell types need to be seeded into a

device and the device must be sealed. This makes it impossible to seal the device with irreversible plasma bonding, the most commonly used method for sealing a microfluidic device. One solution is to incorporate a valve system, for example a pneumatic valve system, which will enable sealing the device first, and injecting the cell suspension. However, this approach will increase the complexity of the device and will render high-throughput operation difficult. A novel μCCA design is required, which will enable easier assembly and operation of multiple devices simultaneously. The new design described in chapter 6 partially addresses this issue, but more improvement is necessary to realize a true high-throughput implementation.

Finally, the μCCA device allows novel experiments which would be impossible to perform in static, conventional *in vitro* systems. For example, PK-PD modeling described in chapter 2 showed that a pharmacokinetic modulating chemotherapy (PMC) can significantly enhance the effectiveness of 5-FU chemotherapy, simply by controlling the dosing strategy of the drugs. This has also been demonstrated in clinical studies (Muneoka et al., 2005). Further optimization of the dosing strategy would be costly and time consuming, because it would be difficult to reproduce such dosing schemes *in vitro*, and can be tested only *in vivo*. The ability of microfluidic systems such as a μCCA to precisely control the flow pattern would allow one to test even complex dosing schemes, such as time-dependent dosing of multiple drugs. Such an attempt would be more successful if combined with a mathematical modeling approach. In that perspective, information about the drugs and metabolites concentration from HPLC or MS analysis would allow construction of a more detailed mathematical model of the μCCA.

REFERENCES

Baudoin, R., et al. (2007). "Trends in the development of microfluidic cell biochips for in vitro hepatotoxicity." Toxicol In Vitro 21(4): 535-44.

Borenstein, J. T., et al. (2007). "Microfabrication of three-dimensional engineered scaffolds." Tissue Eng 13(8): 1837-44.

Muneoka, K., et al. (2005). "Pharmacokinetic modulating chemotherapy highly effective for colorectal carcinoma metastases to multiple organs." Gan To Kagaku Ryoho 32(6): 799-802.

Nahmias, Y., et al. (2007). "Integration of technologies for hepatic tissue engineering." Adv Biochem Eng Biotechnol 103: 309-29.

APPENDIX

1. Equations for a PBPK model (chapter 2)

V_i: Volume of organ i

Q_i: Flow rate out of organ i

C_{ji}: Concentration of a chemical j (FT, 5-FU or uracil) in organ i

P_{ji}: Partition coefficient of chemical j in organ i

$k_{abs,j}$: Absorption rate constant for a chemical j

$V_{m,k,i}$: Maximum rate for enzyme k (CYP or DPD) in organ i

$K_{m,k,i}$: Michaelis-Menten kinetics constant for enzyme k in organ i

CL_j: Renal clearance rate of a chemical j

K_i: Inhibition constant for degradation reaction of DPD by uracil in liver

K_i_T: Inhibition constant for degradation reaction of DPD by uracil in tumor

K_{i_u}: Inhibition constant for degradation reaction of DPD by 5-FU

f_{b_i}: Unbound free fraction of i in tissue

$$V_{Lmn} \cdot \frac{dC_{FT,Lmn}}{dt} = -k_{abs,FT} \cdot V_{Lmn} \cdot C_{FT,Lmn}$$

$$V_G \cdot \frac{dC_{FT,G}}{dt} = [k_{abs,FT} \cdot V_{Lmn} \cdot C_{FT,Lmn} + Q_G \cdot C_{FT,B} - Q_G \cdot \frac{C_{FT,G}}{P_{FT,G}}]$$

$$V_L \cdot \frac{dC_{FT,L}}{dt} = \left[(Q_L - Q_G) \cdot C_{FT,B} - Q_L \cdot \frac{C_{FT,L}}{P_{FT,L}} + Q_G \cdot \frac{C_{FT,G}}{P_{FT,G}} - \frac{V_{m,CYP,liver} \cdot f_{b\_FT} \cdot C_{FT,L}}{K_{m,CYP,liver} + f_{b\_FT} \cdot C_{FT,L}} \cdot V_L \right]$$

$$V_T \cdot \frac{dC_{FT,T}}{dt} = \left[Q_T \cdot C_{FT,B} - Q_T \cdot \frac{C_{FT,T}}{P_{FT,T}} - \frac{V_{m,CYP,tumor} \cdot f_{b\_FT} \cdot C_{FT,T}}{K_{m,CYP,tumor} + f_{b\_FT} \cdot C_{FT,T}} \cdot V_T \right]$$

$$V_F \cdot \frac{dC_{FT,F}}{dt} = \left[Q_F \cdot C_{FT,B} - Q_F \cdot \frac{C_{FT,F}}{P_{FT,F}} \right]$$

$$V_W \cdot \frac{dC_{FT,W}}{dt} = \left[Q_W \cdot C_{FT,B} - Q_W \cdot \frac{C_{FT,W}}{P_{FT,W}} \right]$$

$$V_P \cdot \frac{dC_{FT,P}}{dt} = \left[Q_P \cdot C_{FT,B} - Q_P \cdot \frac{C_{FT,P}}{P_{FT,P}} \right]$$

$$V_B \cdot \frac{dC_{FT,B}}{dt} = \left[\begin{array}{l} Q_L \cdot \frac{C_{FT,L}}{P_{FT,L}} + Q_T \cdot \frac{C_{FT,T}}{P_{FT,T}} + Q_F \cdot \frac{C_{FT,F}}{P_{FT,F}} + Q_W \cdot \frac{C_{FT,W}}{P_{FT,W}} + Q_P \cdot \frac{C_{FT,P}}{P_{FT,P}} \\ - Q_B \cdot C_{FT,B} - CL_{FT} \cdot f_{b\_FT} \cdot C_{FT,B} \end{array} \right]$$

$$V_G \cdot \frac{dC_{FU,G}}{dt} = [Q_G \cdot C_{FU,B} - Q_G \cdot \frac{C_{FU,G}}{P_{FU,G}}]$$

$$V_L \cdot \frac{dC_{FU,L}}{dt} = [(Q_L - Q_G) \cdot C_{FU,B} - Q_L \cdot \frac{C_{FU,L}}{P_{FU,L}} + Q_G \cdot \frac{C_{FU,G}}{P_{FU,G}} + \frac{V_{m,CYP,liver} \cdot f_{b\_FT} \cdot C_{FT,L}}{K_{m,CUYP,liver} + f_{b\_FT} \cdot C_{FT,L}} \cdot V_L$$
$$- \frac{V_{m,DPD,liver} \cdot f_{b\_FU} \cdot C_{FU,L}}{K_{m,DPD,liver} \cdot (1 + \frac{C_{U,L,t}}{K_i}) + f_{b\_FU} \cdot C_{FU,L}} \cdot V_L]$$

$$V_T \cdot \frac{dC_{FU,T}}{dt} = [Q_T \cdot C_{FU,B} - Q_T \cdot \frac{C_{FU,T}}{P_{FU,T}} + \frac{V_{m,CYP,tumor} \cdot f_{b\_FT} \cdot C_{FT,T}}{K_{m,CYP,tumor} + f_{b\_FT} \cdot C_{FT,T}} \cdot V_T$$
$$- \frac{V_{m,DPD,tumor} \cdot f_{b\_FU} \cdot C_{FU,T}}{K_{m,DPD,tumor} \cdot (1 + \frac{C_{U,T}}{K_{i\_T}}) + f_{b\_FU} \cdot C_{FU,T}} \cdot V_L]$$

$$V_F \cdot \frac{dC_{FU,F}}{dt} = [Q_F \cdot C_{FU,B} - Q_F \frac{C_{FU,F}}{P_{FU,F}}]$$

$$V_W \cdot \frac{dC_{FU,W}}{dt} = [Q_W \cdot C_{FU,B} - Q_W \frac{C_{FU,W}}{P_{FU,W}}]$$

$$V_P \cdot \frac{dC_{FU,P}}{dt} = [Q_P \cdot C_{FU,B} - Q_P \frac{C_{FU,P}}{P_{FU,P}}]$$

$$V_B \cdot \frac{dC_{FU,B}}{dt} = [Q_L \cdot \frac{C_{FU,L}}{P_{FU,L}} + Q_T \cdot \frac{C_{FU,T}}{P_{FU,T}} + Q_F \cdot \frac{C_{FU,F}}{P_{FU,F}} + Q_W \cdot \frac{C_{FU,W}}{P_{FU,W}} + Q_P \cdot \frac{C_{FU,P}}{P_{FU,P}}$$
$$- Q_B \cdot C_{FU,B} - \frac{V_{m,DPD,blood} \cdot f_{b\_FU} \cdot C_{FU,B}}{K_{m,DPD,blood} \cdot (1 + \frac{C_{U,B}}{K_i}) + f_{b\_FU} \cdot C_{FU,B}} \cdot V_L - f_{b\_FU} \cdot CL_{FU} \cdot C_{FU,B}]$$

$$V_{Lmn} \cdot \frac{dC_{U,Lmn}}{dt} = -k_{abs,U} \cdot V_{Lmn} \cdot C_{U,Lmn}$$

$$V_G \cdot \frac{dC_{U,G}}{dt} = [k_{abs,U} \cdot V_{Lmn} \cdot C_{U,Lmn} + Q_G \cdot C_{U,B} - Q_G \cdot \frac{C_{U,G}}{P_{U,G}}]$$

$$V_{L,v} \cdot \frac{dC_{U,L,v}}{dt} = [(Q_L - Q_G) \cdot C_{U,B} + Q_G \cdot \frac{C_{U,G}}{P_{U,G}} - Q_L \cdot C_{U,L,v} - k_{in} \cdot C_{U,L,v} + k_{out} \cdot C_{U,L,t}]$$

$$V_{L,t} \cdot \frac{dC_{U,L,t}}{dt} = [k_{in} \cdot C_{U,L,v} - k_{out} \cdot C_{U,L,t} - \frac{V_{m,Uracil,L} \cdot f_{b\_U} \cdot C_{U,L,t,t}}{K_{m,Uracil,L} \cdot (1 + \frac{C_{FU,L}}{K_{i\_U}}) + f_{b\_U} \cdot C_{U,L,t}} \cdot V_{L,t}]$$

$$V_T \cdot \frac{dC_{U,T}}{dt} = [Q_T \cdot C_{U,B} - Q_T \cdot \frac{C_{U,T}}{P_{U,T}}]$$

$$V_F \cdot \frac{dC_{U,F}}{dt} = [Q_F \cdot C_{U,B} - Q_F \cdot \frac{C_{U,F}}{P_{U,F}}]$$

$$V_W \cdot \frac{dC_{U,W}}{dt} = [Q_W \cdot C_{U,B} - Q_W \cdot \frac{C_{U,W}}{P_{U,W}}]$$

$$V_P \cdot \frac{dC_{U,P}}{dt} = [Q_P \cdot C_{U,B} - Q_P \cdot \frac{C_{U,P}}{P_{U,P}}]$$

$$V_B \cdot \frac{dC_{U,B}}{dt} = [Q_L \cdot \frac{C_{U,L}}{P_{U,L}} + Q_T \cdot \frac{C_{U,T}}{P_{U,T}} + Q_F \cdot \frac{C_{U,F}}{P_{U,F}} + Q_W \cdot \frac{C_{U,W}}{P_{U,W}} + Q_P \cdot \frac{C_{U,P}}{P_{U,P}} - Q_B \cdot C_{U,B}$$
$$- CL_U \cdot C_{U,B} - \frac{V_{m,Uracil,B} \cdot f_{b\_U} \cdot C_{U,B}}{K_{m,Uracil,B} \cdot (1 + \frac{C_{FU,B}}{K_{i\_U}}) + f_{b\_U} \cdot C_{U,B}} \cdot V_B]$$

2. Equations for PD model (chapter 2)

C: Number of cells

C_S: Number of sensitive cells

C_R: Number of resistant cells

C_{ss}: Maximum cell number that can be reached

k_g: Cell growth rate

k_d: Cell death rate

k_{sr}: Rate of change of cell population from sensitive to resistant group

k_{rs}: Rate of change of cell population from resistant to sensitive group

K_{max}: Maximum cell kill rate

EC_{50}: Michaelis constant

τ: Mean transit time

FU: Concentration of 5-FU

K_n: nth transit compartment of the first set of transit compartments

L_n: nth transit compartment of the second set of transit compartments

Phase specific model

$$\frac{dC_S}{dt} = k_g \cdot C_S \cdot (1 - C_S / C_{SS}) - k_{sr} \cdot C_S + k_{rs} \cdot C_R - K \cdot C_S$$

$$\frac{dC_R}{dt} = k_{sr} \cdot C_S - k_{rs} \cdot C_R - k_d \cdot C_R$$

$$K = \frac{K_{max} \cdot FU}{EC_{50} + FU}$$

Transit compartment model

$$\frac{dC}{dt} = k_g \cdot C \cdot (1 - C / C_{SS}) - K_n \cdot C$$

$$\frac{dK_1}{dt} = (K - K_1)/\tau$$

$$\frac{dK_2}{dt} = (K_1 - K_2)/\tau$$

$$\frac{dK_3}{dt} = (K_2 - K_3)/\tau$$

.....

$$\frac{dK_n}{dt} = (K_{n-1} - K_n)/\tau$$

$$K = \frac{K_{max} \cdot FU}{EC_{50} + FU}$$

Dual transit compartment model

$$\frac{dC}{dt} = k_g \cdot C \cdot (1 - C/C_{SS}) - K_n \cdot C - L_n \cdot C$$

$$\frac{dK_1}{dt} = (K - K_1)/\tau_1$$

$$\frac{dL_1}{dt} = (L - L_1)/\tau_2$$

$$\frac{dK_2}{dt} = (K_1 - K_2)/\tau_1$$

$$\frac{dL_2}{dt} = (L_1 - L_2)/\tau_2$$

.....

$$\frac{dK_n}{dt} = (K_{n-1} - K_n)/\tau_1$$

$$\frac{dL_n}{dt} = (L_{n-1} - L_n)/\tau_2$$

$$K = \frac{K_{max} \cdot FU}{EC_{50} + FU}$$

$$L = \frac{K'_{max} \cdot FU}{EC'_{50} + FU}$$

3. Equations for a PBPK model (chapter 6)

FU: 5-FU, U: uracil, B: blood, L: liver, T: tumor, M: marrow

$C_{a,b}$: Concentration of a in compartment b.

V_a: Volume of compartment a

Q_a: Flow rate into compartment a

$$V_B \cdot \frac{dC_{FU,B}}{dt} = Q_L \cdot C_{FU,L} + Q_T \cdot C_{FU,T} + Q_M \cdot C_{FU,M} - Q_B \cdot C_{FU,B}$$

$$V_L \cdot \frac{dC_{FU,L}}{dt} = Q_L \cdot C_{FU,B} - Q_L \cdot C_{FU,L} - \frac{V_{m,FU} \cdot C_{FU,L} \cdot V_L}{K_{m,FU} \cdot (1 + \frac{C_{U,L}}{K_{i,U}}) + C_{FU,L}}$$

$$V_T \cdot \frac{dC_{FU,T}}{dt} = Q_T \cdot C_{FU,B} - Q_T \cdot C_{FU,T}$$

$$V_M \cdot \frac{dC_{FU,M}}{dt} = Q_M \cdot C_{FU,B} - Q_M \cdot C_{FU,M}$$

$$V_B \cdot \frac{dC_{U,B}}{dt} = Q_L \cdot C_{U,L} + Q_T \cdot C_{U,T} + Q_M \cdot C_{U,M} - Q_B \cdot C_{U,B}$$

$$V_L \cdot \frac{dC_{U,L}}{dt} = Q_L \cdot C_{U,B} - Q_L \cdot C_{U,L} - \frac{V_{m,U} \cdot C_{U,L} \cdot V_L}{K_{m,U} \cdot (1 + \frac{C_{U,L}}{K_{i,FU}}) + C_{U,L}}$$

$$V_T \cdot \frac{dC_{U,T}}{dt} = Q_T \cdot C_{U,B} - Q_T \cdot C_{U,T}$$

$$V_M \cdot \frac{dC_{U,M}}{dt} = Q_M \cdot C_{U,B} - Q_M \cdot C_{U,M}$$

4. Equations for a PD Model (chapter 6)

$$\frac{dC1}{dt} = k_g \cdot C1 \cdot \left(1 - \frac{C1}{C_{SS}}\right) - C4 \cdot C1 - k_d \cdot C1$$

$$\frac{dC2}{dt} = (\frac{K_{max} \cdot FU}{KC_{50} + FU} - C2)/tau$$

$$\frac{dC3}{dt} = (C2 - C3)/tau$$

$$\frac{dC4}{dt} = (C3 - C4)/tau$$

C_n: Number of cells in the nth transit compartment.

K_{max}: Maximum rate of cell death progression

KC_{50}: Saturation constant

FU: 5-FU

tau: Time constant for cell death progression

k_d: Natural cell death rate

C_{SS}: Maximum cell number that can be reached

K_g: Cell proliferation rate